UiO : Department of Chemistry
University of Oslo

Altering the structural elements of indole–based PDF inhibitors

Synthesis and characterisation

Kristian Sørnes
Master's Thesis, Spring 2021

Altering the structural elements of indole–based PDF inhibitors

Synthesis and characterisation

Kristian Sørnes

Thesis submitted for a Master’s degree in Chemistry
60 credits

Department of Chemistry
Faculty of mathematics and natural sciences

UNIVERSITY OF OSLO

Spring 2021

Altering the structural elements of indole–based PDF inhibitors

http://www.duo.uio.no/

Printed: Reprosentralen, University of Oslo

Acknowledgements

This thesis represents the final piece of a Master's degree in organic chemistry at the University of Oslo, and describes in detail the study I conducted. The work was carried out from August 2019 to June 2021 in the research group of Associate Professor Alexander H. Sandtorv, as part of the Organic Chemistry section at the Department of Chemisty.

First off, I would like to thank Alexander for the amazing help and guidance you have given over these past two years. Being a member of your group has made me grow both as a person and as a chemist, and your trust in me and my abilities has given me a level of confidence I have never had before. I am grateful for the opportunity to explore a topic I am very interested in, and I hope to continue working with you in the future.

I would also like to thank all of those who helped complete this thesis work. Thank you to past and present members of the east wing 2nd and 3rd floors, especially Linn and Cristiano for all you tips and tricks. Thank you to Ingeborg for being a patient and talented student, who let me dabble in supervision for the first time and who made me look critically at my own methods. Thank you to Professor Frode Rise and Senior Engineer Dirk Petersen for trusting me so much with the NMR instruments, and to Osamu Sekiguchi and Lina Aarsborg for running my MS samples. Thank you to the Catalysis section for letting me use your IR instrument. And of course, thank you so much Knut for all your insights. Your knowledge and experience has been crucial for me to complete this work.

This thesis represents the end of six long years as a student at UiO, and I am grateful for all of those wo accompanied me on this journey. Special thanks to Erlend for always being there to listen, Justin and Leon for the great year in Cambridge, my old roommates Andreas, Erlend and Hege for all the happy memories we made together, and Kristian for being a mentor to me for so many years. Thank you to my all my friends and family, especially my Besta who always thought so greatly of me.

My last thanks goes out to my dear Inga. Over the past year and a half, we have travelled the world, moved in together, lived through a global pandemic, contracted COVID, and each written a Master's thesis. This challenging time has only made us grow closer together, and I feel safe about the future knowing I have you by my side.

Kristian Sørnes
Oslo, June 28th 2021

Abstract

Indole–based hydroaxmic acids have previously been shown to selectively inhibit bacterial peptide deformylase (PDF), a metalloenzyme that cleaves off formyl the *N*–terminal end of newly formed proteins. Amino acid formylation and subsequent deformylation make up a set of processes that are crucial for bacterial growth and redundant in human cells, making PDF an intriguing antibacterial target. Inhibition of PDF represents a novel mode of action that is yet to be exploited by commercial antibiotics, something that is desparately needed in the fight against antimicrobial resistance.

The existence of a human mitochondrial PDF has been a source of concern despite its role in normal cell function being largely unknown. Inhibitors that are selective towards bacterial PDF are therefore of major interest. Indole–based inhibitors are said to achieve selectivity through their central indole scaffold, which is reportedly too bulky to fit the active site of human PDF. No justification for the indole fragment has been given apart from its apparent size, raising questions around which exact structural elements are needed for selective inhibition.

In this study, we sought to synthesise analogues of indole–based inhibitors with certain structural elements altered, intending to explore potential enzyme interactions that may or may not be important for inhibition. The central scaffold became the main focus of the study, for which four different synthetic routes were designed. The four target molecules included an indole benchmark and its corresponding benzimidazole, benzotriazole, and indene equivalents.

Of these, only the indole and indene targets were successfully synthesised. The indole structure could be formed at poor yields using a reported procedure, while the indene structure required careful handling of a dynamic *endo*/*exo*–isomerisation. Major steps were made in the syntheses of the benzimidazole and benzotriazole targets, with both scaffolds successfully being formed as intended. Ultimately, the designed routes failed at incorporating the needed hydroxamic acid functionality. The indole and indene inhibitors remain to be tested for inhibitory activity.

Future studies should focus on biochemical testing of the synthesised structures, as well as redoing the benzimidazole and benzotriazole routes using water–insoluble peptide coupling reagents in the final step. Preliminary studies were made on the formation of indolyl and indenyl hydrazides, although more purification is needed. Suggested synthetic routes for indane, naphthalene, pyridine, and thiohydoxamic acid targets are provided.

Abbreviations

ABR	Antibacterial resistance
AMR	Antimicrobial resistance
ATR	Attenuated total reflectance
br	Broad (NMR)
Bt	Benzotriazol–1–yl
COSY	Correlation spectroscopy
d	Doublet (NMR)
$\boldsymbol{\delta}$	Chemical shift
DMF	*N*,*N*–Dimethylformamide
DMSO	Dimethyl sulfoxide
EDCI	1–Ethyl––3–(3–dimethylaminopropyl)–carbodiimide
ESI	Electrospray ionisation
FID	Free induction decay
fMet	*N*–Formylmethionine
HMBC	Heteronuclear multiple–bond correlation spectroscopy
HRMS	High–resolution mass spectrometry
HSQC	Heteronuclear single–quantum correlation spectroscopy
IR	Infrared spectroscopy
$\boldsymbol{J}$	Coupling constant
m	Multiplet (NMR)
MAP	Methionyl aminopeptidase
mp	Melting point
$\boldsymbol{m/z}$	Mass–to–charge ratio
NMM	*N*–methylmorpholine
NMR	Nuclear magnetic resonance spectroscopy
NOESY	Nuclear Overhauser effect spectroscopy
$\boldsymbol{\widetilde{\nu}}$	Wavenumber
PDF	Peptide deformylase
ppm	Parts per million
q	Quartet (NMR)
$\boldsymbol{R_f}$	Retardation factor
RT	Room temperature
s	Singlet (NMR)
$\mathbf{S_NAr}$	Nucleophilic aromatic substitution
t	Triplet (NMR)
THF	Tetrahydrofuran
TLC	Thin–layer chromatography

Contents

1

Introduction

The ever–increasing threat of antimicrobial resistance (AMR) is pushing the world towards another global health crisis. The World Health Organization (WHO) estimates that 700 000 people die of drug–resistant diseases every year, a number that may reach 10 million by 2050 if no action is taken. [1,2] Key medical procedures like caesarian section and chemotherapy are at risk of getting too dangerous to perform, and diseases like tuberculosis and gonorrhoea are getting increasingly resistant to expensive last–resort antibiotics. [2,3] If nothing gets done, widespread AMR is expected to negatively impact global poverty, economic inequality, and access to clean water, with the World Bank predicting a constant state of financial crisis by 2030 and with no clear end in sight. [1,4]

1.1 AMR and the need for new antibiotics

Antimicrobial resistance (AMR) is a fundamental trait of evolution where microorganisms develop resistance towards antimicrobial agents that are designed to kill them. [2] The dangers of AMR revolve around pathogenic microbes like bacteria, viruses, fungi and parasites, all of which can cause life–threatening infections that are difficult to treat when resistance is present. [3] These threats are managable as long as there are several agents suitable for treatment, however some microbes – nicknamed “superbugs” – will over time develop multidrug resistance to entire arsenals of antimicrobials. When this occurs, infections may become untreatable until a new agent is discovered. [2]

Resistance commonly arises through a process called selection pressure, an accelerated type of natural selection where an antimicrobial agent kills off all target organisms except a few individuals with resistant genes. These genes usually stem from random genetic mutations occurring during reproduction, and encode features or changes that are beneficial against the antimicrobial. [5–7] With most competitors gone, these individuals have the space and opportunity to quickly reproduce and spread. Eventually, after continued exposure to the agent, the resistant properties develop into robust defence mechanisms. [2,5] This resistant strain may then spread to become the dominant strain, making the agent in question redundant.

However, resistance is not exclusively hereditary. In the world of bacteria, the primary mechanism for resistance transmission is through horizontal gene transfer, a process where genetic material can be transferred between two individual bacteria of the same generation. [5] The bacteria in question can be of different species and do not need to be closely related. [8] This means that antibacterial resistance (ABR) can spread rapidly across species whenever resistant bacteria get introduced to a bacterial flora, even in places where the antibacterial agent has never been used. Consequently, if bacteria with different modes of resistance are present in the same flora, horizontal gene transfer makes multidrug resistance more likely to emerge. [5, 9]

This ease of transmission, combined with a widespread overuse of readily available antibiotics, is partly why ABR is viewed as the most threatening branch of AMR. [1, 3] Despite the recent uptake in global awareness, its consequences are already present. Multidrug–resistant tuberculosis, caused by resistant strains of *Mycobacterium tuberculosis*, accounts for more than 35 % of all annual deaths by drug–resistant diseases worldwide. [10] Gonorrhea, caused by *Neisseria gonorrhoeae*, is on the rise in the Western world after becoming resistant to four out of five applicable medications. [2] And infections by *Clostridioides difficile*, while not typically resistant, saw an increase in mortality rate of 400 % across the 2000s following several deadly outbreaks of a resistant strain. [11] More generally, out of 66 countries surveyed by the WHO in 2019, more than 30 countries reported some degree of resistance in common infectious bacteria like *Escherichia coli* and *Klebsiella pneumoniae*, with some countries citing resistance rates of 80–90 % for certain antibiotic–bacterium combinations. [12] Healthcare officials agree that, while tackling AMR is inherently a multifaceted issue, the development of new antibiotics is urgently needed to reduce and prevent the impacts of ABR. [1–3]

Antibiotics are, in short, molecules that kill or otherwise inhibit the growth of bacteria. [2] They typically work by interacting with macromolecules that are crucial to the inner workings of bacterial cells. Their modes of action vary greatly, and will often define to which class they belong. [13] Penicillins, for instance, work by inhibiting enzymes that strengthen the bacterial cell wall, whereas quinolones work by obstructing DNA replication. Some antibiotics are classified as broad–spectrum and can be used on a wide range of bacteria, while others are more narrowly tailored for specific groups. [14] Having a large variety in both angle of attack and target specificity is an essential part of modern medicine, since the cause of infection and degree of resistance is often unknown. [14, 15]

Modern antibiotic development is, however, considered insufficient by the WHO and other healthcare officials at tackling ABR. [10] Following a golden age of class discovery in the mid 1900s, the focus of the pharmaceutical industry shifted to analogue development in the early 1970s, a strategy where old antibiotics are improved by adding or replacing functional groups to the baseline structure without altering the mode of action. [16] Over time, as older drugs turn ineffective, bacteria are able to quickly adapt their existing defense mechanisms to new analogues over a relatively short time. [3] By contrast, introducing new classes with novel modes of action force the bacteria to develop new resistance over a far longer time period. Analogue development as a strategy merely postpones the threats of ABR, and offers no sustainable long–term solution to the issue. [17]

This choice of strategy has resulted in a pool of antibiotics that is dominated by old classes, most of which were discovered sometime between 1940 and 1970. Following the release of carbapenems in 1985, nearly 25 years passed before a new class was on the market. [16] Of the five entirely new classes approved since 2000, four are limited to only one agent. [18–21] Of the eleven agents approved since 2017, only two are categorised as novel. And of the 43 antibiotics currently in clinical trials, only seven are considered innovative. [10]

As it stands, the global health sector is in dire need of new classes of antibiotics with novel modes of action. [3, 15, 17] This requires the scientific community to explore new ways of inhibiting bacteria, and the list of potential ways to do so is far from short. [22] The work in this thesis will focus on inhibitors of peptide deformylase, an enzyme involved in bacterial protein synthesis. As of June 2021, no commercially available antibiotic has inhibition of peptide deformylase as its mode of action. [23]

1.2 Peptide deformylase and its inhibitors

Peptide deformylase (PDF) is a globular, single–chained metalloenzyme found in all species of bacteria. Its purpose is to catalyse the deformylation of *N*–formylmethionyl peptides, a hydrolysis reaction where the formyl group is removed from the end of the chain and the resulting methionyl peptide is left with an exposed *N*–terminus. [24]

The need for PDF comes from the fact that, in bacteria, *N*–formylmethionine (fMet) is the starting residue that initiates close to all protein syntheses (Figure 1.1). Following ribosomal translation of mRNA, the fMet residue is no longer of use and newly made proteins almost always undergo deformylation. Of those deformylated, a majority has the underlying methionine removed by an enzyme named methionyl aminopeptidase (MAP). For some proteins the removal of this methionine is crucial to their function, since the *N*–terminal amino acid can affect stability and be involved in biological activity. In some cases the *N*–terminus is modified further, for instance to improve lipophilicity. [24]

The importance put on removing this terminal methionine means that inhibition of MAP can cause bacterial death. However, direct inhibition of MAP is not a viable strategy, as every other cellular life has regular methionine as the protein synthesis initiator. Treatment with MAP inhibitors is therefore lethal both to bacteria and humans. [24]

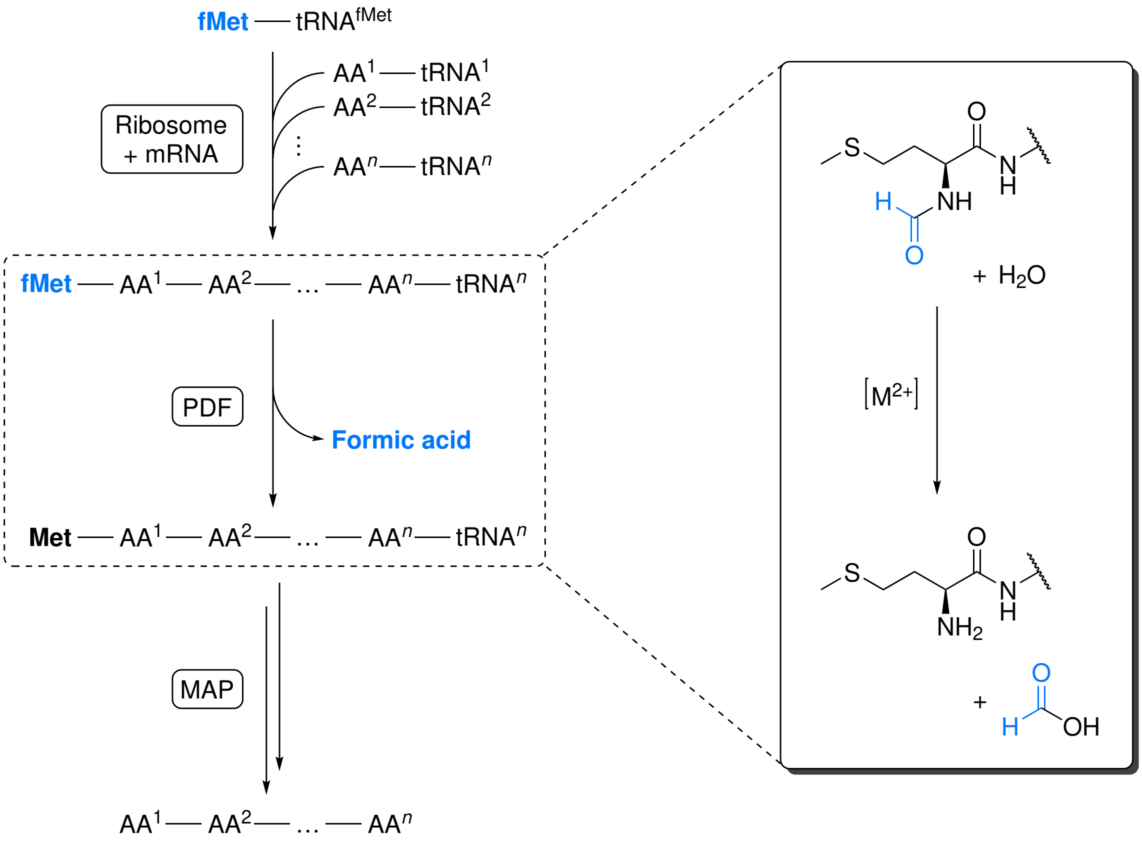

Figure 1.1: Schematic overview of bacterial protein synthesis, with AA^i being the i–th amino acid. Recreated from ref. 24 Framed: Peptide deformylase (PDF) catalyses the hydrolysis of *N*–formylmethionyl peptides into methionyl peptides and formic acid.

The reason PDF is a promising antibacterial target comes from its direct relationship with MAP. For the latter to be catalytically active, the incoming methionyl peptide must be deformylated in advance. [24] If most proteins remain formylated, the bacteria must survive using leftover proteins that were synthesised with methionine as the starting residue, since these can still react with MAP. This drastically reduces the number of functioning proteins in the cell, causing a bacteriostatic effect where the bacterium is not killed but its growth is severely hampered. [25]

The PDF enzyme itself consists of roughly 200 amino acids arranged in a single chain with a divalent iron cation in the centre. [22] Known for its instability, PDF is often isolated as a more stable nickel, cobalt, or zinc analogues. [26] The protein fold shows several consistent motifs across all bacterial species, including a central helix wedged between two β–sheets and a hairpin turn located close the metal centre (Figure 1.2). [24] These three motifs contain all the amino acids that make up the active site, including those specifically needed for catalysis. The metal cation, being bound to two histidines and one cysteine, adopts a tetrahedral geometry with a hydroxide ion as the fourth ligand (Figure 1.3). [26]

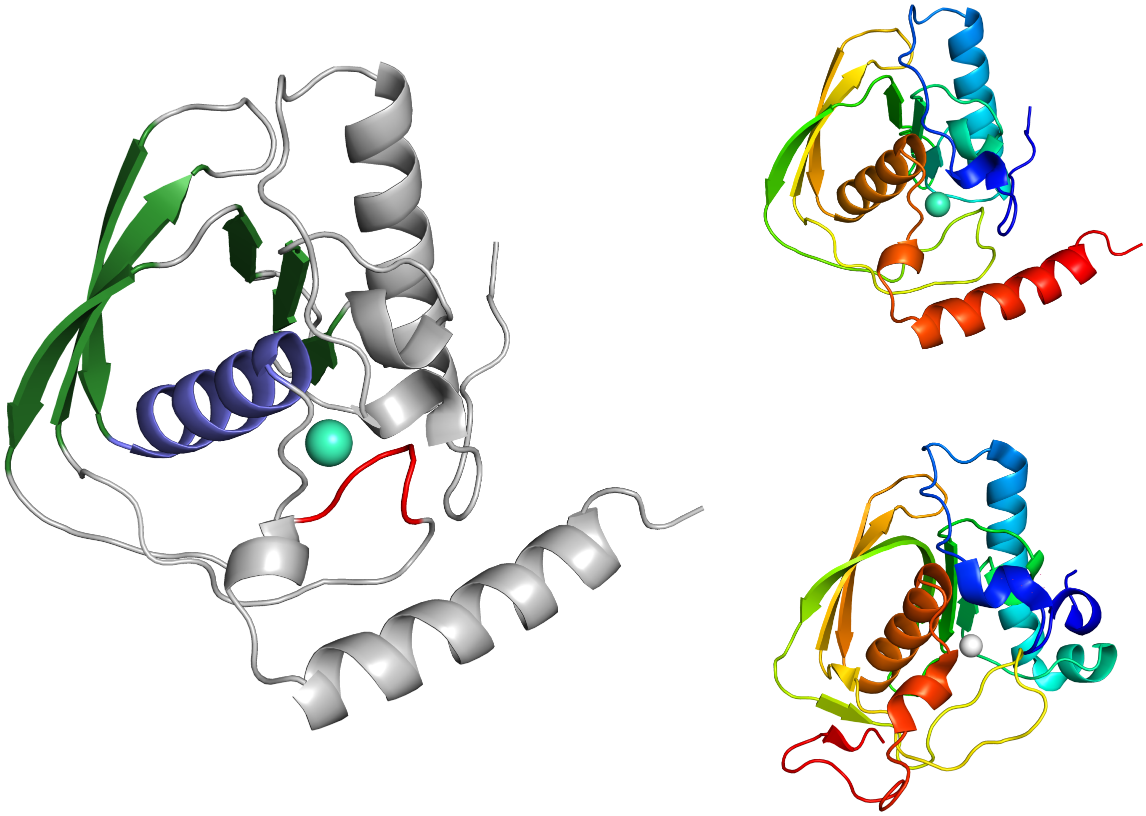

Figure 1.2: Left: Cartoon visualisation of *E. coli* Ni–PDF with the characteristic helix (blue), β–sheets (green) and hairpin (red) motifs highlighted. Right: Rainbow cartoon visualisation of *E. coli* Ni–PDF (top) and *Staphylococcus aureus* Zn–PDF (bottom), demonstrating a clear similarity across species. Metal cations are depicted as light green and white spheres, respectively. PDB IDs: 1BS7 and 1LMH. [27,28]

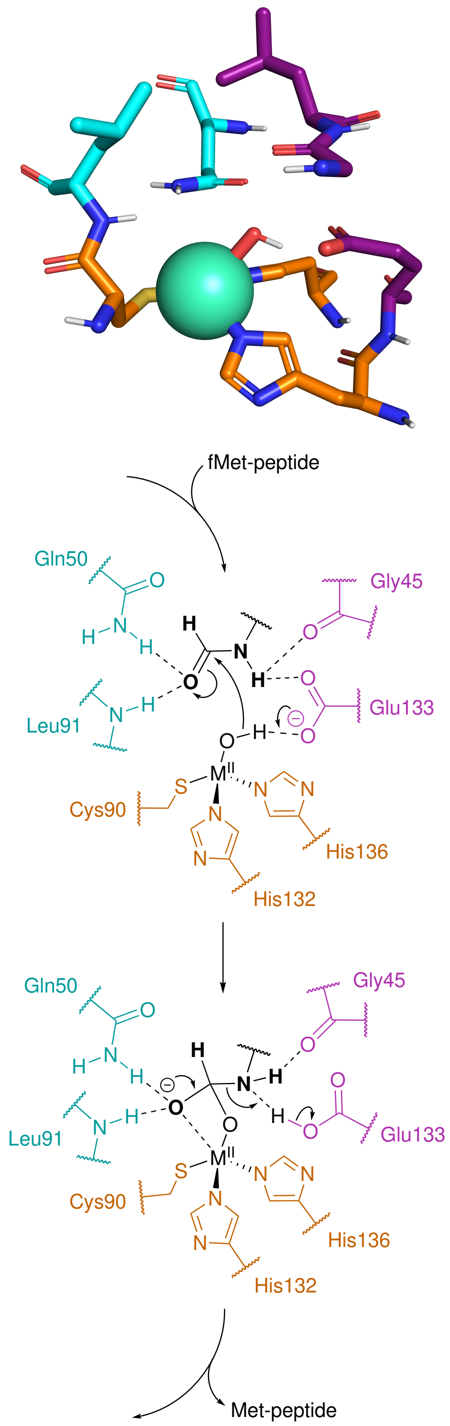

Figure 1.3: Top: Stick visualisation of the *E. coli* Ni–PDF catalytic site, with nickel as light green sphere. Atomic colours, with protein carbons coloured by mechanistic function of residue. PDB ID: 1BS7 [27]. Bottom: Fragment of the metal–generalised *E. coli* PDF catalytic cycle, showing the deformylation step. Recreated from ref. 26

Studies on the catalytic site has proposed this metal–bound hydroxide to be the nucleophile in the deformylation reaction. [26] As the fMet–peptide enters the site, hydrogen bonds from two nearby leucine and glutamine residues activate the formyl carbonyl bond. This allows the hydroxide to perform a nucleophilic attack, forming a tetrahedral oxyanion that is stabilised by both the metal and the aformentioned residues. The hydroxide proton is, simultaneously, transported near to the fMet nitrogen by a glutamate residue. Hydrogen bonds between the glutamate, a nearby glycine, and the substrate nitrogen promotes leaving group ability such that, when the oxyanion collapses, the metionine peptide is released. The remaining metal–bound formate readily hydrolyses, completing the catalytic cycle. [24, 26]

The greater active site also includes a deep hydrophobic pocket directly adjacent to the catalytic site, meant to accommodate the sulfide side chain of the fMet residue (Figure 1.4). [26] This pocket gives PDF its high specificity towards fMet–terminal peptides, and is the reason why deformylation can occur regardless of which amino acid is the second residue. [24]

With these results in mind, researchers quickly developed metal–coordinating inhibitors that could displace the active hydroxide ligand and disrupt the catalytic cycle. The coordinating group needed to be small enough to enter the narrow catalytic site and sufficiently acidic so as to form a strong ionic bond to the metal. Nearby, there had to be a hydrophobic structure element that could mimic the substrate methionyl side chain. The earliest inhibitors thus combined monodentate functional groups like thiols and hydrogen phosphonates with linear alkylic side chains like *n*–butyl and *n*–pentyl, producing inhibitory concentrations in the low micromolar range. [29, 30] Despite being definite proofs of concept, they ultimately lacked the degree of potency required of medicinal antibiotics. [31]

A major breakthrough came with the discovery that actinonin, a naturally occurring antibacterial agent, had PDF inhibition as its mode of action. [25, 32] X–ray crystallography showed actinonin binding to the metal cation in a bidentate manner through its hydroxamic acid group. [33] This turned out to be a substantially stronger interaction than what the monodentate inhibitors had previously produced, as demonstrated by inhibitory concentrations reported in the single–digit nanomolar range. [25] Hydroxamic acid has since become the dominating metal–chelating functional group amongst synthetic PDF inhibitors, including all four inhibitor that have reached clinical trials. [34–37]

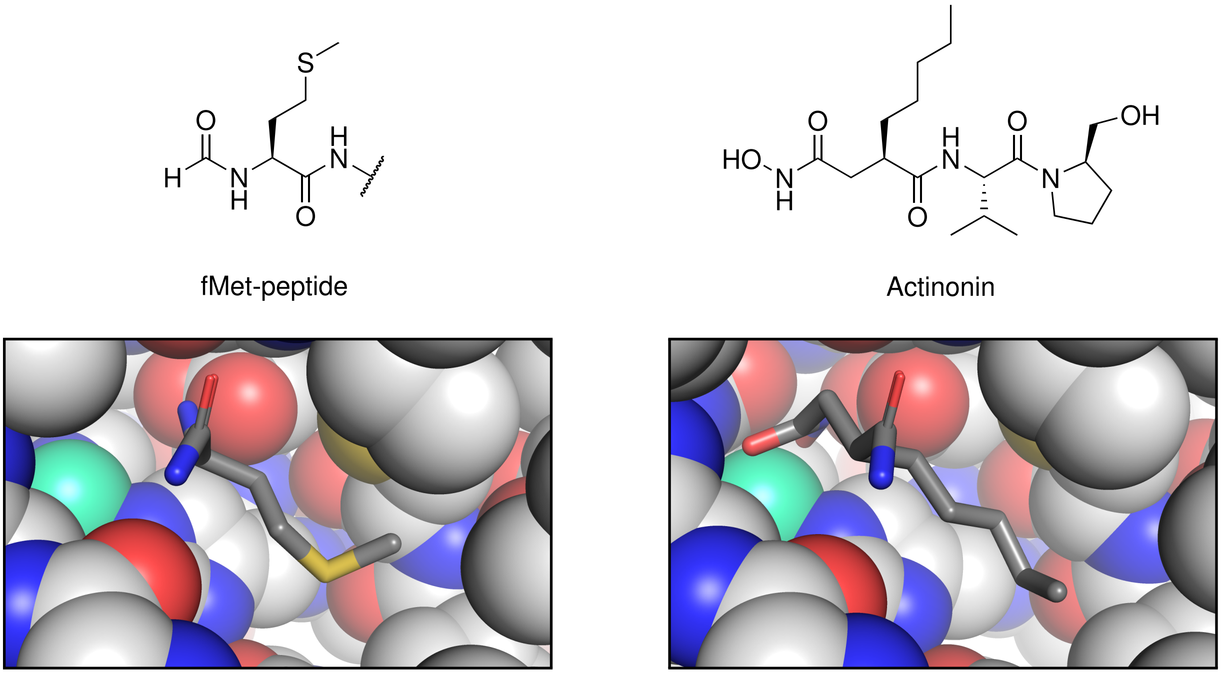

Figure 1.4: Top: Structural comparison of the fMet–peptide substrate (left) and the natural PDF inhibitor actinonin (right). Bottom: Sphere visualisation of the *E. coli* Ni–PDF active site in complex with tripeptide Met–Ala–Ser (left) and actinonin (right). Both show respective side chain protruding into a nearby hydrophobic pocket (obstructing atoms omitted for clarity). Atomic colours, except enzyme carbons in white and nickel in light green. PDB IDs: 1BS6 and 1G2A, respectively. [26, 33]

Around the same time as the first actinonin studies were published, researchers discovered two versions of PDF in the small flowering plant *Arabidopsis thaliana*. [38] Soon after, a human version was identified. [39] This revealed PDFs to be more common than previously believed, a surprising result given the consistent use of regular methionine as protein synthesis initiator in non–bacterial cells. The only exceptions to this rule occur inside mitochondria and plastids, two cellular structures where protein formation proceeds exclusively with fMet as the initiator. Proteins formed in these structures are few in number (< 90) and have been observed with formyl groups retained, making the importance of deformylation uncertain. [40, 41] Nevertheless, the newly discovered PDFs were identified as mitochondrial and plastidic, suggesting they may have a related function. [42]

The existence of human mitochondrial PDF has naturally raised doubts on PDF as an antibacterial target. Actinonin was quickly shown to inhibit human PDF, and yet has not been found toxic in studies on healthy mice. [33, 39, 43] It has, on the other hand, shown antitumor activity against several cancerous cell lines, implying that mitochondrial PDF is essential in cells that grow rapidly. [44] Since it remains unclear what role – if any – human PDF has in normal cell function, it is of great interest to develop inhibitors that are active against bacterial PDF only.

Designing selective inhibitors relies on exploiting chemical or structural differences between bacterial and human PDF. Remarkably, non–bacterial PDFs retain most of the key features from their bacterial counterparts including similar protein folds with near–identical structural motifs (Figure 1.5). [45, 46] The actual catalytic site remains virtually unchanged with six out of seven amino acids being equal to those found in bacteria, resulting in little to no difference in catalytic pathways. [46–48] As such, any potential selectivity must come from structural differences alone.

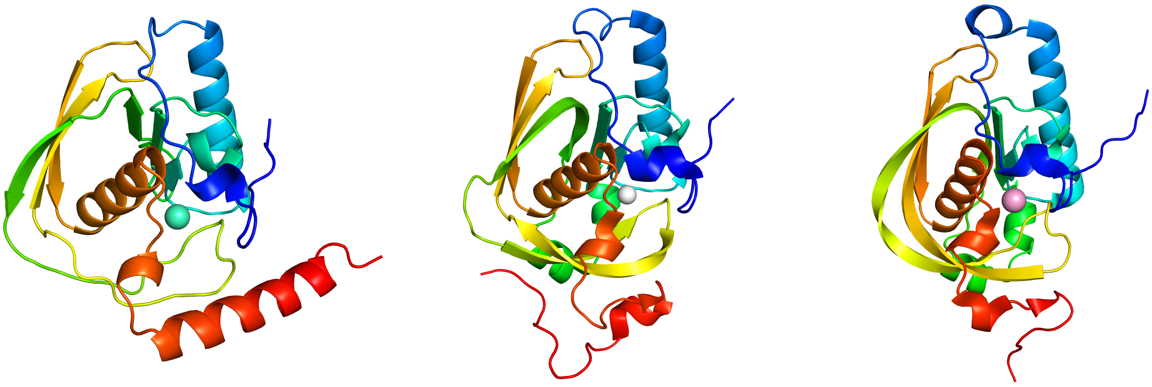

Figure 1.5: Rainbow cartoon visualisation of three different PDFs representing three widely different organisms. From left to right: *E. coli* Ni–PDF, *A. thaliana* Zn–PDF1A, *Homo sapiens* Co–PDF. Metal cations are depicted as light green, white, and pink spheres, respectively. PDB IDs: 1BS7, 1ZY0, and 3G5P. [27, 45, 46]

The most substantial active site difference lies in the hydrophobic side pocket, which is notably shallower in non–bacterial versions (Figure 1.6). [45] A study by the Meinnel group showed that bulkier fragments like phenyl do not fit the pocket of human PDF, a result which led them to develop a series of bulky indole–based hydroxamic acids that showed excellent selectivity towards bacterial PDF. [48, 49] Their leading candidate, colloquially named AB47, consisted of a 5–bromoindole core attached to an acetohydroxamic acid fragment (Figure 2.1). The bromine atom was said to protrude deeply into the hydrophobic pocket, succesfully mimicing methionyl in bacterial PDF while failing to enter the active site of human PDF.

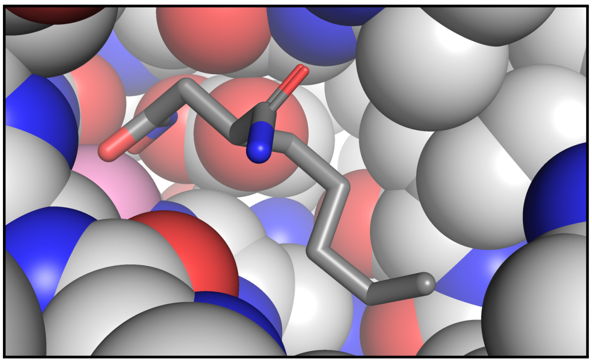

Figure 1.6: Sphere visualisation of *H. sapiens* Co–PDF in complex with actinonin, showing a narrowing of the hydrophobic pocket compared to in *E. coli* PDF (Figure 1.4). Obstructing atoms are omitted for clarity. Atomic colours, except protein carbons in white and cobalt in pink. PDB ID: 3G5K. [46]

The field of selective PDF inhibitors has somewhat stagnated since the publication of AB47 in 2007. Two years after its discovery, Meinnel and affiliates improved the activity by attaching a benzyl motif to the indole nitrogen (Figure 1.7). [50] A few years later, the same groups developed a more potent oxadiazole series, identifying an additional hydrogen bond involving the heterocycle oxygen as a key interaction for achieving tighter binding. [51] Its activity towards human PDF is yet to be investigated, with no further development having been published since 2016. [52]

Meanwhile, the four PDF–inhibiting drug candidates that have entered clinical trials have since been discontinued or put on hold. [23, 53–55] These were pseudopeptide structures heavily based on actinonin itself, albeit with largely different structural elements past the first internal peptide bond. [34–37] Rapid development of antibacterial resistance is suspected to be the main concern, although problems around selectivity may also play a part. [17, 22, 54] As it stands, the potential of PDF inhibition remains unproven. [23]

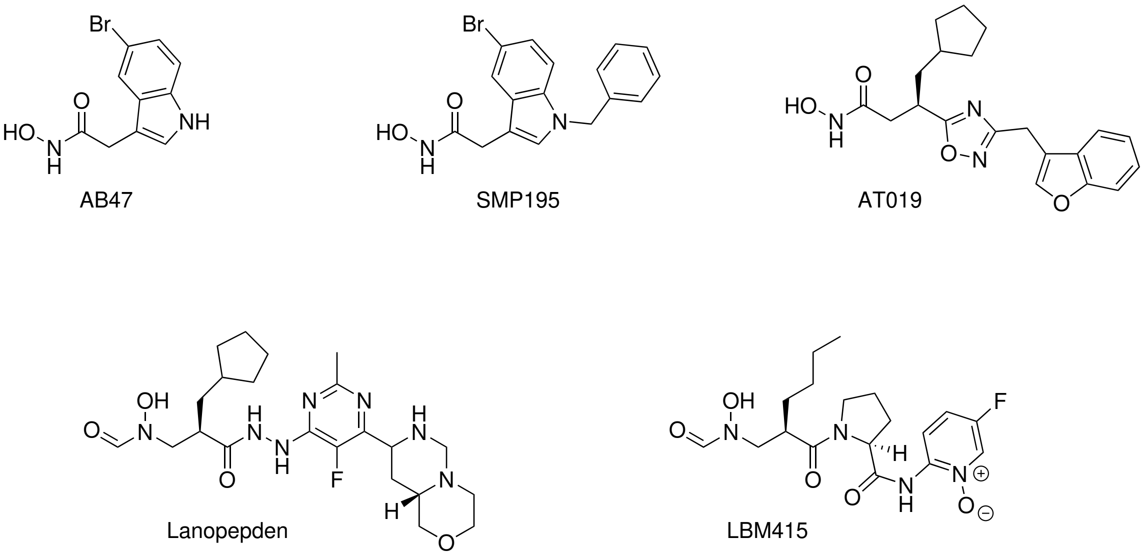

Figure 1.7: A collection of PDF inhibitors, including the selective indoles AB47 and SMP195. AT019 represents the oxadiazole series, while Lanopepden and LBM415 are two drug–candidates that entered clinical trials. The latter two are examples of "reverse" hydroxamic acids, where the chelator nitrogen is tertiary. Structures were obtained from refs. 34, 36, 49, 50, 52.

1.3 Motivation for this work

The contents of this thesis represent the first work on PDF inhibitors conducted in the Sandtorv group. The long–term goal of this project is to develop an understanding of what makes a good PDF inhibitor, and use that to synthesise new drug candidates with greater potency and selectivity than what has previously been observed. To achieve this, the group partnered with the group of Dr. Hans–Petter Hersleth at the Department of Biosciences, University of Oslo, which has an ongoing project studying the expression and inhibition of catalytically active PDFs. This collaboration allows for an iterative cycle where freshly synthesised target molecules are tested for inhibitory porperties against PDFs of differenct origins, the results of which influence the design of new target molecules to be synthesised.

The focus of this first study was to determine the effects of different structural properties on the overall potency of indole–based PDF inhibitors. In the initial planning phase, the indole series stood out as the only inhibitor series with a documented selectivity towards bacterial PDF, thus making it an interesting base structure to explore. While the hydroxamic acid moiety has a long–standing history in the field, the indole scaffold came as a result of an undisclosed medium–throughput screening of bulky, cyclic compounds. [25, 33, 49] As such, it remained unclear which exact structural properties were important for inhibition, and which could be altered or removed to improve the inhibitory response. To assess this, analogues of the indole–based inhibitors with certain altered properties would be synthesised and tested for inhibitory activity. Due to its simple strucure, AB47 was chosen as the benchmark molecule to beat.

2

Aim of the study

The aim of the study was to explore the structural elements of indole–based PDF inhibitors and assess their influence on PDF inhibition. The benchmark molecule AB47 was deconstructed into three key parts; a metal–binding chelator, a bulky central scaffold, and a far–reaching methionyl mimicker (Figure 2.1). AB47 was to be synthesised alongside structural analogues where these key elements were altered.

Figure 2.1: The structure of AB47 alongside a decomposition of its key structural elements. Note that the molecule is redrawn compared to in Figure 1.7.

Three target scaffolds with different properties were envisioned, including benzimidazole, benzotriazole, and indene (Figure 2.2). The metal chelator was to be altered by making the corresponding hydrazides. The methionyl mimicker was left unchanged in this study.

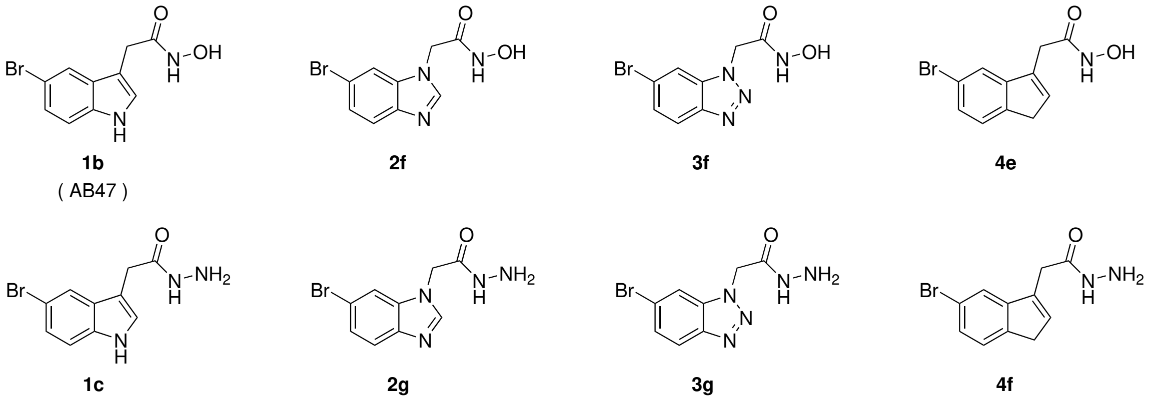

Figure 2.2: Selective PDF inhibitor AB47 and the analogues to be synthesised in this thesis. Top row: Target molecules with differing central scaffolds. Bottom row: Target molecules where the metal–chelating hydroxamic acid is replaced with hydrazide.

3

Synthesis and Discussion

Based on analyses in literature, we deconstructed AB47 into three key structural elements; a metal–binding chelator, a bulky central scaffold, and a far–reaching methionyl mimicker. [48,49] Of the three, the central scaffold had been explored the least, making it the primary fragment to be studied in this thesis. At the time, an indazole analogue had showed similarily potentcy to AB47, while a "reverse–indole" structure with the hydroxamic acid attached on the nitrogen had proven noticably less effective. [50]

With this in mind, we prepared synthetic routes to four target molecules of differing scaffolds. The target of Route I was simply the benchmark molecule, synthesised for use as a comparison during biochemical testing. With the other three, we wanted to assess whether the indole scaffold had a specific influence on potency aside from being just hydrophobic and bulky. As such, the indole core was to be replaced with three similarily sized bicyclic scaffolds, all with slightly different properties. Route II would yield the benzimidazole structure, in which the indole nitrogen is changed from a hydrogen donor to a hydrogen acceptor, possibly forming different hydrogen bonds with the enzyme. Route III would yield the benzotriazole structure, where the second hydrogen–accepting nitrogen would allow for additional interactions to form. Lastly, Route IV would yield the corresponding indene structure, in which the influence of the nitrogen is removed altogether.

The metal chelator fragment had, as opposed to the scaffold, seen some variation in literature. Several bidentate functional groups had been explored, with groups like carboxylic acid, α–hydroxy carbonyl and α–sulfhydryl carbonyl proving largely ineffective. [?] Within the wider indole series, only hydroxamic acids produced nanomolar inhibitory concentrations, implying that the extra heteroatom is essential for sufficient metal–binding. The structurally similar hydrazide group has, however, showed some albeit weaker chelating properties in other PDF inhibitor series. [56, 57] Therefore, as a secondary focus of this thesis, hydrazide analogues of all target molecules would be synthesised to assess its metal affinity in the context of this selective inhibitor series.

Of the three key fragments identified, the methionyl mimicker had seen the most variation in literature. Substituents like halogens, methyl, metoxy, methylthio, and cyclopropyl had all been explored, with bromine proving most effective ahead of chlorine. [49,50] The exact substituent position was also briefly scoped, indicating a strong need for a methionyl mimicker on C5 or C6 specifically. Given the extensive research already conducted on this fragment and its position, no attempts at altering its properties were made in this thesis.

3.1 Route I: Indole benchmark

Route I consisted of one net reaction; a peptide coupling between hydroxylamine and the commercially available indolylacetic acid **1a**, yielding the corresponding hydroxamic acid **1b** (AB47) as the product. The reaction was performed as reported by the Meinnel group in their original indole article, using 1–hydroxybenzotriazole (BtOH) and the hydrochloride salt of 1–ethyl–3–(3–dimethylaminiopropyl)carbodiimide (EDCI) as coupling agents, *N*–methylmorpholine (NMM) as an amine base, and hydroxylammonium chloride as the source of hydroxylamine (Scheme 3.1). [49]

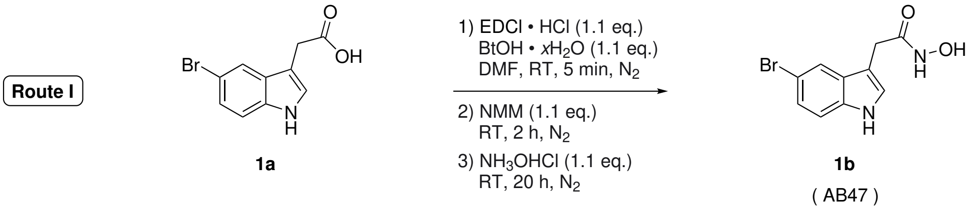

Scheme 3.1: Peptide coupling reaction of indolyl carboxylic acid **1a** with hydroxylammonium chloride forming indolyl hydroxamic acid **1b**; the selective PDF inhibitor AB47 and the target of Route I. Adapted from ref 49.

The reaction proceeded as expected, producing target molecule **1b** as a white solid at a yield of 30 %. The terminal hydroxamic acid moiety was easily identified by two characteristic ^{1}H NMR signals at 10.60 and 8.77 ppm, with the overall spectroscopic data fitting well with those reported in literature (Figure 6.1). [49] The yield was noticeably lower than the reported yield of 55 %, likely the result of a more extensive work–up procedure. To ensure a high purity suitable for testing, the crude product was recrystallised twice from a mixture of acetone and cyclohexane as opposed to only once, followed by an additional washing with pure cyclohexane. This likely caused significant loss of material, but was ultimately effective at removing trace contaminations as seen by its ^{1}H NMR spectrum.

Despite the otherwise high degree of purity, there remained a considerable amount of solvent in the final product. Solid form **1b** was found to trap acetone excellently, with integration of the ^{1}H NMR spectrum revealing a compound–to–acetone ratio of approximately 2:1. Neither high–vacuum drying (24 h) nor vacuum oven drying (80 °C, overnight) proved effective at reducing the relative acetone content, implying that the solvent molecules were tightly bound.

This was somewhat to be expected given the high number of hydrogen–bonding groups present in the structure. The acetone could be exchanged by dissolving the compound in ethyl acetate, however the resulting compound–to–solvent ratio remained near 2:1 following rotary evaporation (Figure A1). This recurring ratio might imply that the solvent is involved in the crystal packing, perhaps as a bridging unit between two molecules of **1b**, although no X–ray crystal structure was obtained to verify this claim. Regardless, the originial Meinnel article made no mention of solvent cocrystallisation taking place, implying that the obtained compound can be isolated fully. Solvent cocrystallisation is a possible explanation for the apparent difference between measured (137–140 °C) and reported (145 °C) melting point ranges. [49]

3.2 Route II: Benzimidazole scaffold

Designing a route to the benzimidazole scaffold required careful consideration of where to begin. Directly using bromobenzimidazole as the starting structure would allow for a short, two–step synthesis of target molecule **2f**, although issues around regioselectivity are likely to arise when N–alkylating an asymmetric benzimidazole. [58, 59] The selected approach was therefore to ring–close the imidazole from an appropriately substituted benzene, thus avoiding regioselectivity at the cost of adding several steps to the route. The final route was heavily inspired by Brooks *et al.*, who synthesised a clinical drug candidate containing an N–alkylated 6–cyanobenzimidazole using a similar strategy. [60]

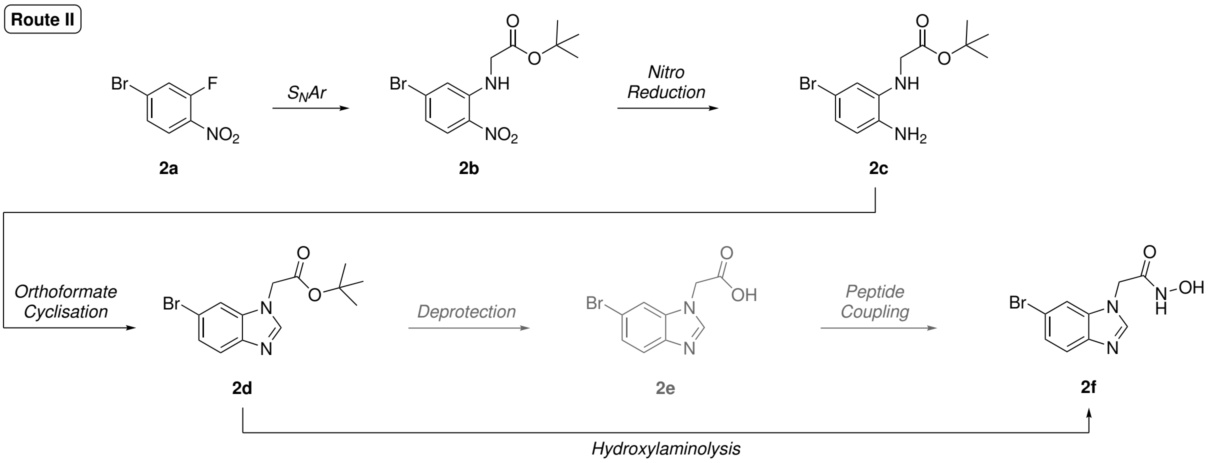

Scheme 3.2: The proposed route to the benzimidazole hydroxamic acid **2f**, going through at least four steps starting from bromofluoronitrobenzene **2a**.

Route II is a four–step synthesis going from bromofluoronitrobenzene **2a** to the benzimidazole analogue of AB47 (**2f**) (Scheme 3.2). Starting with **2a**, an alkylated amine is attached *ortho* to the nitro group through a nucleophilic aromatic substitution reaction (S_NAr). The substitution pattern is established in advance by the given isomer of **2a**, in which the bromo and nitro substituents are oriented *para* to each other. The amine used is *tert*–butyl glycinate, which introduces the necessary carboxyl motif. Reduction of the nitro group yields a nucleophilic *ortho*–diamine **2c** that readily cyclises with an orthoformate to form the benzimidazole scaffold.

The hydroxamic acid functionality is introduced either directly from ester **2d** through hydroxylaminolysis, or from the corresponding carboxylic acid **2e** through a peptide coupling. Both of these approaches have previously been reported by the Meinnel group. [49] The latter option, if utilised, requires a separate removal of the ester group, making this alternative route five steps long.

3.2.1 Attaching glycinate fragment to compound 2a

The first step of Route II was the S_NAr reaction between bromofluoronitrobenzene **2a** and the hydrochloride salt of *tert*–butyl glycinate, forming nitroaniline **2b**. The reaction was performed close to what Brooks *et al.* reported, including a stirring time of 4 days at room temperature with potassium carbonate present as a base. [60] The limiting reagent was, however, changed from the amine to the substituted benzene to increase conversion of **2a** (Scheme 3.3).

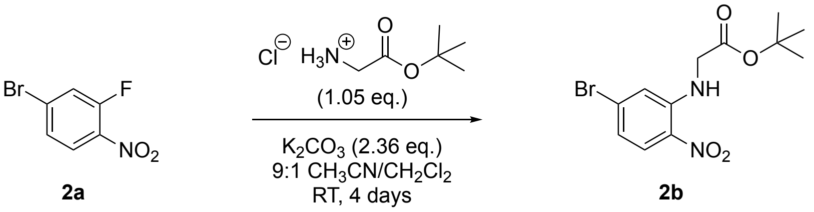

Scheme 3.3: Nucleophilic aromatic substitution (S_NAr) of bromofluoronitrobenzene **2a** and *tert*–butyl glycinatium chloride, forming nitroaniline **2b**. Adapted from ref 60.

The reaction proceeded as expected, producing **2b** as a bright yellow solid at a yield of 79 %. The resulting ^1H NMR spectrum revealed a set of six signals easily identified by basic spectrum analysis; a singlet at 1.44 ppm from *tert*–butyl, a doublet at 4.19 ppm from methylene, a broadened triplet at 8.39 ppm from the secondary amine, as well as two doublets and one doublet of doblets between 8.00 and 6.89 ppm characteristic of a 1,2,4–trisubstituted benzene (Figure 6.4). The compound was not previously described apart from in patents, although different esters with and without bromine have been reported. [61,62] The obtained yield appeared to be in the lower end of the 75–95 % range found in literature.

As it stands, it is unclear whether further optimisation of the reaction conditions will result in higher yields. ^1H NMR spectra of crude products often revealed there to be 10–15 mol % of leftover **2a**, as well as trace amount of 5–bromo–2–nitroaniline, the product of an S_NAr reaction between **2a** and ammonia. This side product likely arises from traces of ammonium chloride being present in the *tert*–butyl glycinate hydrochloride salt, ammonia being the standard reagent in glycine production. [63] A larger excess of glycinate may therefore result in both higher conversion and more contamination, especially since the more challenging chromatographic separation is between **2b** and 5–bromo–2–nitroaniline. As such, the current iteration of the S_NAr procedure was deemed sufficient for the purposes of this thesis.

3.2.2 Formation of key *ortho*–diamine intermediate 2c

With the glycinate fragment in place, nitroaniline **2b** was to be reduced to the corresponding *ortho*–dianiline **2c**. Brooks *et al.* had performed a nitro reduction alongside an imidazole ring–closure as a one–pot reaction using iron metal, formic acid and triethyl orthofromate as reagents. [60] Seeing as **2c** was planned to be a crucial intermediate in Route III, it was decided that the nitro reduction would be considered a unique step with its own work–up procedure. As such, a separate set of conditions unlike those by Brooks *et al.* would have to be defined.

Nitro groups readily reduce to primary amines in a multitude of ways, for instance by base metals like iron and zinc in the presence of acid. [64] As a first attempt, **2b** was reacted with iron metal in neat acetic acid at room temperature, as reported by Hylland *et al.* who successfully reduced nitro–containing biphenyl– based metal–organic framework (MOF) linker molecules using identical conditions (Scheme 3.4). [65]

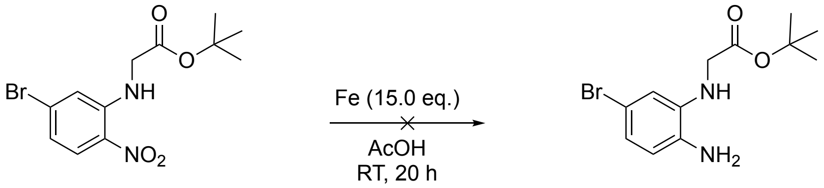

2b **2c**

Scheme 3.4: Iron–mediated reduction of nitroaniline **2b** into *ortho*–diamine **2c** in neat acetic acid. Adapted from ref 65.

These conditions proved to be ill–suited for the intended transformation. The ^{1}H NMR spectrum of the crude material revealed substantial amounts of unreacted **2b**, alongside numerous other signals of unknown origins (Figure 3.1). No product signals from **2c** could be identified, however a broadened singlet at 10.39 ppm stood out as a characteristic resonance. Signals in this region of the spectrum are often from exchangeable hydrogens bonded to oxygen or nitrogen, although this particular signal appeared too sharp and too shielded for it to arise from the corresponding carboxylic acid of **2b** or **2c** usually expected around 11–12 ppm. [64, 66] Suspecting a nitrogen–bonded hydrogen, questions arose whether **2c** was partaking in an undesirable side reaction.

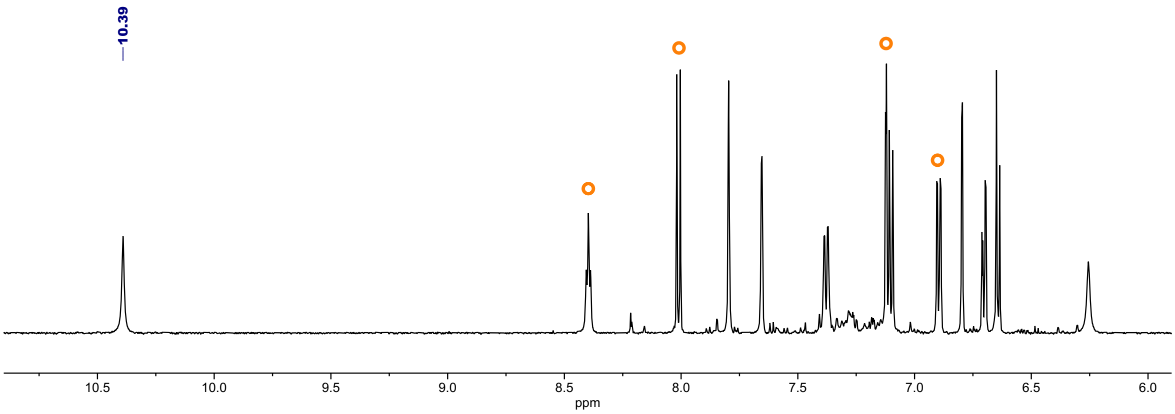

Figure 3.1: ^{1}H NMR (600 MHz, DMSO–d$_6$) spectrum of the crude material from the reaction in Scheme 3.4. Signals from leftover **2b** are marked with orange circles. No signals from *ortho*–diamine **2c** could be identified, but the signal at 10.39 ppm stood out as an unexpected resonance from an exchangable hydrogen. For full spectrum see Figure A2.

Given the acidic environment, the carbonyl group of **2c** was likely to be activated towards nucleophilic attack. An intramolecular cyclisation was proposed, in which the primary amine of **2c** reacts with the *tert*–butyl ester forming dihydroquinoxalinone **2x** as a side product (Scheme 3.5). This would require the formation of a second six–membered ring, a ring size that is known to be favourable in many ring–closure reactions. [66] The attacking nitrogen would formally end up as a secondary amide, fitting with the high chemical shift of 10.39 ppm observed in the crude material. Using ^{1}H–^{15}N HMBC, this signal was later confirmed to arise from a nitrogen–bonded hydrogen, with a ^{15}N chemical shift of 129.9 ppm being well within the normal range for amides at 95–145 ppm (relative to liquid ammonia, Figure A3). [67] Literature searches have since revealed dihydroquinoxalinone syntheses with near–identical conditions, suggesting the proposed side reaction to be correct. [68]

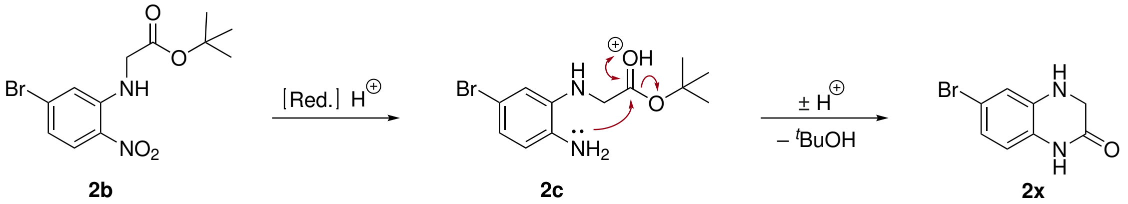

Scheme 3.5: Generalised nitro reduction of **2c** in acidic media, conditions that allow for an intramolecular cyclisation to dihydroquinoxalinone **2x**. [68]

Believing the proposed side reaction to be taking place, the focus shifted towards acid–free reaction conditions that perhaps would not trigger the cyclisation. The common method of hydrogenation over palladium was attempted, using similar conditions to those described by Folkertsma *et al.* (Scheme 3.6). [69]

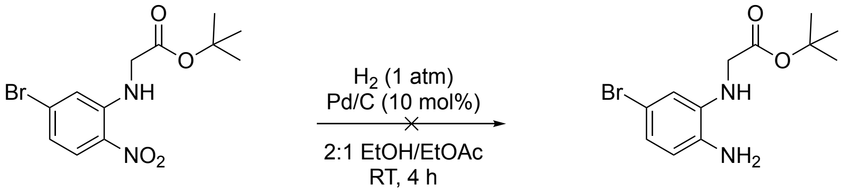

2b **2c**

Scheme 3.6: Palladium–catalysed hydrogenation of nitroaniline **2b** into *ortho*–diamine **2c**. Adapted from ref 69.

The reaction proceeded with a gradual loss of colour, suggesting total conversion of **2b**. This was confirmed by the ^{1}H NMR spectrum of the crude material, although a broad singlet above 10 ppm was once again observed. Moreover, the spectrum revealed a series of aromatic signals with coupling patterns unlike those expected of 1,2,4–trisubstituted benzenes, with some being noticeably triplet–like (Figure 3.2). Treatment of a Gaussian window function on the free induction decay (FID) produced a ^{1}H NMR spectrum containing four triplets of doublets (td), a coupling pattern that can only occur in benzenes when they are *ortho*–disubstituted. [66] This meant that hydrodehalogenation had occured, in which the bromine substituent had been replaced by a hydrogen.

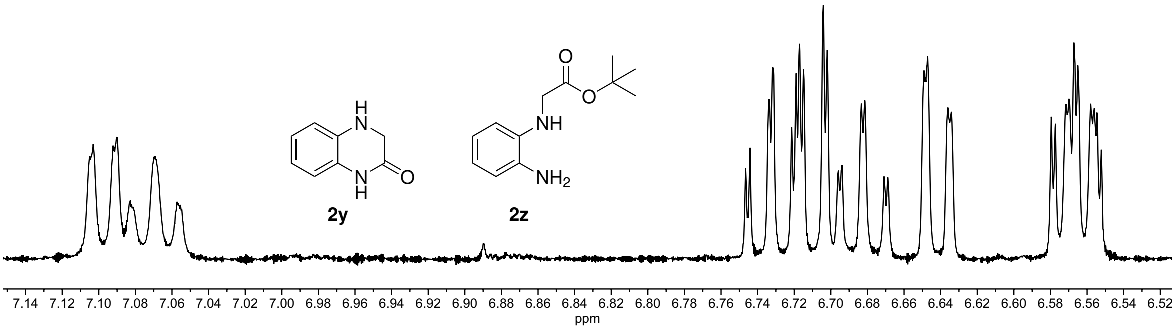

Figure 3.2: ^{1}H NMR (600 MHz, DMSO–d$_6$) spectrum of the crude material from the reaction in Scheme 3.6, processed with a Gaussian window function (LB = −0.60 Hz, GB = 0.30). No signals from *ortho*–diamine **2c** could be identified. Instead, multiple triplets of doublets (td) were observed, indicating hydrodehalogenation to have occurred. The material was most likely a mixture of side products **2y** and **2z**.

There being four triplets of doublets in the ^{1}H NMR spectrum meant that two major side products, both *ortho*–disubstituted, were present in the sample. One was presumably the unsubstituted analogue of **2x**, easily identified by the characteristic broad singlet at 10.19 ppm (Scheme 3.7). The second was likely the bromine–lacking analogue of *ortho*–diamine **2c**, indicated by an intense singlet at 1.43 ppm characteristic of *tert*–butyl with a favourable integral relative to the aromatic signals (**??**). While a shorter reaction time might have led to less intramolecular cyclisation, trying to avoid hydrodehalogenation during nitro group reduction is reported in literature to be a major challenge not possible with simple metal catalysts. [70, 71] As such, the search for suitable conditions continued.

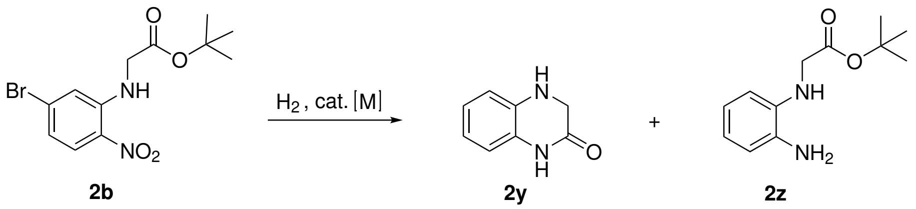

Scheme 3.7: Generalised metal–catalysed hydrogenation of **2c**, conditions that trigger hydrodehalogenation, yielding both dihydroquinoxalinone **2y** and *ortho*–diamine **2z**. [?, 71]

From here, the focus returned to metal–mediated reductions, this time in mildly acidic media to limit cyclisation. In 2019, Kallinen *et al.* reported a successful nitro reduction of an *iso*–propyl ester similar to **2b** using iron powder and ammonium chloride. [72] The particular reaction was activated using ultrasound, although other reductions were performed using mild heating (40 °C). To allow for monitoring by ^{1}H NMR, an adapted procedure using zinc powder was attempted (Scheme 3.8).

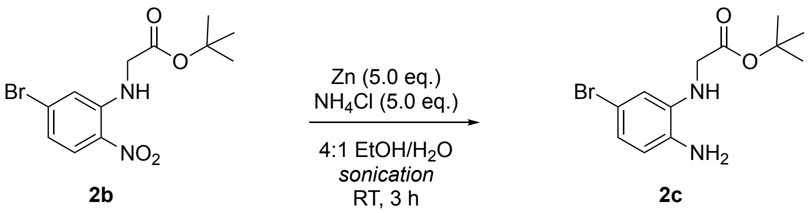

Scheme 3.8: Zinc–mediated reduction of nitroaniline **2b** into *ortho*–diamine **2c** in the presence of aqueous ammonium chloride. Adapted from ref 72.

The resulting ^{1}H NMR spectrum of the crude material showed, for the first time, signals belonging to the intended product **2c** (Figure 3.3). The signal from the primary amine appeared as a clearly visible broad singlet at 4.69 ppm, while the signal from the secondary amine saw a 3.2 ppm drop in chemical shift due to the sudden change in electron density. At a 0.40 mmol scale, the reaction showed full conversion after three hours of ultrasound, and the product could be obtained at a yield of 46 % after purification by column chromatography.

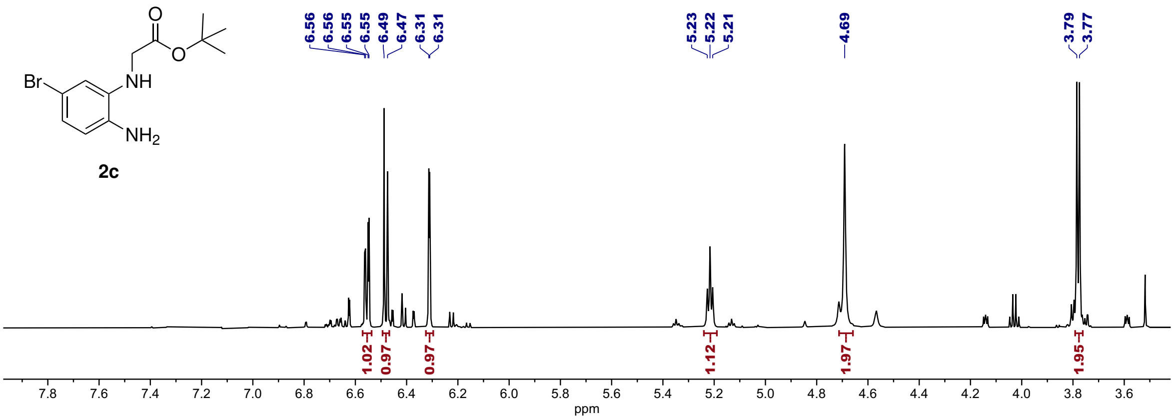

Figure 3.3: ^{1}H NMR (600 MHz, DMSO–d$_6$) spectrum of the crude material from the reaction in Scheme 3.8. Signals marked with chemical shifts arise from **2c**, the major species. For full spectrum see Figure A4

However, these conditions proved to be insufficient when attempting the reaction on a 1.20 mmol scale, with poor conversion of **2b** even after five hours of ultrasound treatment. Given the heterogenous nature of the reaction mixture, it is likely that flask size and surface area were important parameters for the progression of the reaction. To circumvent this upscaling issue, further optimisation of reaction conditions were conducted.

With zinc, the reaction was shown to work thermally at 40 °C, albeit less cleanly than with ultrasound. When switching to iron, thermal heating at 40 °C produced **2c** more selectively at the expense of a slow reaction rate. Conversely, heating at 80 °C gave side product **2x** exclusively. Heating at 60 °C turned out to be the suitable middle ground, achieving full conversion of **2b** with a relatively low degree of side product formation (Scheme 3.9).

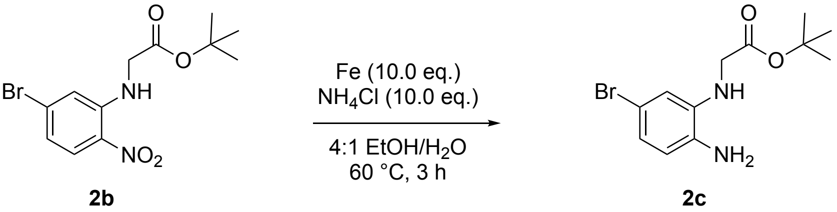

Scheme 3.9: Iron–mediated reduction of nitroaniline **2b** into *ortho*–diamine **2c** in the presence of aqueous ammonium chloride. Optimised from ref 72.

With these conditions, the reduction of **2b** to **2c** was performed at multiple scales of up to 2.40 mmol with obtained yields of 50–56 %. Flask size turned out to be a crucial parameter, with a reaction mixture volume of 16 mL requiring a 100 mL–sized round–bottomed flask to achieve full conversion. In all cases, the final product remained contaminated with trace amount of **2x** after column chromatography, and was therefore stored at −20 °C as a precaution to minimise potential cyclisations occuring spontaneously.

In literature, *ortho*–diamines with similar glycinate fragments tend to be used as crude intermediates, and are not typically isolated. A literature yield range is therefore unobtainable. The exact structure of **2c** has only been described in patents, and similar structures with different substituents are generally not accompanied by characterisation data. [62, 72, 73]

3.2.3 Ring–closure to benzimidazole scaffold

The next step of Route II was the ring–closure reaction of *ortho*–diamine **2c** with an orthoformate to form benzimidazole **2d**. The intention had been to perform the reaction similar to that described by Brooks *et al.* using a homogenous solution containing **2c**, triethyl orthoformate, and formic acid. [60] However, given the aforementioned acid sensitivity of **2c**, questions arose whether the orthoformate could instead be used directly as the solvent, thus maximising the chances of ring–closure occurring before intramolecular cyclisation. The reaction was therefore attempted as described by Wang *et al.*, who synthesised a novel oxoindolinyl–substituted benzimidazole using only triethyl orthoformate and a catalytic amount of tosylic acid (Scheme 3.10). [74]

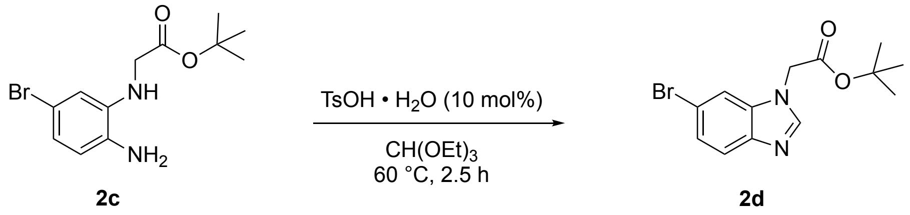

Scheme 3.10: Acid–catalysed imidazole ring–closure of *ortho*–diamine **2c** and triethyl orthoformate into benzimidazole **2d**. Adapted from ref 74.

The reaction proceeded as described, with **2d** being formed as a beige solid at a yield of 87 %. In the ^{1}H NMR spectrum, the formation of a benzimidazole ring was indicated by a new singlet at 8.21 ppm as well as the disappearance of the two amino signals (Figure 6.10). The methylene hydrogens also saw a 0.45 ppm increase in chemical shift relative to in **2c**. The product was shown to contain some trace organic impurities, but purification by column chromatography was considered unecessary due to the planned recrystallisation at the end of route. The compound itself has not been described outside of patents, although the unsubstituted analogue has been reported in literature. [75] The obtained yield fell within the literature range of 70–99 % reported for similar reactions using triethyl orthoformate as the solvent. [76, 77]

3.2.4 Transformation to hydroxamic acid 2f

The last challenge of Route II revolved around converting the *tert*–butyl ester **2d** into the hydroxamic acid **2f**, the benzimidazole analogue of AB47 and the target molecule of the route. This was to be done either by direct hydroxylaminolysis of **2d**, or in a two–step manner by first deprotecting the carboxylic acid group, yielding **2e**, and then performing a peptide coupling with hydroxylamine as described in Route I. The preferred option was naturally the former, given the fewer number of total steps.

Direct hydroxylaminolysis of indole–based ethyl esters was extensively performed by Boularot *et al.* in the Meinnel group article that first spawned AB47. [49] The reaction involved mixing the ester substrate with free hydroxylamine, generated *in situ* by reacting hydroxylammonium chloride with sodium ethoxide. Given the substantially stronger nucleophilicity of hydroxylamine compared to normal amines, it was believed that *tert*–butyl ester **2d** would be able to undergo an equivalent transformation despite its larger steric bulk. [66, 78] To simplify the procedure, sodium ethoxide was replaced with potassium *tert*–butoxide for easier handling (Scheme 3.11).

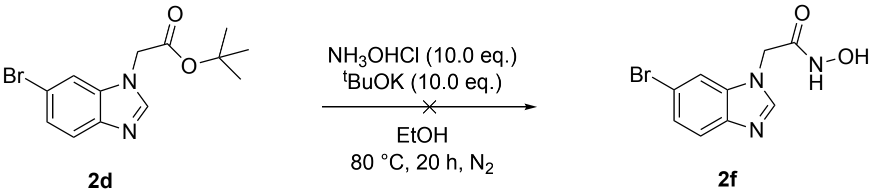

Scheme 3.11: Hydroxylaminolysis of benzimidazolyl *tert*–butyl ester **2d**, forming benzimidazolyl hydroxamic acid **2f**. Adapted from ref 49.

The effectiveness of the proposed reaction remains largely unclear. As described by the reported work–up procedure, upon completion the reaction mixture was evaporated under reduced pressure and extracted using ethyl acetate. [49] The organic phase was washed repeatedly with water, base, and brine before being dried over sodium sulfate and evaporated to a solid. In Route I, as a comparison, this process gave crude **1b** (AB47) at a yield of roughly 60 %. In Route II, this process produced trace amounts of a crude material that could not be identified. If no reaction had occurred, unreacted **2d** should have emerged from the organic phase. This meant that, while a reaction had likely taken place, the resulting product must have been water–soluble and thus been extracted into the aqueous phases.

To sidestep this issue, a second reaction mixture was analysed by ^{1}H NMR following the initial evaporation of solvent. The resulting spectrum revealed one major species which, when compared to the spectrum of **2d**, appeared to be a monosubstituted benzimidazole. While each of the four aromatic signals appeared slightly shifted compared to in **2d**, the broad singlet at 4.97 ppm seemed to have changed more drastically. This signal, if arising from target molecule **2f**, would come from the carbonyl–bonded methylene bridging the chelator and the scaffold. A change in chemical shift at this position is likely to occur if a substitution reaction takes place at the adjacent carbonyl, as seen for instance in the ^{1}H NMR spectra of **1a** and **1b**. Moreover, no appropriately sized *tert*–butyl signal could be identified, furthering the suspicion that a carbonyl substitution truly had occurred.

Despite these indirect pieces of evidence, no actual hydroxamic acid signals were ever present in the ^{1}H NMR spectrum. A potential side product could be the carboxylic acid **2e**, although no carboxylic acid signal was observed either. It is possible that these exchangeable resonances – if present – collapse due to the substantial amount of hydroxylamine left in the sample, as indicated by the large hump centred around 3.32 ppm.

This then highlights a secondary problem, namely that extraction with ethyl acetate and washing with water is performed so as to separate excess hydroxylamine from the hydroxamic acid product. If the target molecule **2f** truly is water–soluble, then a new reaction procedure will have to be designed to ensure the removal of hydroxylamine. One potential approach could be to use hydroxylamine Wang resin, a solid–phase support that has *O*–benzylated hydroxylamine on its surface. Reactions with the resin produce hydroxamate esters that remain attached until cleaved by trifluororacetic acid, allowing for a different work–up procedure. [79] Utilising other separaton techniques like reversed–phase column chromatography could also be considered.

The apparent water solubility was ultimately the reason why carboxylic acid **2e** was never synthesised, and the subsequent peptide coupling was never attempted. This is because water–washing of an organic phase plays an even more important role in the work–up of the peptide coupling, removing all major contaminants from the product including the urea byproduct, the hydroxybenzotriazole, the *N*–methyl morpholine and any excess hydroxylamine. Future attempts at synthesising **2f** should therefore make us of coupling agents whose byproducts are insoluble in water, for instance *N,N'*–dicyclohexylcarbodiimide (DCC), thus allowing for alternative work–up procedures. [80]

3.3 Route III: Benzotriazole scaffold

The design of Route III was essentially the same as that of Route II, making use of the same ring–closure strategy to avoid issues with regioselectivity. In fact, the observation that benzotriazoles can be made from *ortho*–diamines meant that Route III could be a divergent branch of Route II, rather than one starting from scratch (Scheme 3.12). [81] Reacting *ortho*–diamine **2c** with a nitrite source would yield the desired benzotriazole **3d**, going through a diazonium salt intermediate as seen in the Sandmeyer reaction. [64, 82] The hydroxamic acid moiety would then be introduced through direct hydroxylaminolysis, or through a two–step deprotection/peptide coupling approach *via* **3e**.

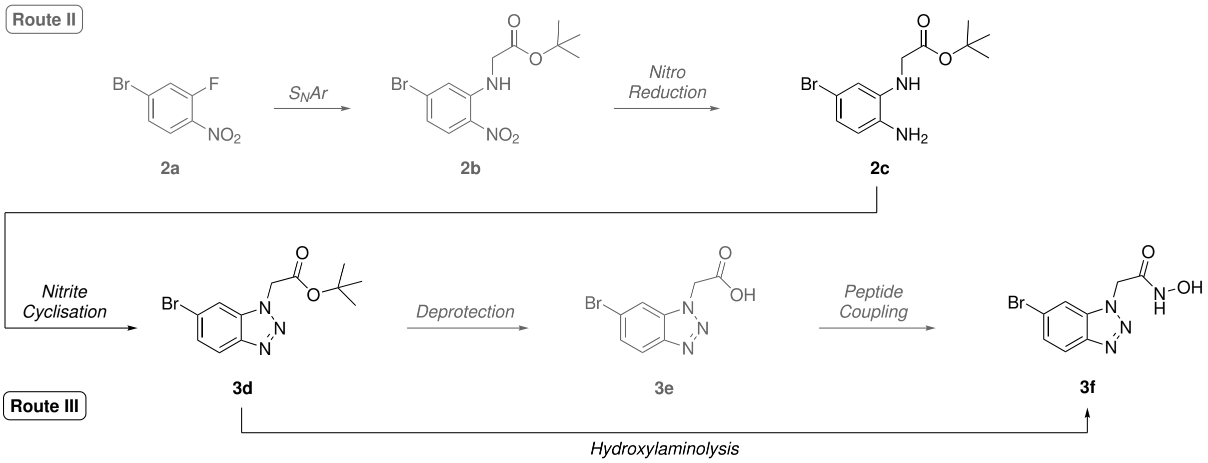

Scheme 3.12: The proposed route to the benziotriazole hydroxamic acid **3f**, branching off Route II at the *ortho*–diamine intermediate **2c**

3.3.1 Ring–closure to benzotriazole scaffold

The first step of Route III was the ring–closure reaction of *ortho*–diamine **2c** with nitrite to form benzotriazole **3d**. Normally, this reaction is performed using sodium nitrite in aqueous acid, forming nitrosonium ions *in situ* that react with the amino groups. [64, 83] However, given the acid sensitivity of **2c**, the focus shifted to surrogates of nitrite that could react without acid being present. The reaction was eventually performed as described by Azeez *et al.*, who reported a high–yielding acid–free method for benzotriazole synthesis using *tert*–butyl nitrite, a readily available alkyl nitrite (Scheme 3.13). [84]

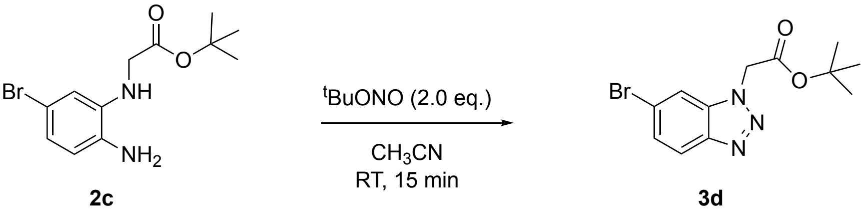

Scheme 3.13: Triazole ring–closure of *ortho*–diamine **2c** and *tert*–butyl nitrite into benzotriazole **3d**. Adapted from ref 84.

The reaction proceeded as described, forming **3d** as a maroon solid at a yield of 93 %. As with benzimidazole, the formation of a benzotriazole ring was indicated in the ^{1}H NMR spectrum by the disappearance of the two amino signals (Figure 6.13). The methylene hydrogens also saw a 0.96 ppm increase in chemical shift relative to in **2c**, a larger change than that seen in Route II. The addition of a third nitrogen was verified using ^{1}H–^{15}N HMBC and high–resolution mass spectrometry (Figure 6.15). The product was shown to contain similar trace organic impurities as the benzimidazole analogue **2c**, and further purification was omitted for the same reasons. The compound itself has at the time of writing not been described, although other esters with and without substituents have been reported. [83,85] The obtained yield was well within the 85–99 % range reported by Azeez *et al.* [84]

3.3.2 Transformation to hydroxamic acid 3f

The transformation of *tert*–butyl ester **3d** into hydroxamic acid **3f** faced similar issues to those described for Route II. To begin with, hydroxylaminolysis of **3d** was attempted so as to potentially save a synthetic step (Scheme 3.14). However, despite using the same conditions as in Route II, the reaction simply retained substrate ester **3d** at a quantitative yields. This result went far in suggesting that a *tert*–butyl ester was an impractical electrophile for carbonyl substitution. The choice of glycinate ester for the S$_N$Ar reaction with **2a** was largely arbitrary, and future attempts at synthesising **3f** *via* Route II should commence with a less sterically hindered glycinate instead.

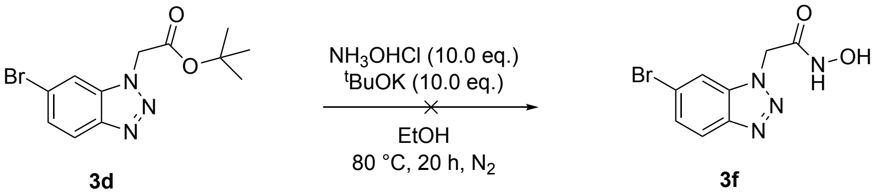

Scheme 3.14: Hydroxylaminolysis of benzotriazolyl *tert*–butyl ester **2d**, forming benzotiazolyl hydroxamic acid **2f**. Adapted from ref 49.

Given the poor reactivity of **3d** towards hydroxylaminolysis, it was deemed necessary to deprotect the underlying carboxylic acid **3e** and attempt the transformation *via* the alternative peptide coupling method. To achieve deprotection, *tert*–butyl ester **3d** was treated with trifluoroacetic acid in dichloromethane as described by Messeguer *et al.* (Scheme 3.15). [86] Although the intermediate **3e** was not fully characterised, its formation was documented by ^{1}H NMR monitoring. The crude carboxylic acid was subsequently treated with EDCI, hydroxybenzotriazole, NMM, and hydroxylammonium chloride, equivalent to as described Route I.

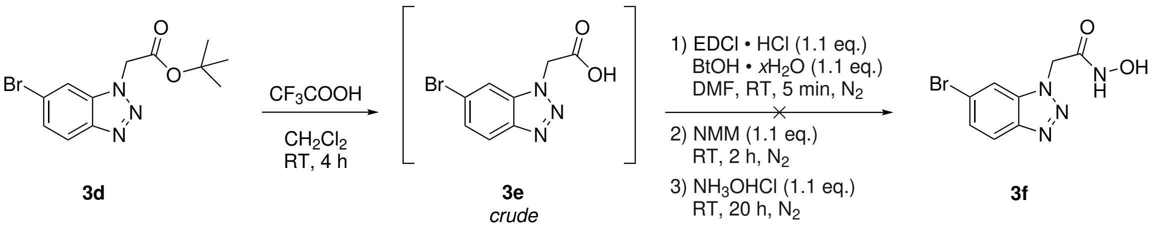

Scheme 3.15: Deprotection of benzotriazolyl *tert*–butyl ester **2d** by trifluoroacetic acid, followed by the peptide coupling between benzotriazolyl carboxylic acid **3e** and hydroxylammonium chloride, forming benzotriazolyl hydroxamic acid **3f**.

Somewhat predictably, the reaction produced only traces of a crude material after the standard extraction work–up procedure. As with the benzimidazole, it appeared that benzotriazole target **3f** was soluble in water. The aqueous phases was indeed found to contain organic material, although its identity was never resolved. Ultimately, Route III was halted alongside Route II pending the reveal of a different peptide coupling procedure.

3.4 Route IV: Indene and related scaffolds

Designing a route to the indene scaffold was largely a choice between reaction conditions, rather than particular synthetic strategies. The most described pathway to indenyl–subtituted esters involves attaching a side chain to a suitable indanone, a pathway which guarantees that the desired substitution pattern is obtained. Common methods for doing this include the aldol–related Reformatsky reaction and the Wittig–related Horner–Wadsworth–Emmons reaction. [87, 88] While the former requires the use of toxic α–haloacetates, the latter has been shown to form mixtures containing both an indene isomer (*endo*) and two stereoisomers of 2–(indanylidene)acetate (*exo*). [88, 89] As such, a safer and seemingly more selective approach using the lithium enolate of ethyl acetate was used, heavily inspired by Alcalde *et al.* who synthesised indene–based serotonin receptor agonists using this method. [90]

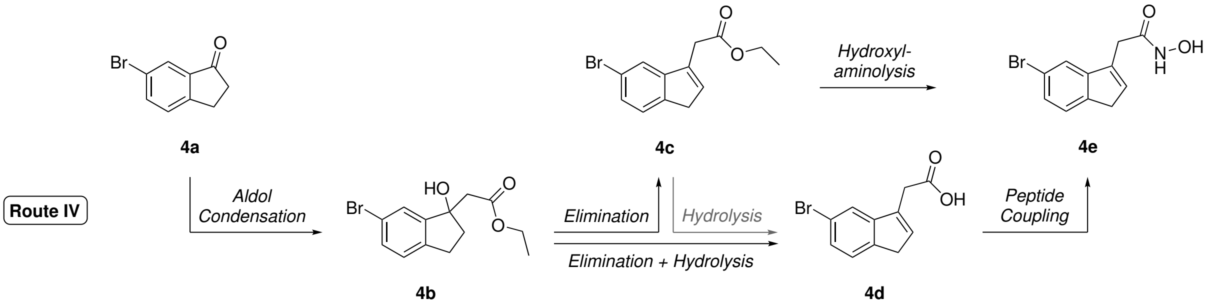

Scheme 3.16: The proposed route to the benzimidazole hydroxamic acid **2f**, going through at least four steps starting from bromofluoronitrobenzene **2a**

Route IV is a three–step synthesis going from 5–bromoindan–1–one (**4a**) to the indene analogue of AB47 (**4e**, Scheme 3.16). Starting with **4a**, ethyl acetate is attached at the ketone carbon through an aldol condensation reaction, forming the β–hydroxyacetate **4b**. Acid–cataysed elimination of water yields the desired indene scaffold, after which the hydroxamic acid is formed either through direct hydroxylaminolysis of **4c** or through a peptide coupling between **4d** and hydroxylamine.

3.4.1 Attaching ethyl acetate to compound 4a

The first step of Route IV was the aldol condensation between bromoindanone **4a** and ethyl acetate, forming β–hydroxyester **4b** (Scheme 3.17). The reaction was performed as described by Alcalde *et al.*, using lithium bis(trimethylsilyl)amine as the strong base. [90]

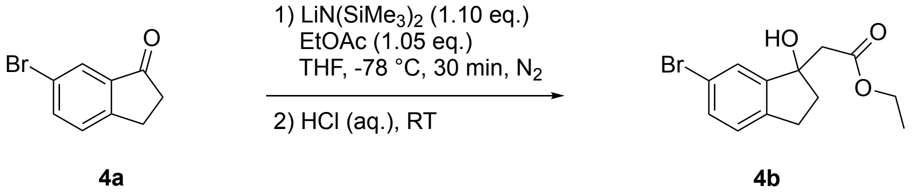

Scheme 3.17: Aldol condensation of ethyl acetate and indanone **4a**, forming β–hydroxyester **4b**. Adapted from ref. [90].

The reaction proceeded as expected, producing **4b** as an orange oil at a yield of 92 %. The resulting ^{1}H NMR spectrum revealed a set of eleven unique signals, most notably six multiplets from four sets of diastereotopic protons and a characteristic singlet at 5.40 ppm arising from the hydroxyl group (Figure 6.16). The exact compound was not previously described, although some differently substituted structures have been reported. [91, 92] Even though Alcalde *et al.* did not report a yield for this step, the obtained yield appeared to be within the 75–95 % range found in literature.

In the ^{1}H NMR spectrum, the methylene group on the ethyl chain appeared as an interesting and highly symmetrical ABX_3 quartet of quartets (**??**, inset). In this multiplet, each subsignal of a second–order AB quartet is itself split into a binomial quartet caused by the adjacent methyl group. [93] All sixteen subsignals could be made visible using a Gaussian window function on the FID.

3.4.2 Resolving *endo* / *exo*–isomerism

The second step of Route IV was the elimination of water from β–hydroxyester **4b**, forming the desired indene scaffold. Alcalde *et al.* had synthesised the nitro–substituted analogue of carboxylic acid **4d** by simply stirring the substrate in 50 % aqueous sulfuric acid, essentially performing water elimination and ester hydrolysis simultaneously. [90] An impressive yield of 80 % was reported, although a discrepancy between the article and the supplementary information has since put this result into question. Nevertheless, as a first attempt, an equivalent experiment was set up using the same conditions (Scheme 3.18).

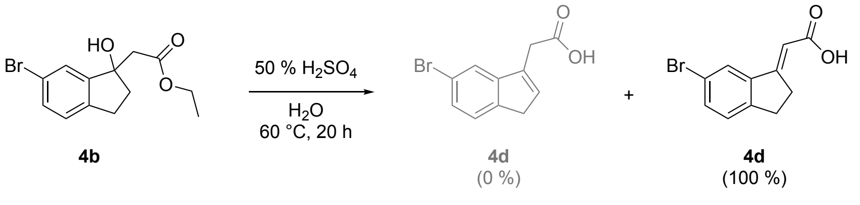

Scheme 3.18: Simultaneous water elimination and ester hydrolysis of β–hydroxyester **4b** in the presence of concentrated aqueous sulfuric acid, forming exclusively indanylidene **5d**. Adapted from ref. 90.

The ^{1}H NMR spectrum of the resulting crude material showed only the undesired (E)–indanylidene isomer **5d**, henceforth referred to as the *exo*–isomer (Figure 3.4a)). The identity of the isomer was deduced using a NOESY experiment, which showed a through–space coupling between the alkene hydrogen and the aromatic ring that would not be present in the *endo* structure (compare **??**). No trace of the (Z)–isomer was observed, making the conditions remarkably selective towards one of three possible isomers. Despite this, the result was ultimately the opposite of what had been reported. [90] Fellow group member I. B. Tangevold later studied this reaction further, revealing decarboxylation of the caboxylic acid products to be taking place. Differing rates in decarboxylation between the *endo*–isomer (**4d**) and *exo*–isomer (**5d**) result in only the latter remaining at the end of the reaction, allowing it to be isolated at yields of 20–30 %. [94]

At the time, the apparent selectivity was believed to be caused by thermodynamic control given the strong acid and moderate heating used in the reaction. The focus therefore shifted to milder reaction conditions with the hopes of forming more of the desired *endo*–isomer. In the same article, Alcalde *et al.* reported some eliminations by using trifluoroacetic acid in dichloromethane at −5 °C (Scheme 3.19). [90]

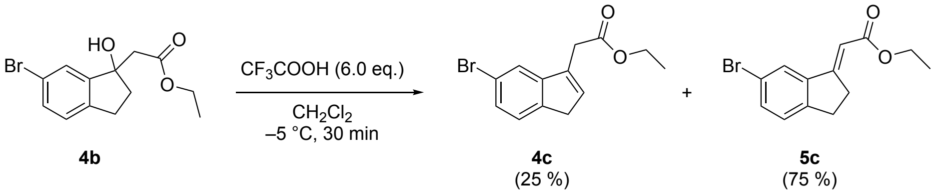

Scheme 3.19: Water elimination of β–hydroxyester **4b** in the presence of trifluoroacetic acid, forming a 25:75 mixture of indene **4c** and indanylidene **5c**. Adapted from ref. 90.

These conditions proved promising, this time forming a mixture of the ethyl esters **4c** and **5c** with an *endo*:*exo* ratio measured to 25:75 by integration of the crude ^{1}H NMR spectrum (Figure 3.4b)). This improvement from the last attempt supported the assumption that the *endo*–isomer was the kinetic product of the elimination reaction. And yet, reducing the reaction temperature did little to increase the *endo*:*exo* ratio, with −40 °C retaining the 25:75 ratio and −78 °C stopping the reaction completely. Although the two esters were found to be separable by column chromatography, the unfavourable isomer ratio meant that the aldol strategy of Route IV could potentially be as inefficient as the Horner–Wadsworth–Emmons reactions reported in literature. [88, 89]

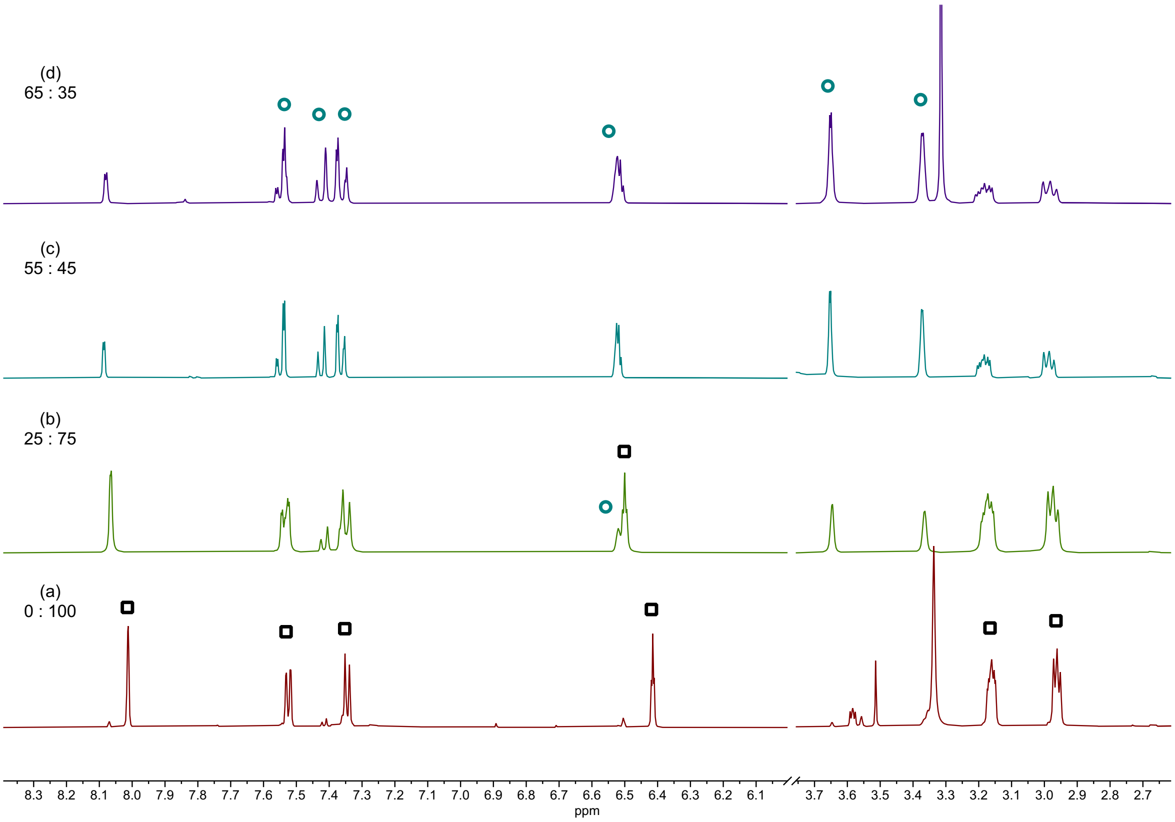

Figure 3.4: ^{1}H NMR (DMSO–d$_6$) spectra of crude mixtures between indene **4c** (*endo*, teal circles) and indanylidene **5c** (*exo*, black squares) after different conditions. Isomer ratio stated as *endo* : *exo*. The *exo*–isomer appears to form first, but the *endo*–isomer is slightly favoured over time. From bottom: a) (600 MHz) H_2SO_4, 60 °C, 20 h b) (400 MHz) CF_3COOH (6.0 eq.), −5 °C, 30 min c) (400 MHz) CF_3COOH (6.0 eq.), RT, 2 days d) (300 MHz) CF_3COOH (24.0 eq.), RT, 24 h.

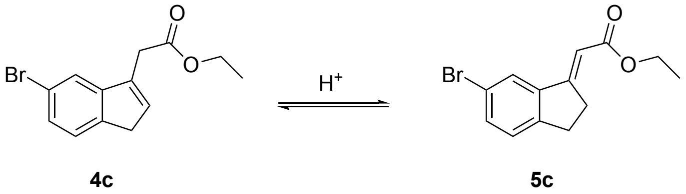

Scheme 3.20: Acid–catalysed isomerisation between indene **4c** and indanylidene **5c**.

However, a major breakthrough came with the observation that the two ester species were isomerising in acidic environments (Scheme 3.20). Two days after monitoring the reaction at −40 °C by ^{1}H NMR, the very same NMR sample displayed an *endo*:*exo* ratio of 55:45 (Figure 3.4c)). Monitoring the equilibrium at room temperature with increasing concentrations of acid found it to stabilise at a ratio of 65:35 (Figure 3.4d)). This meant the initial assumptions were false, and that the *endo*–isomer was in fact the formal thermodynamic product of the elimination reaction. Knowing this, the acid concentration was further optimised to ensure stabilisation of the equlbrium occurred within 24 hours (Scheme 3.21).

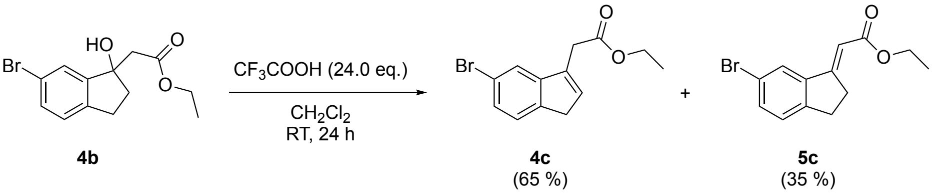

Scheme 3.21: Water elimination of β–hydroxyester **4b** in the presence of trifluoroacetic acid, forming a 65:32 mixture of indene **4c** and indanylidene **5c**. Optimised from ref. 90.

Allowing the equilbrium to stabilise produced crude mixtures that were successfully separated chromatographically, obtaining **4c** as a pale yellow solid at yields of 43–52 %. Compared to that of **4b**, the ^{1}H NMR spectrum showed only homotopic protons (Figure 6.18). The new alkene functionality appeared as a characteristic broad signal at 6.52 ppm, and the isomer identity was confirmed by NOESY correlations between this signal and the other aliphatic resonances. (Figure E8) The slower eluating *exo*–isomer **5c** was usually obtained only in mixed fractions due to narrow band separation, although it was obtained once at a yield of 29 % following a particularly large column. Its alkene hydrogen appeared at 6.49 ppm, and produced NOESY correlations only with the aromatic ring as previously mentioned. (**??**)

Neither of the ethyl esters **4c** or **5c** have previously been described, although analogues with different substituents have been reported. [90, 95] The optimised procedure turned out to compare favourably with methods in literature, with near identical yields to other enolate approaches and almost double the yield of Horner–Wadsworth–Emmons reactions. [88–90, 96] The Reformatsky reaction comes out superior with reported yields of 65–95 %, supposedly forming the indene–isomer selectively. [87, 97]

3.4.3 Transformation to hydroxamic acid

The transformaton of ethyl ester **4c** into its corresponding hydroxamic acid **6a** proved to be reletively simple compared to the aforementioned struggles of Routes II and III. Firsty, it being an ethyl ester already made it far more susceptible to nucleophilic attack at the ester carbonyl, more in line with what had originally been reported by Boularot *et al.* [49] Moreover, its lack of a hydrogen–bonding heteroatoms in the central scaffold could only attribute to a worse water solubility than the indole benchmark, making issues with the work–up procedure unlikely. As such, the transformation commenced with standard hydroxylaminolysis conditions (Scheme 3.22).

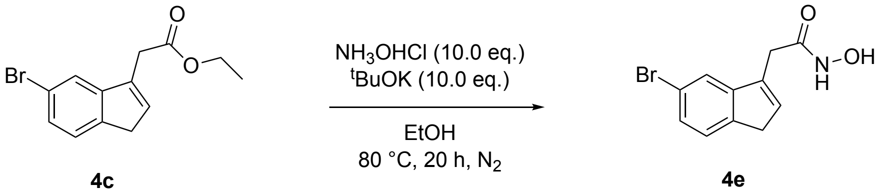

Scheme 3.22: Hydroxylaminolysis of indenyl ethyl ester **4c** forming indenyl hydroxamic acid **4e**, the target structure of Route IV. Adapted from ref 49.

The reaction proceeded as designed, producing target molecule **4e** as a white solid at a yield of 45 %. The formation of the hydroxamic acid group was clearly visible in the ^{1}H NMR spectrum by the emergence of two broad singlets at 10.66 ppm and 8.86 ppm (Figure 6.20). The compound had never previously been reported. The obtained yield fell within the typical yield range of 45–83 % reported by Boularot *et al.* [49]. Moreover, the apparent lack of ethyl acetate in the final product meant that the high solvent affinity described in Route I was largely dependant on the indole nitrogen, perhaps in a coordinated manner with the hydroxamic acid group.

Interestingly, the conditions of the hydroxylaminolysis appeared to heavily favour the *endo*–isomer **4e**, seeing as no *exo*–isomer could be observed i the resulting ^{1}H NMR spectrum. In fact, varrying out the reaction with the *exo*–isomer **5c** gave the *endo* hydroxamic acid **4e** exclusively. The reason for this behaviour remains unknown.

Preliminary tests were conducted on the basic hydrolysis of **4c** to form the carboxylic acid **4d**, but poor yields made the method undesirable. The subsequent peptide coupling was also shown to induce *endo*/*exo*–scrambling, with both the *endo*–acid **4e** and *exo*–acid **5e** yielding isomeric mixtures. Of the two, the latter isomerised more.

3.5 Hydrazide synthesis

The secondary goal of this thesis was to explore other potential metal–binding functional groups, specifically those with the same number of heteroatoms as the hydroxamic acids moiety. A natural first choice was therefore the hydrazide group, which in principle could be prepared by simply exchanging hydroxylamine with hydrazine in the already discussed procedures. So far, only the indole and indene scaffolds have been shown to form the hydroxamic acid as intended, making them prime candidates for testing hydrazide formation.

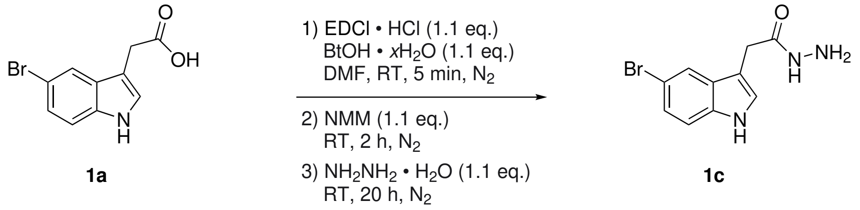

Scheme 3.23: Peptide coupling of indolyl carboxylic acid **1a** with hydrazine forming indolyl hydrazide **1c**, the alternative target of Route I

Synthesising the indole hydrazide **1c** involved a peptide coupling between carboxylic acid **1a** and hydrazine, directly equivalent to the reaction in Route I (Scheme 3.23). Conducting the reaction in this manner produced a crude material that could be identified as target molecule **1c** by ^{1}H NMR and high–resolution mass spectrometry (HRMS)[1]. The hydrazide functional group was visible as a broadened singlet at 9.15 ppm and a broad hump at 4.19 ppm. However, the compound has yet to be purified sufficiently, mainly becuase the hydrazide reacts with acetone making it unsuitable for recrystallisation.

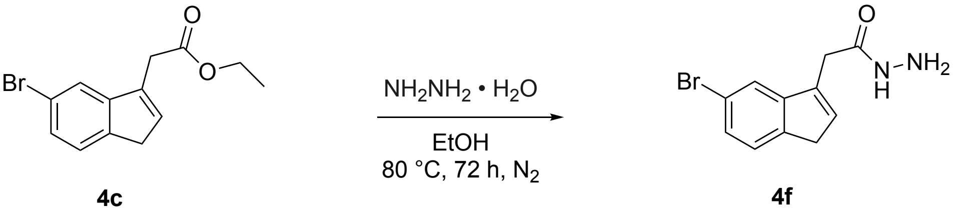

Scheme 3.24: Hydrazinolysis of indenyl ethyl ester **4c** yielding indenyl hydrazide **4f**, the alternative target of Route IV

Synthesising the indene hydrazide **4f** meant performing a hydrazinolysis reaction with the ethyl ester **4c** (Scheme 3.24). Suitable conditions were found by simply treating the ester with hydrazine and stirring at high heat, with full conversion occurring sometime between 24 and 72 hours after reaction start. The formation of the molecule was verified by the crude material ^{1}H NMR spectrum (Figure A6), although further purification is needed.

This noticeably longer reaction time compared to the hydroxylaminolysis was somewhat surprising , given the stronger nucleophilicity of hydrazine. [78] However, since hydroxylamine is added as a hydrochloride salt, it is possible that small inaccuracies in stoichiometry may yield slightly acidic conditions that accelerate the reaction.

3.6 Considerations for future biochemical testing

In a parallel study, I. K. Faye–Schjøll of the Hersleth group successfully managed to express catalytically active PDF from *S. aureus*, *N. gonorrhoeae*, and human mitochondria. [98]

---

[1] **HRMS** (ESI, CH_3CN): m/z $[C_{10}H_{10}BrN_3O + Na]^+$: calcd.: 289.9899 / 291.9878, found: 289.9899 / 291.9879

This means that the synthesised target molecules **1b** and **4e** can be tested for inhibitory activity in the near future.

While still only preliminary, a potential difference in potencies between these molecules would give valuable information on what the role of the indole fragment is. The indole target being more potent could imply that the nitrogen is involved in an important hydrogen bond, or that a favourable aromatic π–stacking interaction takes place. Conversely, the indene target being more potent would suggest that scaffold size is the only factor of interest, thus allowing for a larger variety in future target design.

The presence of organic solvent in the solid form of **1b** should be kept in mind when conducting biochemical testing in the future, both in terms of stoichiometry and in terms of potential interference with the inhibitory activity. Control tests using only the organic solvent at appropriate concentrations should be conducted. The original article by Boularot *et al.* made no mention of solvent cocrystallisation occuring, implying that pure compound is achievable.

4

Conclusion

In this study we attempted to synthesise analogues of the selective PDF inhibitior AB47 with key structural elements altered. Four synthetic routes were designed; Route I to the indole benchmark, Route II to a benzimidazole structure, Route III to a triazole structure, and Route IV to an indene structure. Only Routes I and IV were completed.

The indole benchmark molecule AB47 (**1b**) was successfully synthesised at a yield of 29 %. Its spectroscopic data were in accordance with literature, although it cocrystallised with considerable amount of solvent.

The indene target molecule **4e** was successfully synthesised at an overall yield of 22 % over three steps. During the second step, an *endo*/*exo*–isomer mixture had to be separated. The isomerisation equilibrium favoured the *endo* ethyl ester **4c** by a small margin. Only the *endo*–isomer **6a** was formed in the final step.

Much progess was made on the synthesis of benzimidazole and benzotriazole analogues of AB47. Both scaffolds were successfully synthesised at good yelds. Formation of a crucial *ortho*–diamine intermediate required careful optimisation, as it was able to cyclise intramolecularly under acidic conditions. The routes failed at incorporating the crucial hydroxamic acid moiety.

Preliminary studies were made on the synthesis of indole and indene hydrazides, although further purification is needed.

5

Further work

This thesis leaves behind a series of potential leads that should be resolved in future work. This includes biochemical testing, completion of synthetic routes, and design of additional target molecules.

First and foremost, the indole (**1b**) and indene (**4e**) targets that were synthesised in this work should be tested for inhibitory activity against bacterial and human PDF. Differences in potency between these molecules might answer whether or not the indole fragment is more than just a scaffold of appropriate size.

Secondly, incorporation of the crucial hydroxamic acid group to the benzimidazole (**2d**) and benzotriazole (**3d**) intermediates should be investigated further. The apparent water–solubility of target structures **2f** and **3f** complicates the work–up procedure, and future attempts should make use of reagents whose byproducts can be filtered off directly or extracted into organic solvents. Suggested reagents include *N*,*N'*–dicyclohexylcarbodiimide (DCC) and hydroxylamine Wang resin. [79, 80]

Thirdly, the preliminary attempts at altering the metal chelator should be continued by establishing a work–up procedure for the hydrazide targets **1c** and **4f**. Hydrazinolysis of the benzimidazole (**2d**) and benzotriazole (**3d**) intermediates should be attempted.

Moreover, synthetic routes to four additional target structures have been designed. A saturated indane analogue is proposed to explore the steric effects of letting the β–position relative to carbonyl be sp^3–hybridised (Scheme 5.1). The potential two–step synthesis involves hydrogenation of either indene **4c** or indanylidene **5c**.

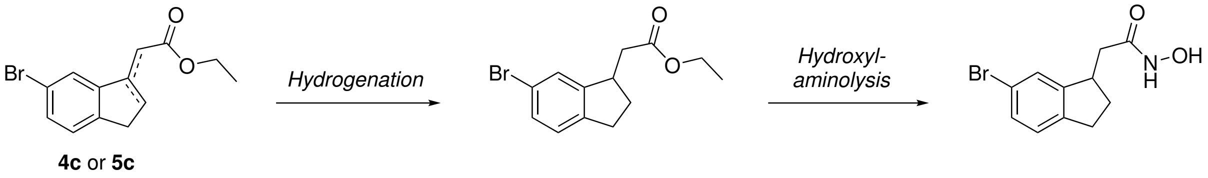

Scheme 5.1: Suggested synthetic route for an indane–based hydroxamic acid target, starting from either **4c** or **5c**.

To explore steric effect in the ring–plane, suggested routes to the equivalent naphthalene and quinoline scaffolds are presented (Scheme 5.2). Synthesising the former could potentially go *via* a similar route to that of Route IV of this thesis, with the necessary aromatisation step being inspired by Singh and Seitz. [99] Synthesis of the latter could go through an S_NAr reaction between a bromochloroquinoline and a malonate diester, equivalent to what has been discribed with methylmalonate diesters previously. [100]

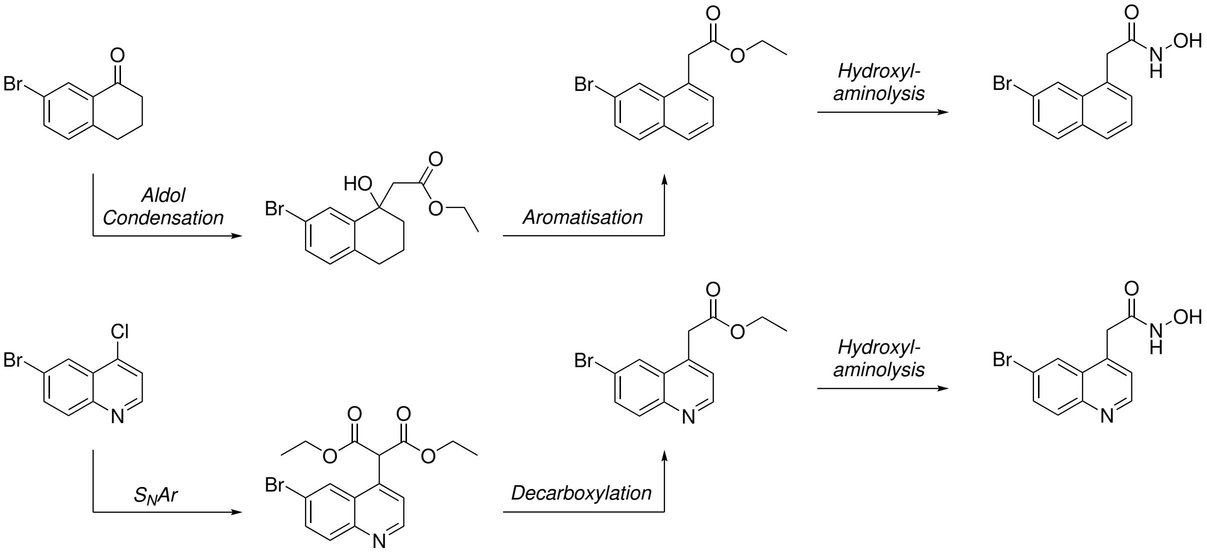

Scheme 5.2: Suggested synthetic routes for a naphthalene–based and a pyridine–based hydroxamic acid target, starting from commercially available 7–bromotetral–1–one and 6–bromo–4–chloroquinoline, respectively.

To explore the influence of sulfur on the metal–binding interaction, a potential thiohydroxamic acid chelator was envisioned (Scheme 5.3). The indole–based target without bromine has previously been described, going through a transformation of the corresponding primary nitro compound using potassium hydride and bis(trimethylsilyl)sulfide. [101] The needed nitro compound can be synthesised as described by Ranganathan *et al.* [102]

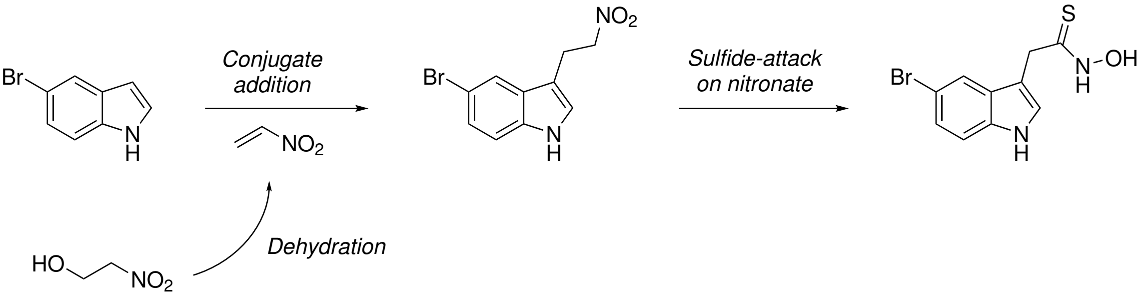

Scheme 5.3: Suggested synthetic route for an indole–based thiohydroxamic acid target, starting from commercially available 5–bromoindole and 2–nitorethanol.

Lastly, as a long–term goal, future research should try to incorporate a hydrogen–accepting structural motif on a side chain branching off the central scaffold. This would potentially make use of the additional hydrogen–bond interaction that Meinnel and affiliates highlighted with the oxadiazole series. [52] Suggested motifs include oxadiazole and hydantoin.

6

Experimental

6.1 General

All solvents and chemicals were purchased fom Fluorochem, Sigma–Aldrich, Tokyo Chemical Industry and VWR and were used as recieved. Deuterated solvents were purchased from Cambridge Isotope Laboratories, Eurisotop and Sigma–Aldrich. Tetrahydrofuran (THF)*N*,*N*–Dimethylformamide (DMF), and CH_2Cl_2 were purified using an MB SPS–800 solvent purifier system from MBraun. All water and ice used were of Type II. Hexanes and ethyl acetate were distilled before use.

All reactions were performed in air unless otherwise stated. All glassware used under inert conditions was pre–heated in an oven at 120 °C for several hours. Sonication was applied using a 5 L PALSSONIC Profi ultrasonic cleaner from ALLPAX. Thin–layer chromatography (TLC) was performed using Merck 60 F_{254}–plates. Column chromatography was performed using silica gel from VWR (60, 0.040–0.063 mm).

NMR spectra were recorded using Bruker Avance DPX300, AVIII400HD, AVI600, AVII600 and AVIII800HD instruments at ambient temperatures. Chemical shifts (δ) are given in parts per million (ppm) and have been referenced relative to the residual solvent signals of DMSO–d_6 (δ_H 2.50 ppm, δ_C 39.5 ppm) as reported by Fulmer *et al.* [103] ^{15}N chemical shifts were obtained indirectly through ^1H–^{15}N HMBC experiments and are referenced relative to liquid NH_3 using CH_3CN (δ_N 245.3 ppm) or CH_3NO_2 (δ_N 380.5 ppm) as internal standards (1.0 µL). [67] Coupling constants (J) are given in hertz (Hz). Basic resonance multiplicities are abbreviated as follows: s – singlet, d – doublet, t – triplet, q – quartet, m – multiplet, br – broad, with combinations being used when applicable (e.g. td being a triplet of doublets). Resonances that display second order effects are labeled using the appropriate Pople nomenclature followed by a basic multiplicity (e.g. ABq being a quartet from an AB system). [93] All ^{13}C NMR spectra were ^1H decoupled unless stated otherwise.

All ^{1}H and ^{13}C NMR resonances were assigned using two–dimensional NMR techniques including HSQC and HMBC. COSY was used whenever ^{1}H NMR coupling patterns were ambiguous. NOESY was used in cases of chirality and isomerism. ^{15}N NMR resonances were assigned using ^{1}H–^{15}N HMBC. Note that the assigned atoms are numbered after IUPAC naming conventions, and thus the numbering pattern may appear to switch between compounds.

Mass spectra (ESI) were obtained on a Bruker maXis II ETD QTOF spectrometer by Osamu Sekiguchi and Lina Aarsborg (University of Oslo). The molecular fragments were quoted using mass–to–charge ratios (m/z). Fragments containing bromine are reported with two mass–to–charge ratios in the format ^{79}Br / ^{81}Br.

Fourier–transform IR spectra were recorded in ATR (Bruker ATR A225/Q) on a Vertex 80 Bruker infrared spectrophotometer, equipped with a DTGS detector. Vibrational modes are quoted using wavenumbers ($\widetilde{\nu}$) measured in reciprocal centimetres (cm^{-1}) and are assigned using standard IR spectrum tables. [66, 104]

Melting point were measured on a Stuart SMP10 melting point apparatus and are reported uncorrected.

6.2 Synthesis of compounds in Route I

2–(5–Bromoindol–3–yl)acetohydroxamic acid (1b)

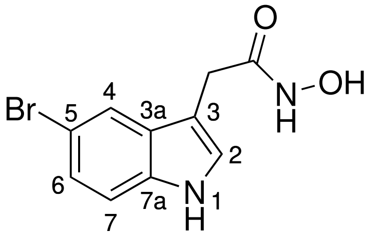

The compound was prepared as reported by Boularot *et al.* [49]
A solution of 2–(5–bromoindol–3–yl)acetic acid (203 mg, 0.798 mmol, 1.00 eq.), 1–ethyl–3–(3–dimethylammoniopropyl)carbodiimide chloride (169 mg, 0.880 mmol, 1.10 eq.) and 1–hydroxybenzotriazole hydrate (125 mg, 0.909 mmol, 1.14 eq.) in dry DMF (2.80 mL) was stirred under nitrogen at room temperature for 5 min. The solution was added *N*–methylmorpholine (100 µL, 0.910 mmol, 1.14 eq.) and stirred for another 2 h under nitrogen. The solution was then treated with hydroxylammonium chloride (61.3 mg, 0.882 mmol, 1.11 eq.) and stirred at room temperature overnight. The DMF was evaporated under reduced pressure and the residual oil was dissolved in ethyl acetate (40 mL). The resulting solution was washed with water (3 × 25 mL), saturated $NaHCO_3$ (25 mL), water again and brine (both 25 mL) before being dried over $MgSO_4$, filtered by gravity and evaporated under reduced pressure. The crude product was twice recrystallised from 1:1 acetone/cyclohexane *via* slow evaporation of acetone under reduced pressure. Washing with cyclohexane and evaporation to dryness yielded **1b** as a white solid.
Yield: 63.8 mg (29 %)

^{1}H NMR (600 MHz, DMSO–d_6): δ (ppm) **11.09** (br s, 1 H, H1), **10.62** (s, 1 H, N**H**OH), **8.78** (s, 1 H, NHO**H**), **7.78** (d, 1 H, J = 1.6 Hz, H4), **7.31** (d, 1 H, J = 8.6 Hz, H7), **7.24** (d, 1 H, J = 2.1 Hz, H2), **7.17** (dd, 1 H, J = 8.6, 1.9 Hz, H6), **3.37** (s, 2 H, CH_2)

^{13}C NMR (151 MHz, DMSO–d_6): δ (ppm) **167.4** (C=O), **134.7** (C7a), **129.0** (C3a), **125.5** (C2), **123.3** (C6), **121.1** (C4), **113.3** (C7), **111.0** (C5), **108.4** (C3), **29.5** (CH_2)

IR (ATR): $\widetilde{\nu}$ (cm^{-1}) **3348** (O–H), **3202** (N–H), **3020** (N–H), **1628** (C=O), **1448** (C–H)

^{15}N{^{1}H} NMR (600 MHz, DMSO–d_6): δ (ppm) **164.5** (NHOH), **131.7** (N1)

HRMS (ESI, CH_3CN): m/z $[C_{10}H_9BrN_2O_2 + Na]^+$:
calcd.: **290.9740 / 292.9720**, found: **290.9739 / 292.9719**

mp: 137–140 °C

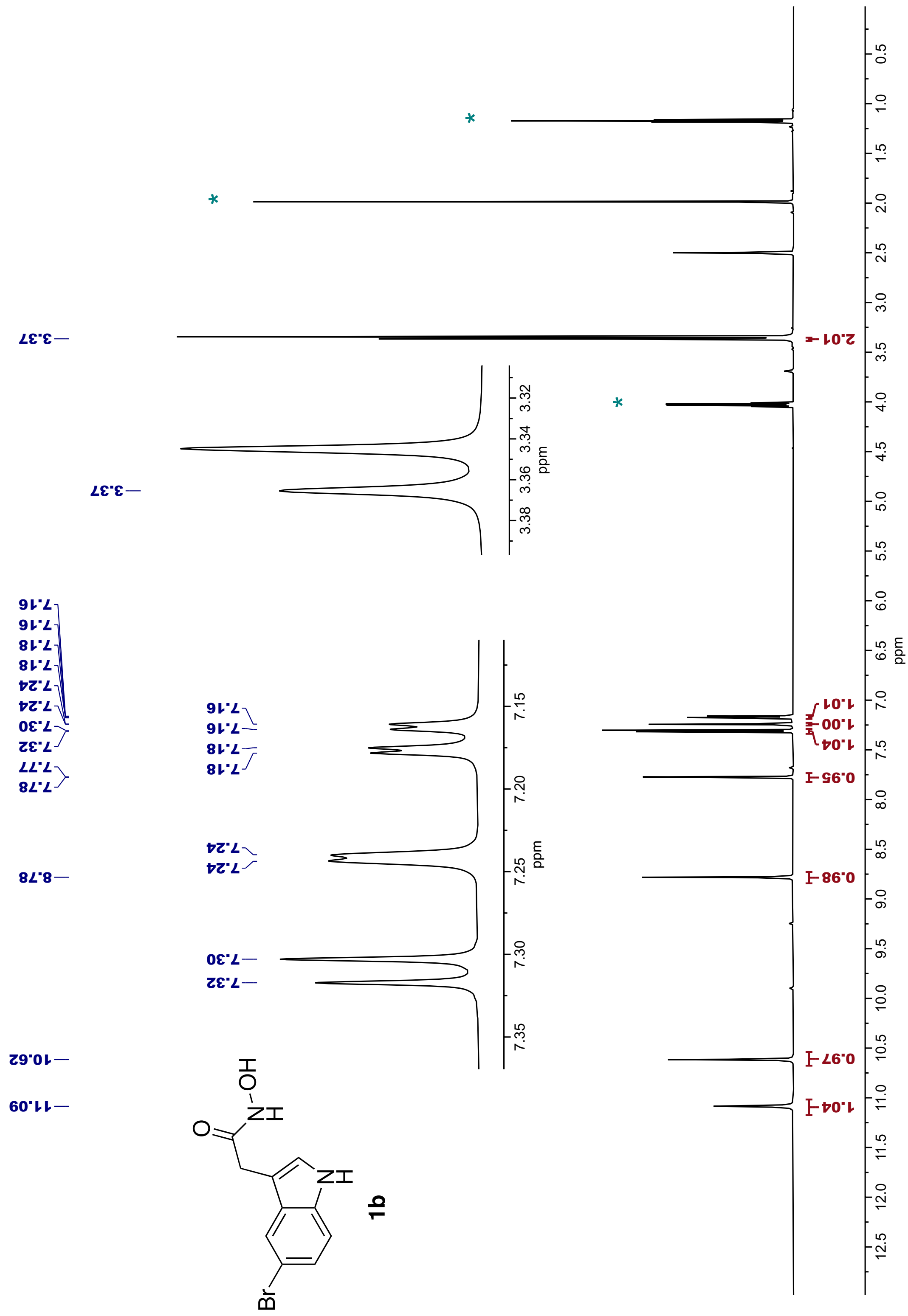

Figure 6.1: ^{1}H NMR (600 MHz, DMSO–d_6) spectrum of **1b**.
Signals from ethyl acetate are marked with teal asterisks.

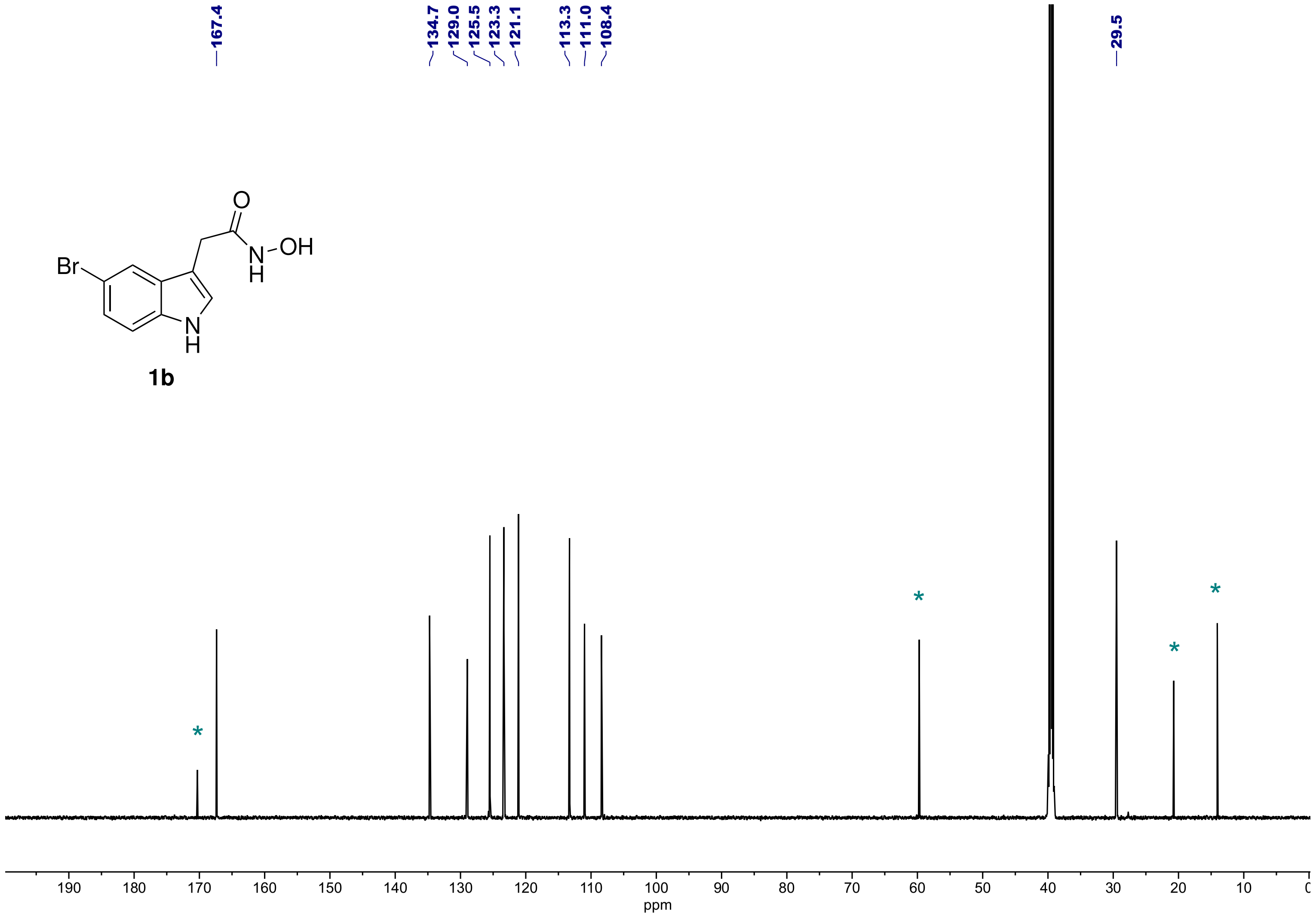

Figure 6.2: ^{13}C NMR (151 MHz, DMSO–d_6) spectrum of **1b**.
Signals from ethyl acetate are marked with teal asterisks.

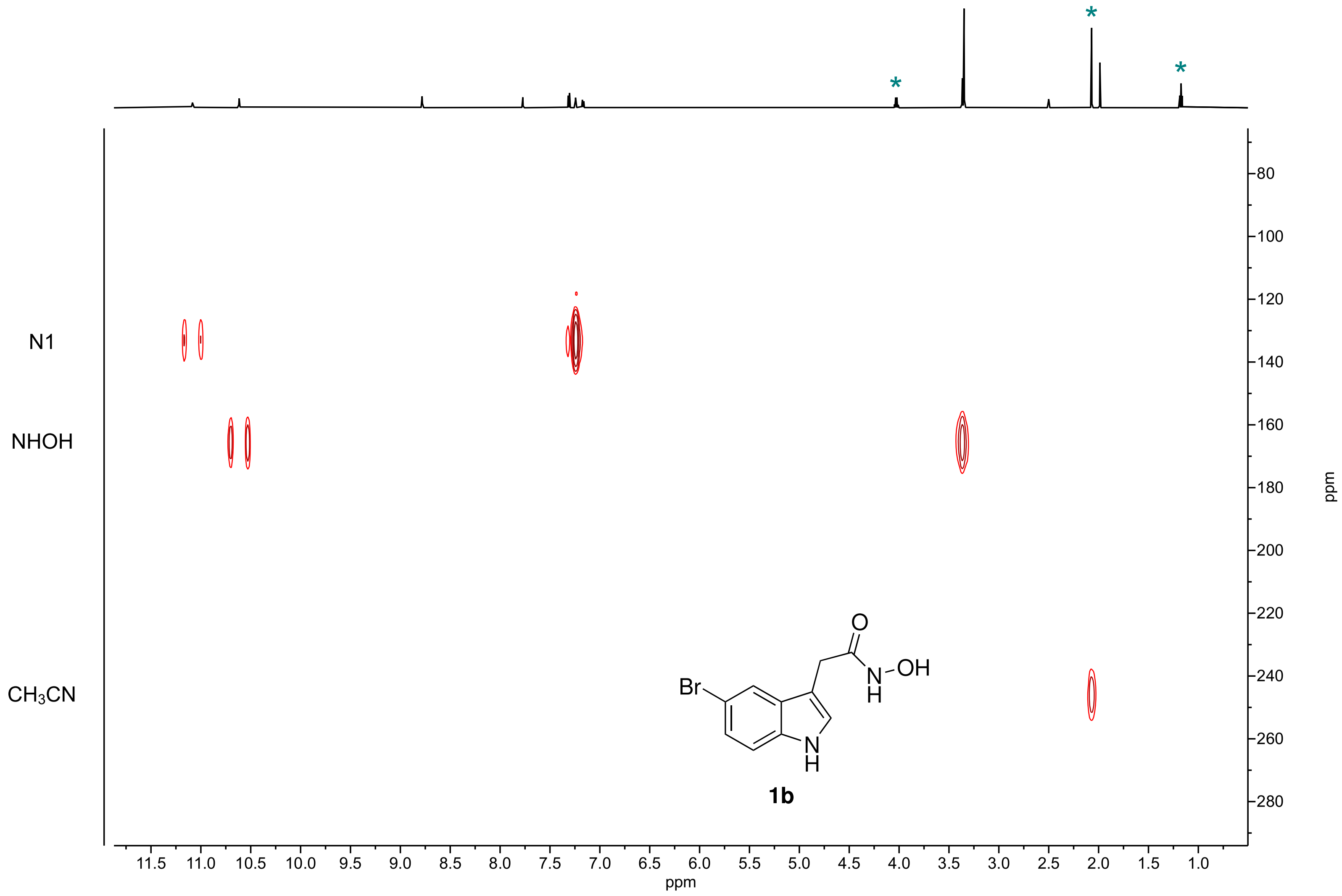

Figure 6.3: ^{1}H–^{15}N HMBC (600 MHz, DMSO–d_6) spectrum of **1b** with CH_3CN as an internal standard. Signals from ethyl acetate are marked with teal asterisks.

6.3 Synthesis of compounds in Route II

tert–Butyl (5–bromo–2–nitrophenyl)glycinate (2b)

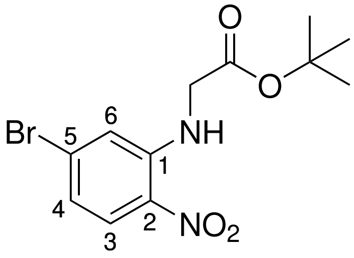

The compound was prepared based on a reported procedure by Brooks *et al.* [60]
A solution of 4–bromo–2–fluoro–1–nitrobenzene (1.25 g, 5.69 mmol, 1.00 eq.), *tert*–butyl glycinatium chloride (1.00 g, 5.99 mmol, 1.05 eq.), and K_2CO_3 (1.85 g, 13.4 mmol, 2.36 eq.) in acetonitrile (60 mL) and dichloromethane (6.7 mL) was left to stir at room temperature for 4 days. The solvents were evaporated under reduced pressure and the resulting crude solid was redissolved in dichloromethane and filtered by gravity. The filtrate was concentrated under reduced pressure and purified by column chromatography (silica gel, toluene) yielding **2b** as a bright yellow solid.
Yield: 1.48 g (79 %)

^{1}H NMR (600 MHz, DMSO–d$_6$): δ (ppm) **8.39** (t, 1 H, J = 5.4 Hz, NH), **8.01** (d, 1 H, J = 9.1 Hz, H3), **7.12** (d, 1 H, J = 1.9 Hz, H6), **6.89** (dd, 1 H, J = 9.1, 1.9 Hz, H4), **4.19** (d, 2 H, J = 5.6 Hz, CH$_2$), **1.44** (s, 9 H, C(CH$_3$)$_3$)

^{13}C NMR (151 MHz, DMSO–d$_6$): δ (ppm) **168.6** (C=O), **144.9** (C1), **130.8** (C2), **130.6** (C5), **127.9** (C3), **118.8** (C4), **117.3** (C6), **81.7** (**C**(CH$_3$)$_3$), **44.9** (CH$_2$), **27.7** (C(**C**H$_3$)$_3$)

^{15}N{^{1}H} NMR (600 MHz, DMSO–d$_6$): δ (ppm) **370.6** (NO$_2$), **75.6** (NH)

IR (ATR): $\widetilde{\nu}$ (cm^{-1}) **3358** (N−H), **2980** (C−H), **1736** (C=O), **1616** (N−H), **1555** ($\mathrm{N}\overset{\scriptscriptstyle --}{-}\mathrm{O}$), **1493** (C−H), **1306** ($\mathrm{N}\overset{\scriptscriptstyle --}{-}\mathrm{O}$), **1242** (C−O), **1153** (C−O)

HRMS (ESI, CH$_3$CN): m/z $[C_{12}H_{15}BrN_2O_4 + Na]^+$:
calcd.: **353.0107** / **355.0086**, found: **353.0107** / **355.0087**

R$_f$ (Toluene): 0.26

mp: 95–96 °C

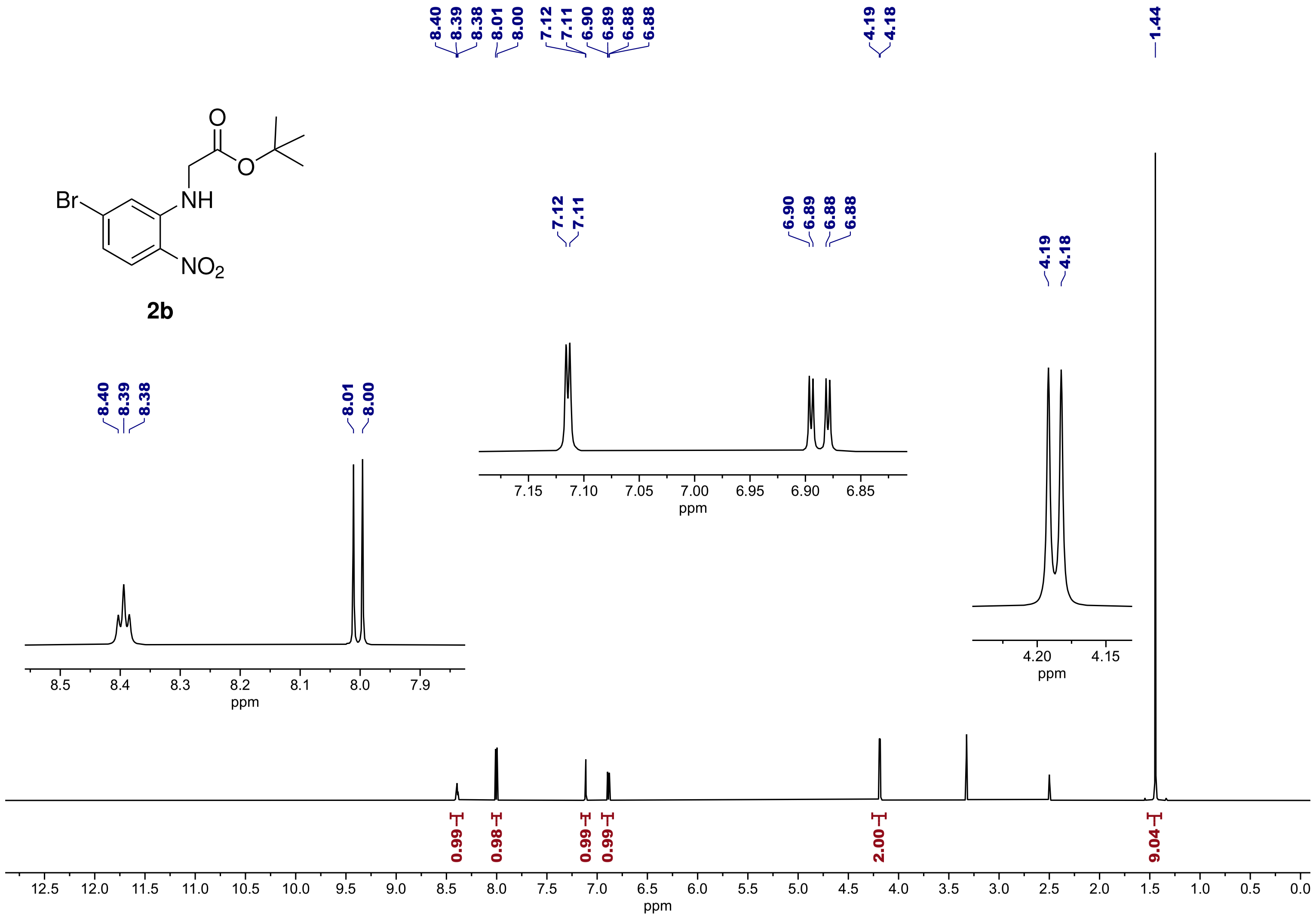

Figure 6.4: ^{1}H NMR (600 MHz, DMSO–d$_6$) spectrum of **2b**.

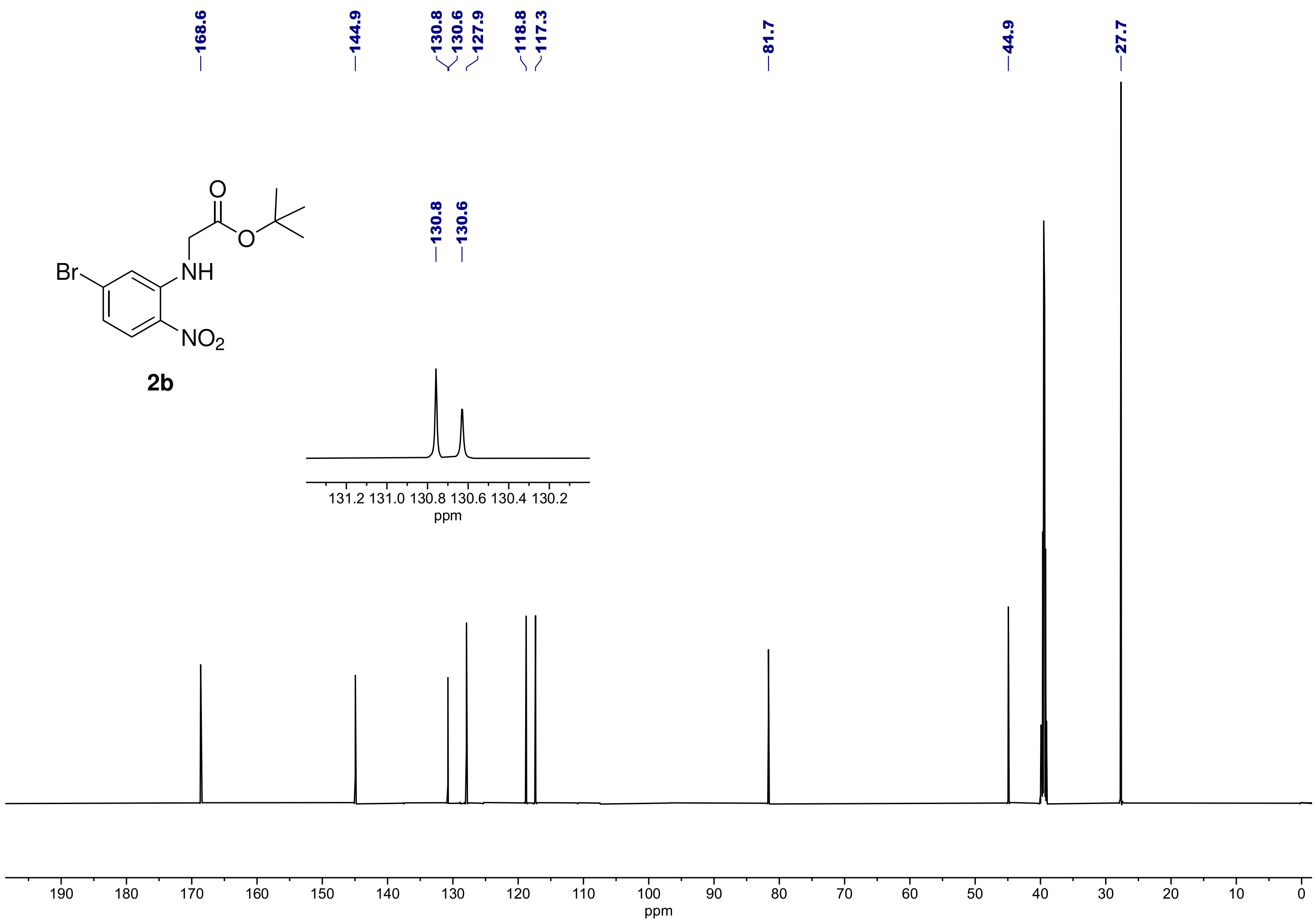

Figure 6.5: ^{13}C NMR (151 MHz, DMSO–d$_6$) spectrum of **1b**.

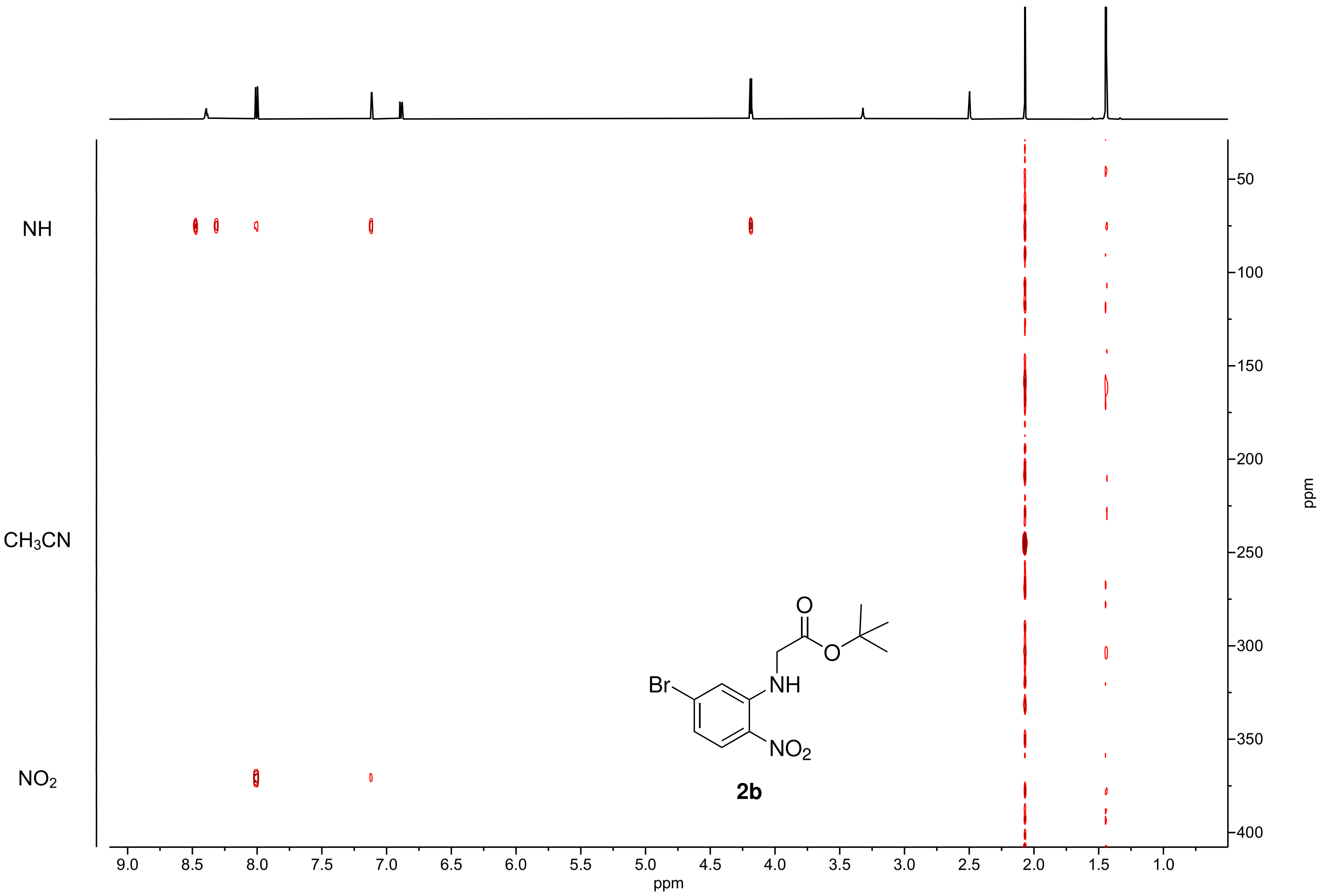

Figure 6.6: ^{1}H–^{15}N HMBC (600 MHz, DMSO–d$_6$) spectrum of **1b** with CH_3CN as an internal standard.

tert–Butyl (2–amino–5–bromophenyl)glycinate (2c)

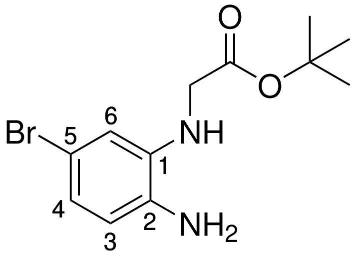

The compound was prepared based on a reported procedure by Kallinen *et al.* [72]
A suspension of *tert*–butyl (5–bromo–2–nitrophenyl)glycinate (**2b**) (265 mg, 0.799 mmol, 1.00 eq.) and iron powder (449 mg, 8.04 mmol, 10.1 eq.) in ethanol (4.2 mL) and aqueous NH_4Cl (1.05 mL, 8.01 mmol, 10.0 eq.) was stirred in darkness at 60 °C for 3 h. The resulting suspension was neutralised with saturated $NaHCO_3$ (30 mL), diluted with ethyl acetate (30 mL) and filtered through silica using ethyl acetate as eluent (200 mL). The two phases were separated, and the organic phase was washed with brine and dried over $MgSO_4$ before being filtered by gravity and concentrated under reduced pressure. The resulting crude oil was purified by column chromatography (silica gel, 6:4 Hexane/EtOAc) yielding **2c** as a pale brown solid.
Yield: 134 mg (56 %)

^{1}H NMR (600 MHz, DMSO–d_6): δ (ppm) **6.56** (dd, 1 H, J = 8.2, 2.1 Hz, H4), **6.49** (d, 1 H, J = 8.2 Hz, H3), **6.32** (d, 1 H, J = 2.1 Hz, H6), **5.22** (t, 1 H, J = 6.3 Hz, NH), **4.69** (s, 2 H, NH_2), **3.79** (d, 2 H, J = 6.3 Hz, CH_2), **1.42** (s, 9 H, $C(CH_3)_3$)

^{13}C NMR (151 MHz, DMSO–d_6): δ (ppm) **170.3** (C=O), **136.9** (C1), **134.7** (C2), **119.3** (C4), **115.3** (C3), **112.1** (C6), **108.4** (C5), **80.7** ($\mathbf{C}(CH_3)_3$), **45.7** (CH_2), **27.7** ($C(\mathbf{C}H_3)_3$)

^{15}N{^{1}H} NMR (600 MHz, DMSO–d_6): δ (ppm) **53.6** (NH), **51.0** (NH_2)

IR (ATR): $\widetilde{\nu}$ (cm^{-1}) **3397** (N–H), **3315** (N–H), **2978** (C–H), **1728** (C=O), **1508** (C–H), **1362** (C–N), **1232** (C–O), **1161** (C–O)

HRMS (ESI, CH_3CN): m/z $[C_{12}H_{17}BrN_2O_2 + Na]^+$:
calcd.: **323.0366 / 325.0346**, found: **323.0365 / 325.0345**

R_f (6:4 Hexane/EtOAc): 0.26

mp: 67–70 °C

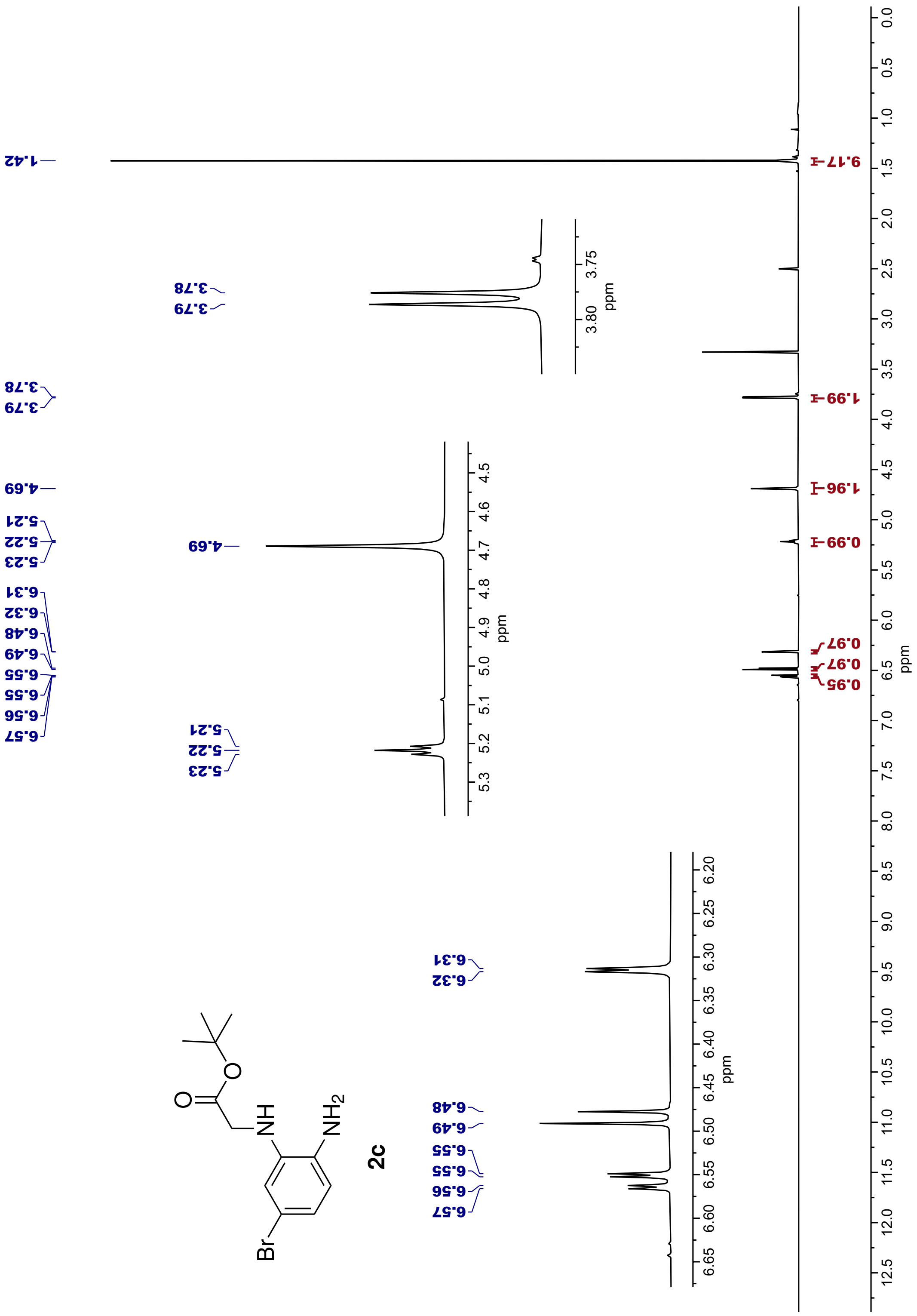

Figure 6.7: ^{1}H NMR (600 MHz, DMSO–d$_6$) spectrum of **2c**.

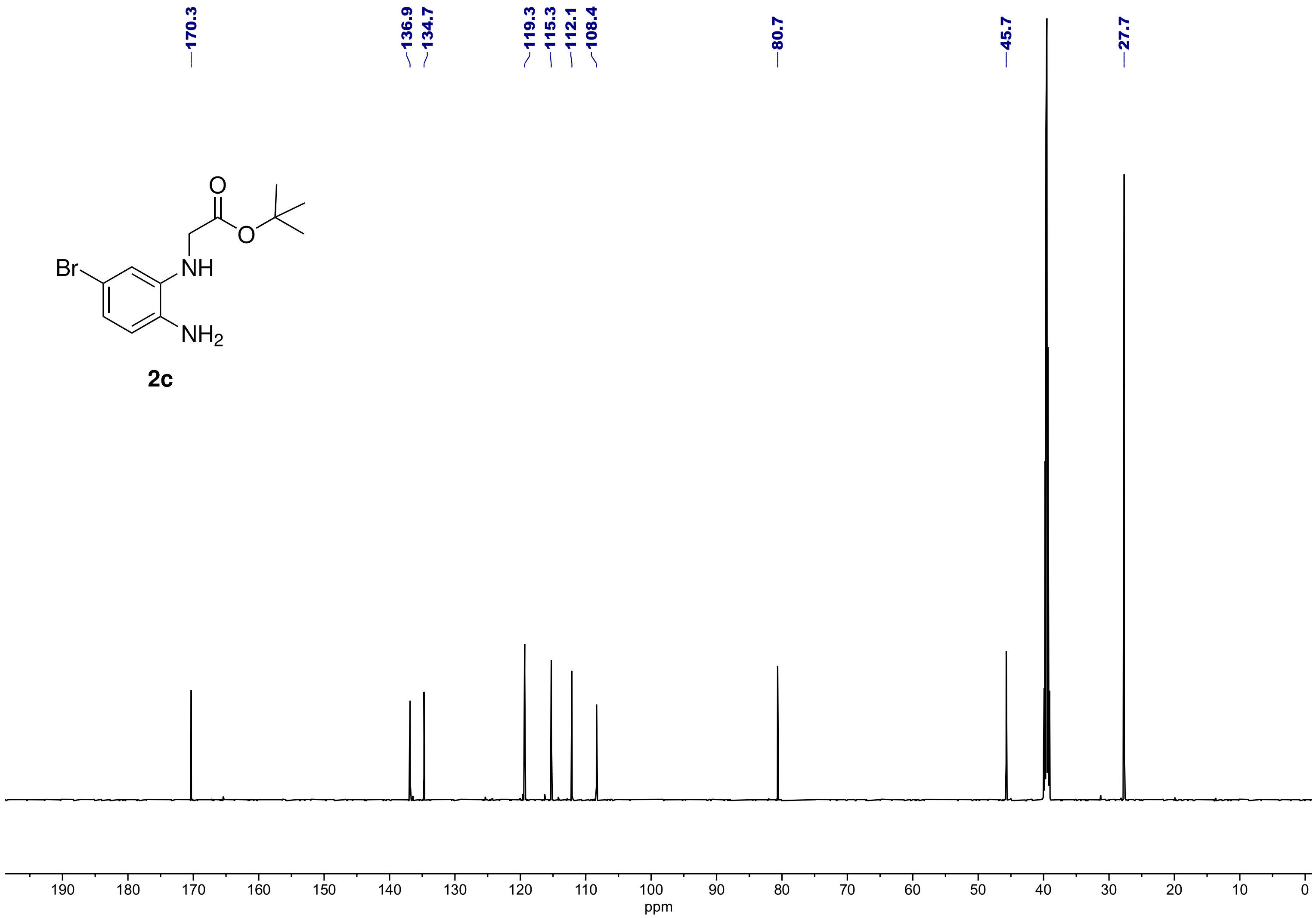

Figure 6.8: ^{13}C NMR (151 MHz, DMSO–d$_6$) spectrum of **2c**.

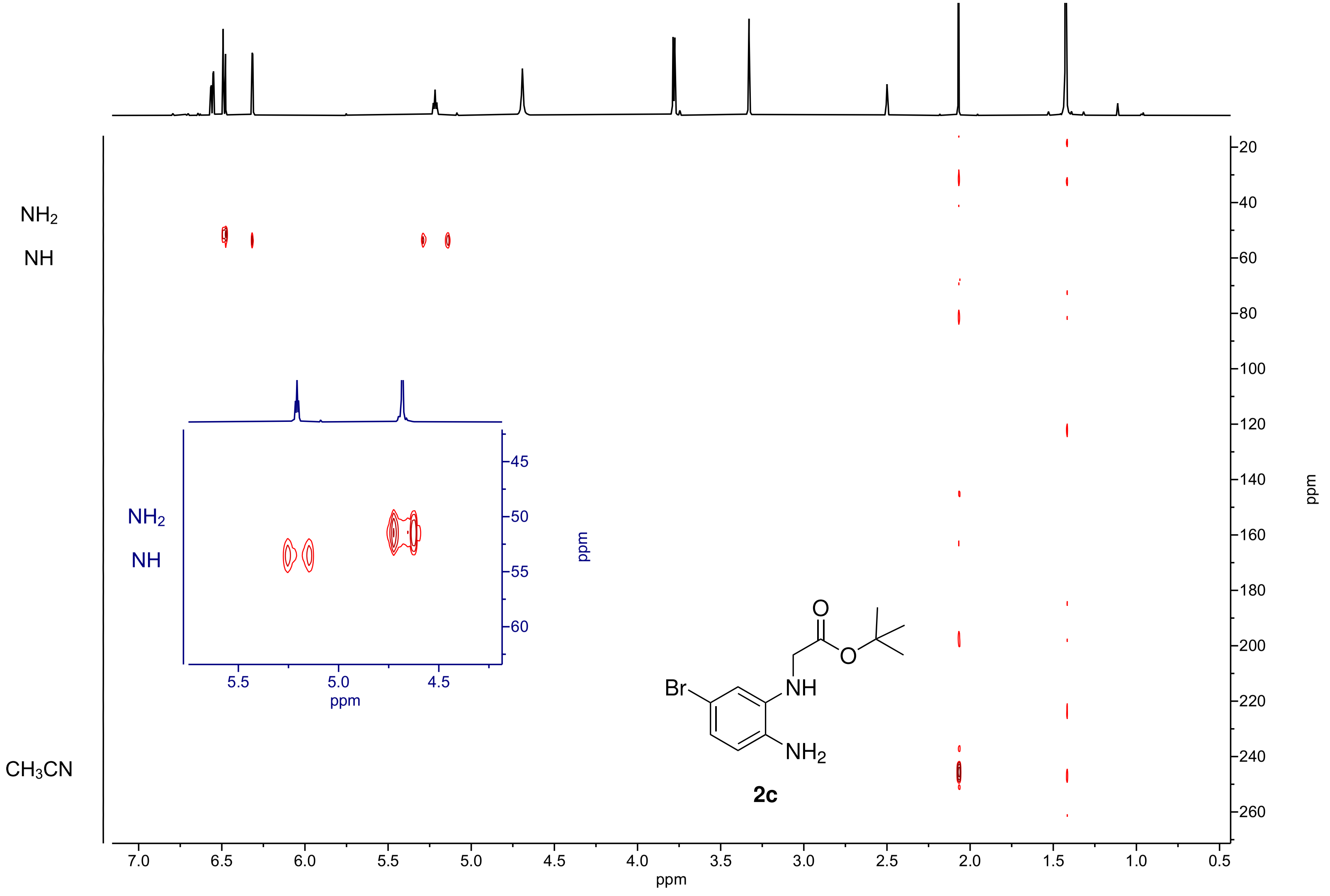

Figure 6.9: ^{1}H–^{15}N HMBC (600 MHz, DMSO–d$_6$) spectrum of **2c** with CH$_3$CN as an internal standard. Inset of ^{1}H–^{15}N HMBC spectrum recorded at 800 MHz, showing a $^1J_{\mathrm{HN}}$ correlation from the NH$_2$ signal at 4.69 ppm.

tert–Butyl 2–(6–bromobenzimidazol–1–yl)acetate (2d)

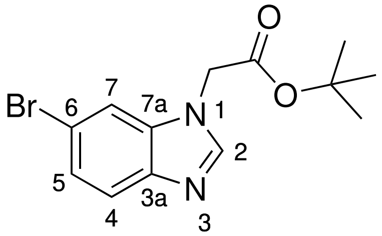

The compound was prepared based on two reported procedures. [60, 74]
tert–Butyl (2–amino–5–bromophenyl)glycinate (**2c**) (60.1 mg, 0.200 mmol, 1.00 eq.) and *p*–toluenesulfonic acid monohydrate (4.6 mg, 0.024 mmol, 0.12 eq.) were dissolved in triethyl orthoformate (1.65 mL) and left to stir at 60 °C for 2.5 h. The resulting suspension was treated with THF (1.8 mL) and aqueous HCl (pH = 3, 0.5 mL), and was left to stir at room temperature for 20 min. The organic solvents were evaporated under reduced pressure, and the residual aqueous phase was diluted with saturated $NaHCO_3$ and extracted with ethyl acetate. The organic phase was washed with water and brine before being dried over $MgSO_4$ and filtered by gravity. Evaporation under reduced pressure gave **2d** as a beige solid. The compound was used in the next reaction without further purification.
Yield: 53.1 mg (87 %)

^{1}H NMR (600 MHz, DMSO–d_6): δ (ppm) **8.21** (s, 1 H, H2), **7.85** (d, 1 H, J = 1.7 Hz, H7), **7.62** (d, 1 H, J = 8.6 Hz, H4), **7.35** (dd, 1 H, J = 8.5, 1.9 Hz, H5), **5.14** (s, 2 H, CH_2), **1.43** (s, 9 H, $C(CH_3)_3$)

^{13}C NMR (151 MHz, DMSO–d_6): δ (ppm) **167.2** (C=O), **145.7** (C2), **142.1** (C3a), **135.5** (C7a), **124.6** (C5), **121.0** (C4), **114.9** (C6), **113.6** (C7), **82.0** (**C**$(CH_3)_3$), **46.0** (CH_2), **27.6** (C(**C**$H_3)_3$)

^{15}N{^{1}H} NMR (600 MHz, DMSO–d_6): δ (ppm) **243.2** (N3), **146.0** (N1)

IR (ATR): $\tilde{\nu}$ (cm^{-1}) **2964** (C–H), **1742** (C=O), **1495** (C–H), **1366** (C–N), **1232** (C–O), **1148** (C–O), **810** (Benzimidazole ring[I])

HRMS (ESI, CH_3CN): m/z $[C_{13}H_{15}BrN_2O_2 + H]^+$:
calcd.: **311.0390 / 313.0370**, found: **311.0390 / 313.0370**

mp: 145–147 °C

[I] Observed in region typical of ring–bending modes. [105–107]

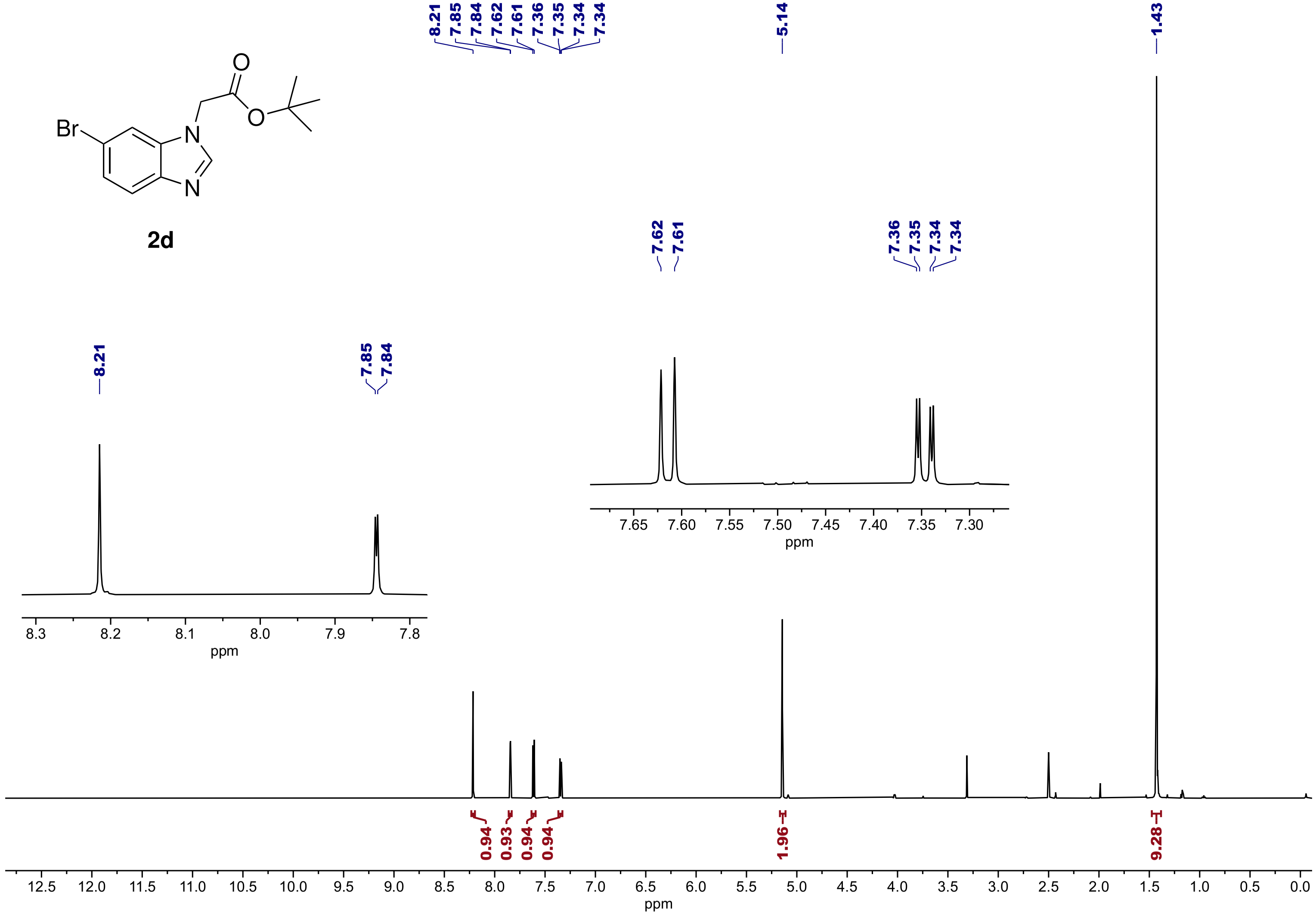

Figure 6.10: ^{1}H NMR (600 MHz, DMSO–d$_6$) spectrum of **2d**.

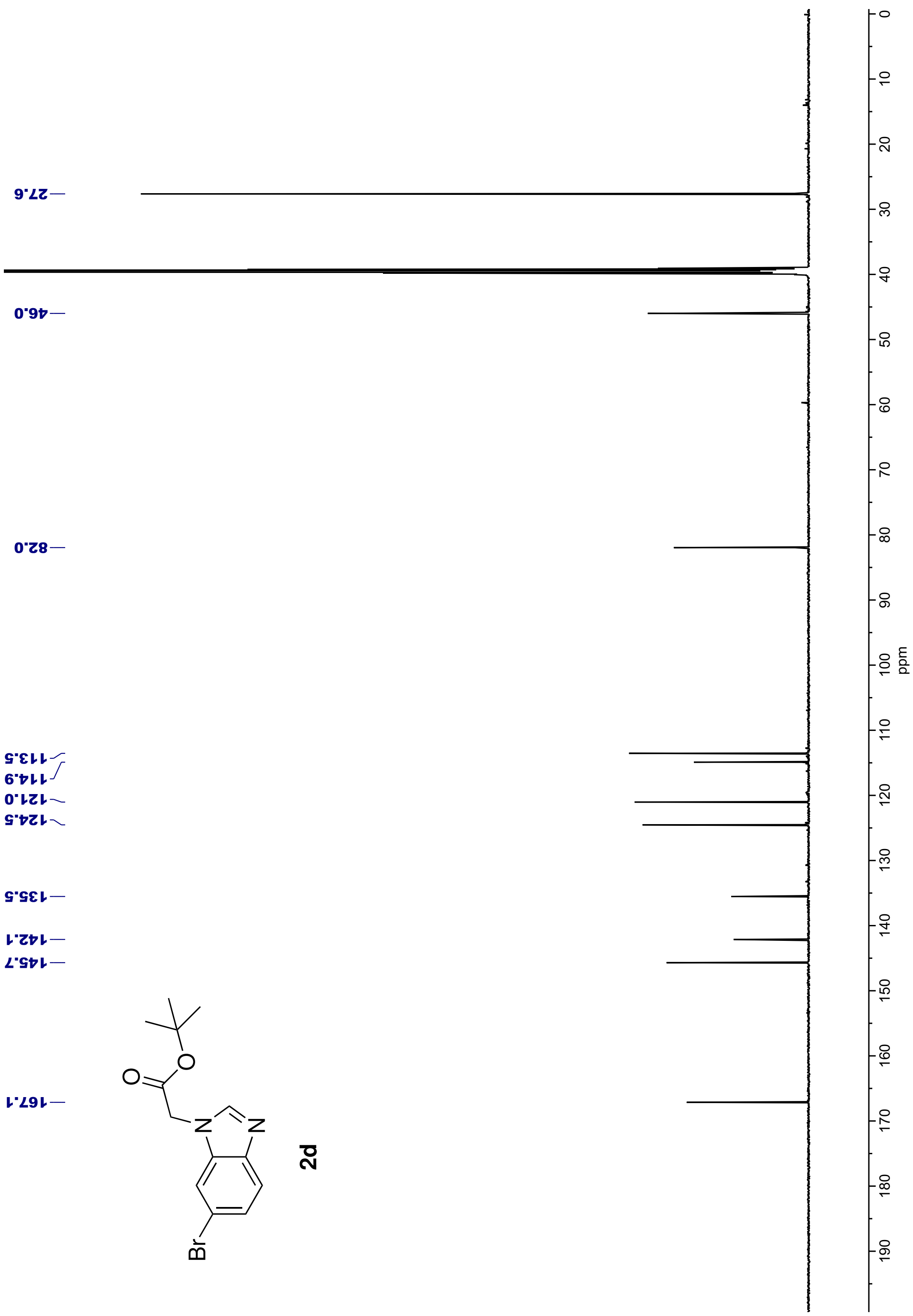

Figure 6.11: ^{13}C NMR (151 MHz, DMSO–d_6) spectrum of **2d**.

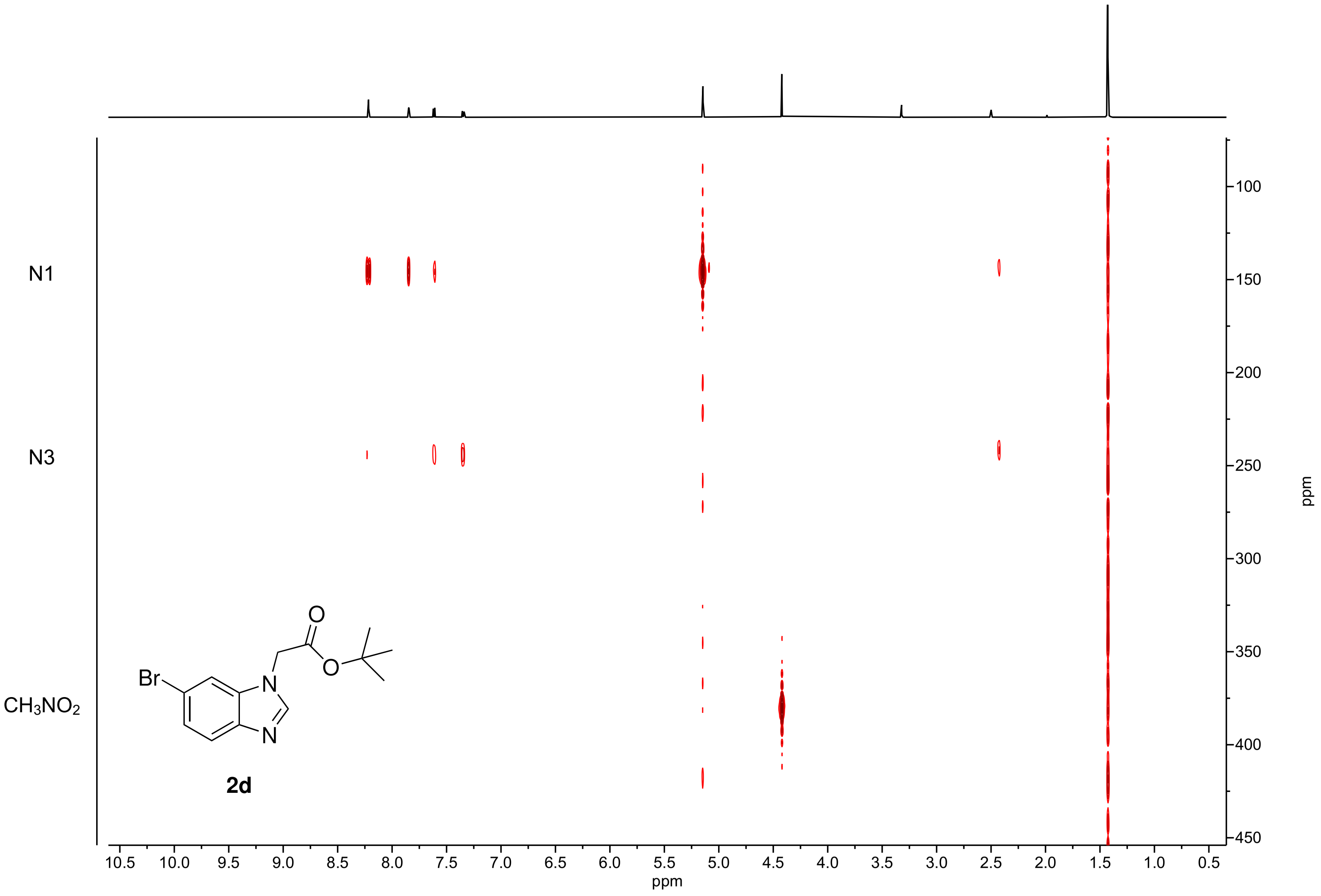

Figure 6.12: ^{1}H–^{15}N HMBC (600 MHz, DMSO–d$_6$) spectrum of **2d** with CH$_3$NO$_2$ as an internal standard. The correlations arising from a signal at 2.43 ppm are from an unknown benzimidazole impurity.

6.4 Synthesis of compounds in Route III

tert–Butyl 2–(6–bromobenzotriazol–1–yl)acetate (3d)

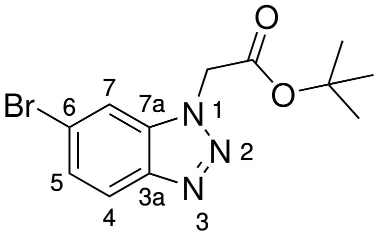

The compound was prepared based on a reported procedure by Azeez *et al.* [84]
A solution of *tert*–butyl (2–amino–5–bromophenyl)glycinate (**2c**) (131 mg, 0.433 mmol, 1.00 eq.) in acetonitrile (2.15 mL) was treated with *tert*–butyl nitrite (100 µL, 0.841 mmol, 1.94 eq.) and stirred at room temperature for 15 min. The solvent was evaporated under reduced pressure and the residual oil was dissolved in ethyl acetate (15 mL). The resulting solution was washed with water, saturated $NaHCO_3$, water again and brine (all 10 mL) before being dried over $MgSO_4$ and filtered by gravity. Evaporation under reduced pressure gave **3d** as a maroon solid. The compound was used in the next reaction without further purification.
Yield: 125 mg (93 %)

^{1}H NMR (600 MHz, DMSO–d$_6$): δ (ppm) **8.25** (d, 1 H, J = 1.8 Hz, H7), **8.05** (d, 1 H, J = 8.8 Hz, H4), **7.56** (dd, 1 H, J = 8.8, 1.7 Hz, H5), **5.65** (s, 2 H, CH_2), **1.42** (s, 9 H, $C(CH_3)_3$)

^{13}C NMR (151 MHz, DMSO–d$_6$): δ (ppm) **166.1** (C=O), **143.9** (C3a), **134.7** (C7a), **127.3** (C5), **120.9** (C4 + C6[II]), **113.8** (C7), **82.5** (**C**$(CH_3)_3$), **49.3** (CH_2), **27.6** (C(**C**$H_3)_3$)

^{15}N{^{1}H} NMR (600 MHz, DMSO–d$_6$): δ (ppm) **382.8** (N1), **342.9** (N3), **219.0** (N2)

IR (ATR): $\tilde{\nu}$ (cm^{-1}) **2988** (C–H), **1744** (C=O), **1456** (C–H), **1366** (C–N), **1242** (C–O), **1153** (C–O), **810** (Benzotriazole ring[III])

HRMS (ESI, CH_3CN): m/z $[C_{12}H_{14}BrN_3O_2 + Na]^+$:
calcd.: **334.0162** / **336.0142**, found: **334.0161** / **336.0141**

mp: 103–106 °C

[II] The signal from C6 was made visible using a ^{1}H coupled ^{13}C NMR experiment.
[III] Observed in region typical of ring–bending modes. [108, 109]

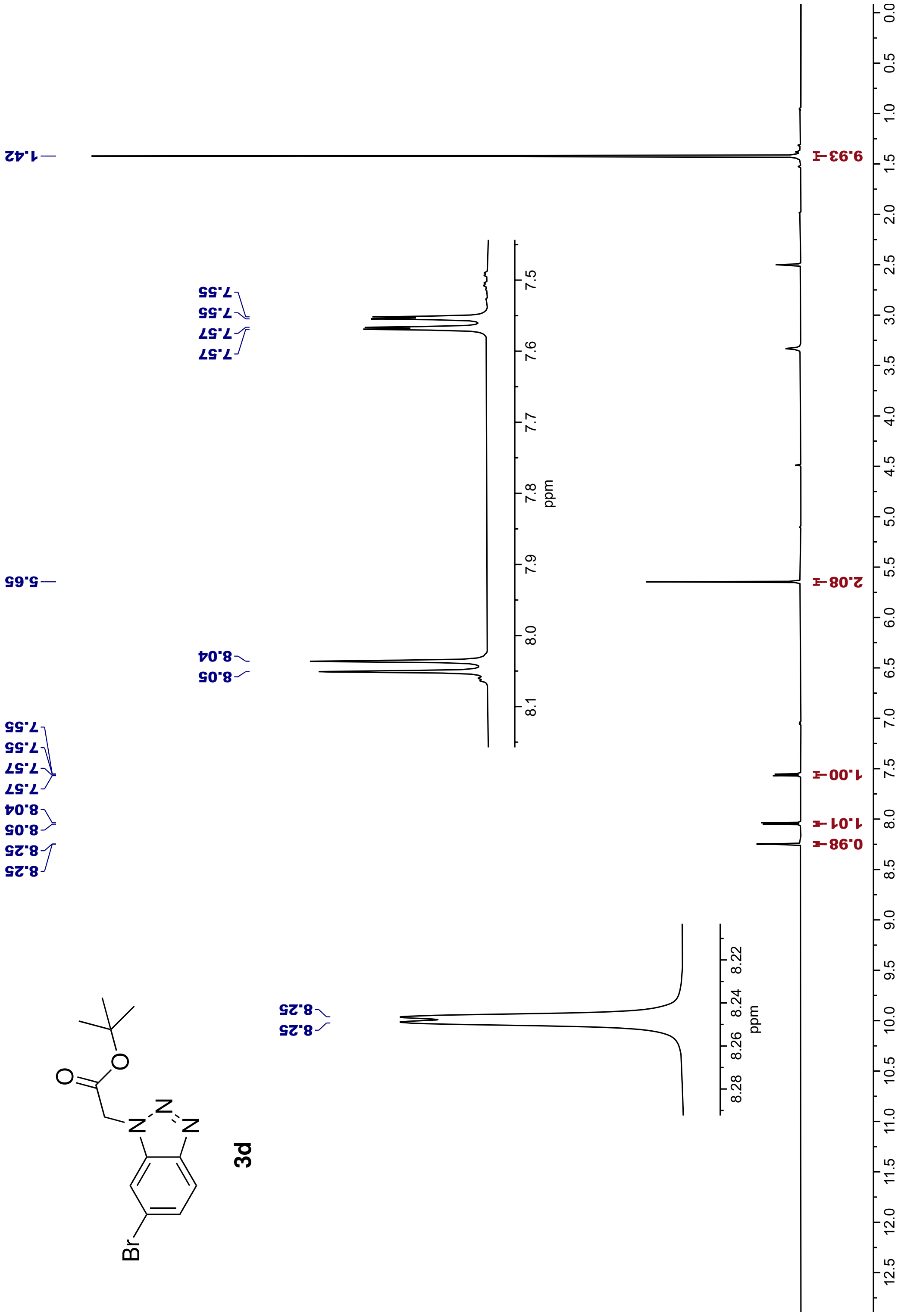

3d

Figure 6.13: ^{1}H NMR (600 MHz, DMSO–d$_6$) spectrum of **3d**.

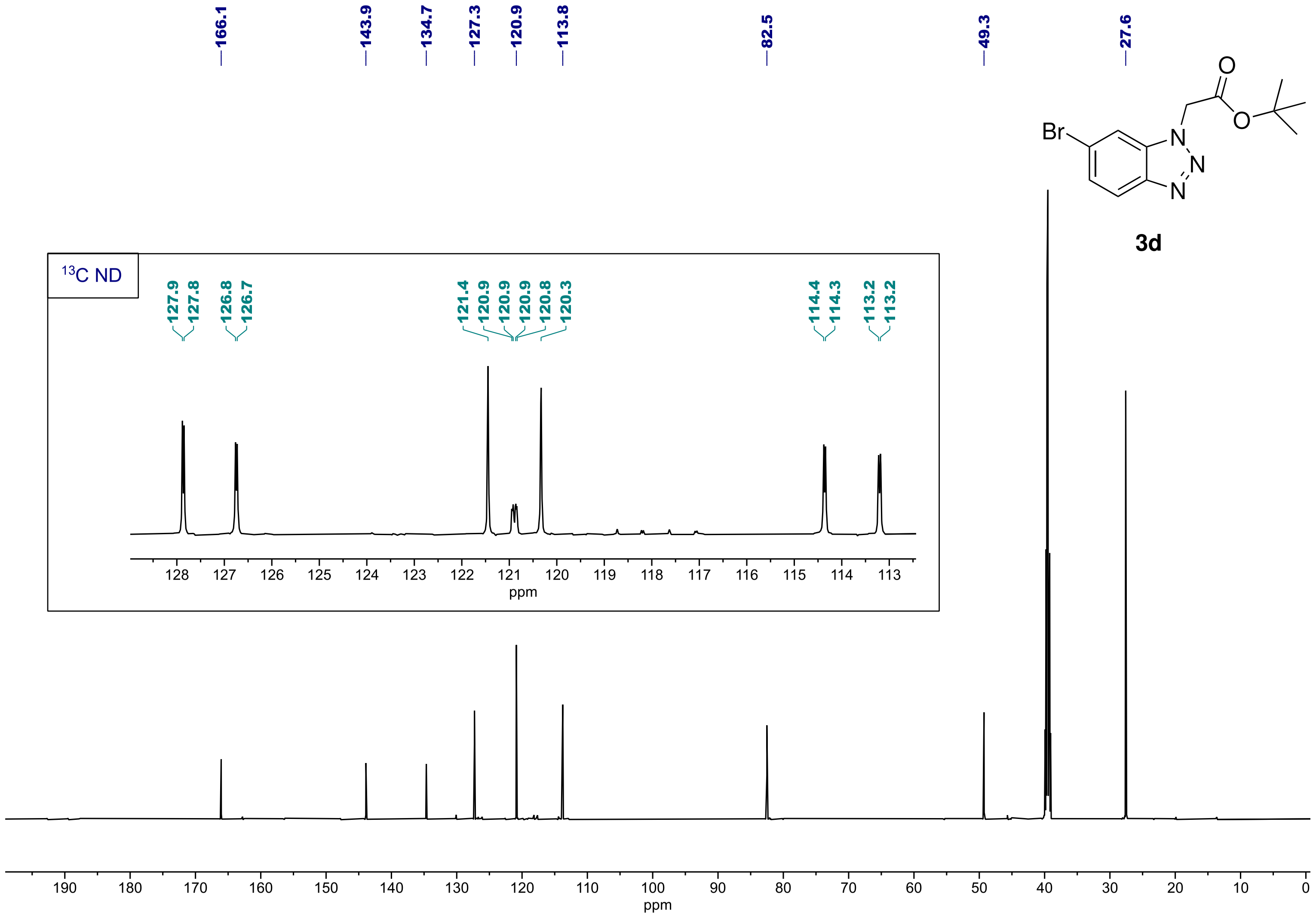

Figure 6.14: ^{13}C NMR (151 MHz, DMSO–d$_6$) spectrum of **3d**. Inset of a non–decoupled ^{13}C NMR spectrum, revealing the C6 signal at 120.9 ppm from underneath the more intense C4 signal.

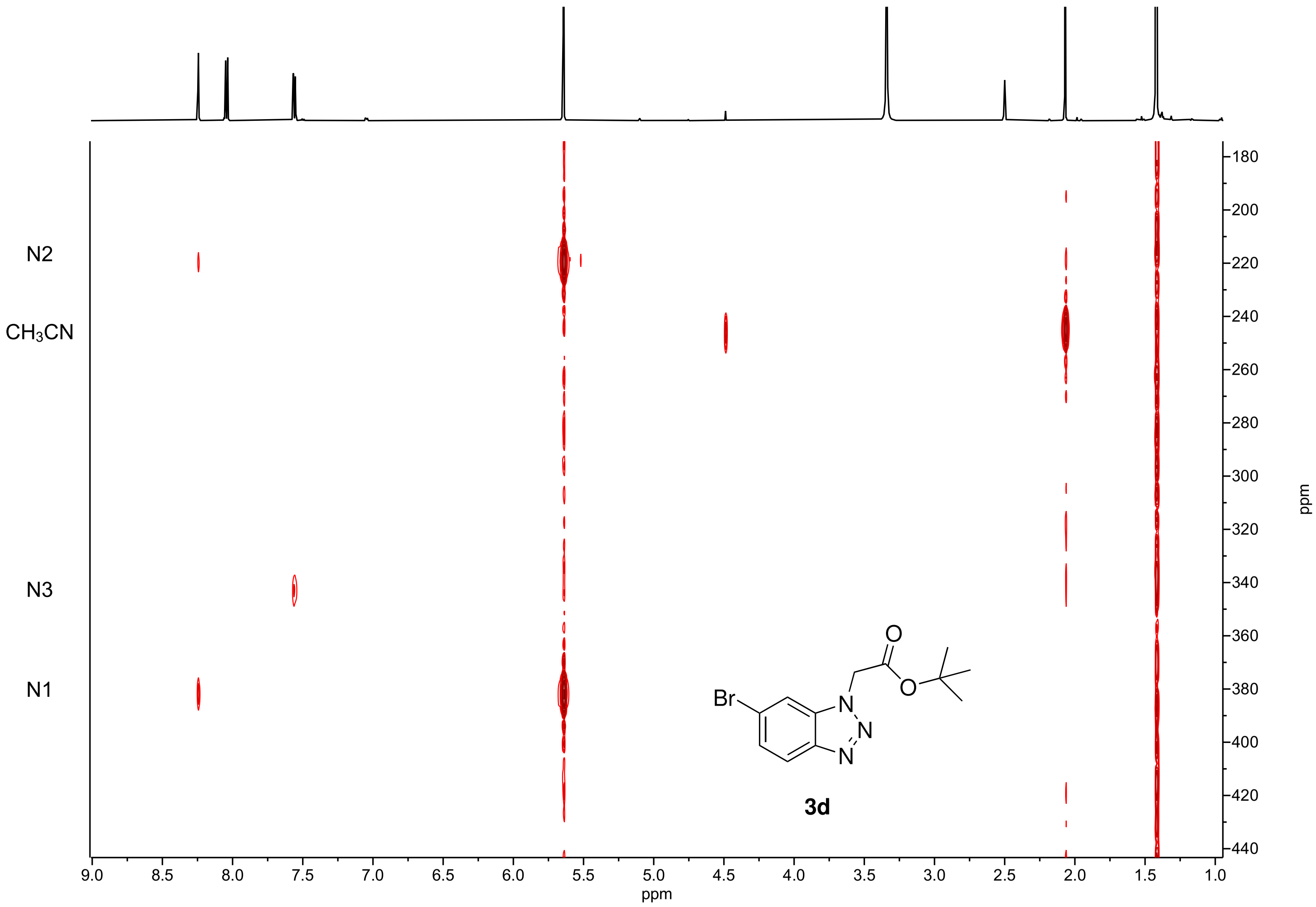

Figure 6.15: ^{1}H–^{15}N HMBC (600 MHz, DMSO–d$_6$) spectrum of **3d** with CH$_3$CN as an internal standard.

6.5 Synthesis of compounds in Route IV

Ethyl 2–(6–bromo–1–hydroxyindan–1–yl)acetate (4b)

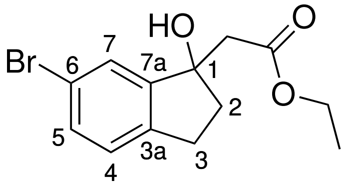

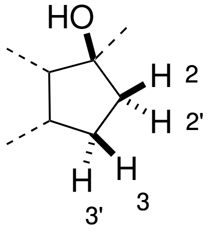

The compound was prepared based on a reported procedure by Alcalde *et al.* [90]
A 1.0 M THF solution of lithium bis(trimethylsilyl)amide (2.20 mL, 0.220 mmol, 1.10 eq.) was added to a volume of dry THF (5.0 mL) and cooled to −78 °C while under a nitrogen atmosphere. Dry ethyl acetate (0.210 mL, 0.215 mmol, 1.07 eq.) was added drop–wise and the solution was left to stir under nitrogen at −78 °C for 30 min. A solution of 6–bromoindan–1–one (423 mg, 2.00 mmol, 1.00 eq.) in dry THF (3.0 mL) was added and the solution was left to stir under nitrogen at −78 °C for 1 h. The resulting mixture was acidified with 1.0 M HCl (5.0 mL) and allowed to heat up to room temperature before being extracted with ethyl acetate (3 × 20 mL). The combined organic phase was washed with brine, dried over Na_2SO_4, filtered by gravity and evaporated under reduced pressure, yielding **4b** as a pale orange oil. The compound was used in the next reaction without further purification.
Yield: 551 mg (92 %)

^{1}H NMR (800 MHz, DMSO–d$_6$): δ (ppm) **7.48** (d, 1 H, J = 1.9 Hz, H7), **7.38** (dd, 1 H, J = 8.0, 1.9 Hz, H5), **7.17** (d, 1 H, J = 8.0 Hz, H4), **5.40** (s, 1 H, OH), **3.98** (ABX$_3$qq, 2 H, J = 10.8, 7.1 Hz, $\Delta\delta$ = 0.02 ppm, OCH$_2$), **2.86** (ddd, 1 H, J = 16.1, 8.5, 4.9 Hz, H3), **2.74–2.67** (m, 1 H, H3'), **2.73** (ABq, 2 H, J = 13.9 Hz, $\Delta\delta$ = 0.07 ppm, CH$_2$CO), **2.45** (ddd, 1 H, J = 13.1, 8.2, 4.8 Hz, H2'), **2.06** (ddd, 1 H, J = 13.1, 8.5, 6.6 Hz, H2), **1.10** (t, 3 H, J = 7.1 Hz, CH$_3$)

^{13}C NMR (201 MHz, DMSO–d$_6$): δ (ppm) **169.9** (C=O), **150.2** (C7a), **141.9** (C3a), **130.4** (C5), **126.7** (C4), **126.3** (C7), **119.0** (C6), **80.3** (C1), **59.6** (OCH$_2$), **44.6** (**C**H$_2$CO), **39.4** (C2), **28.6** (C3), **14.0** (CH$_3$)

IR (ATR): $\widetilde{\nu}$ (cm^{-1}) **3454** (broad O–H), **2978** (C–H), **2937** (C–H), **1709** (C=O), **1468** (C–H), **1186** (C–O)

HRMS (ESI, CH$_3$CN): m/z $[C_{13}H_{15}BrO_3 + Na]^+$:
calcd.: **321.0097 / 323.0077**, found: **321.0097 / 323.0077**

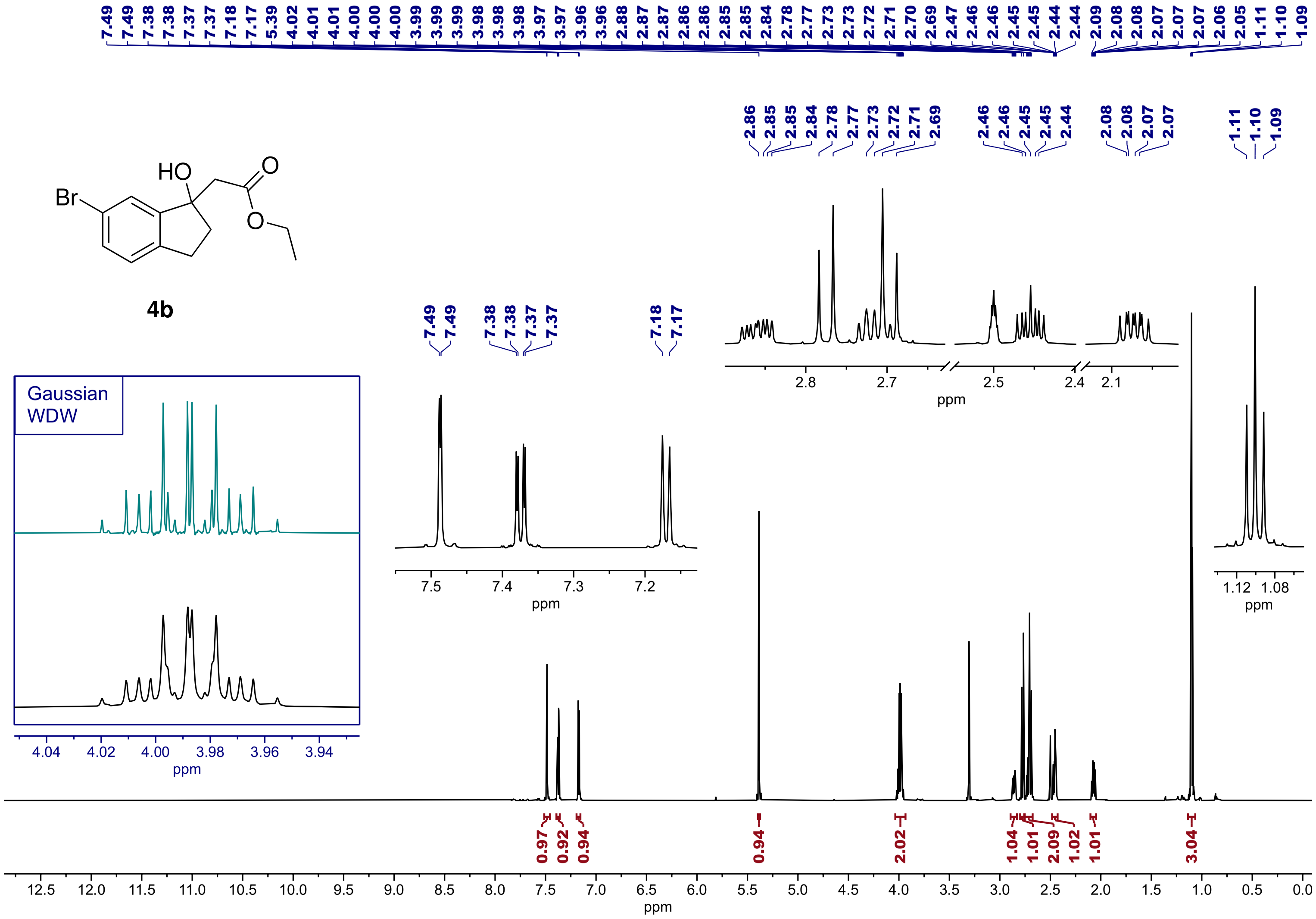

Figure 6.16: ^{1}H NMR (800 MHz, DMSO–d$_6$) spectrum of **4b**. Left inset shows the ABX$_3$ quartet of quartets at 3.99 ppm processed with a Gaussian window function (LB = −0.60 Hz, GB = 0.30), revealing all sixteen subsignals.

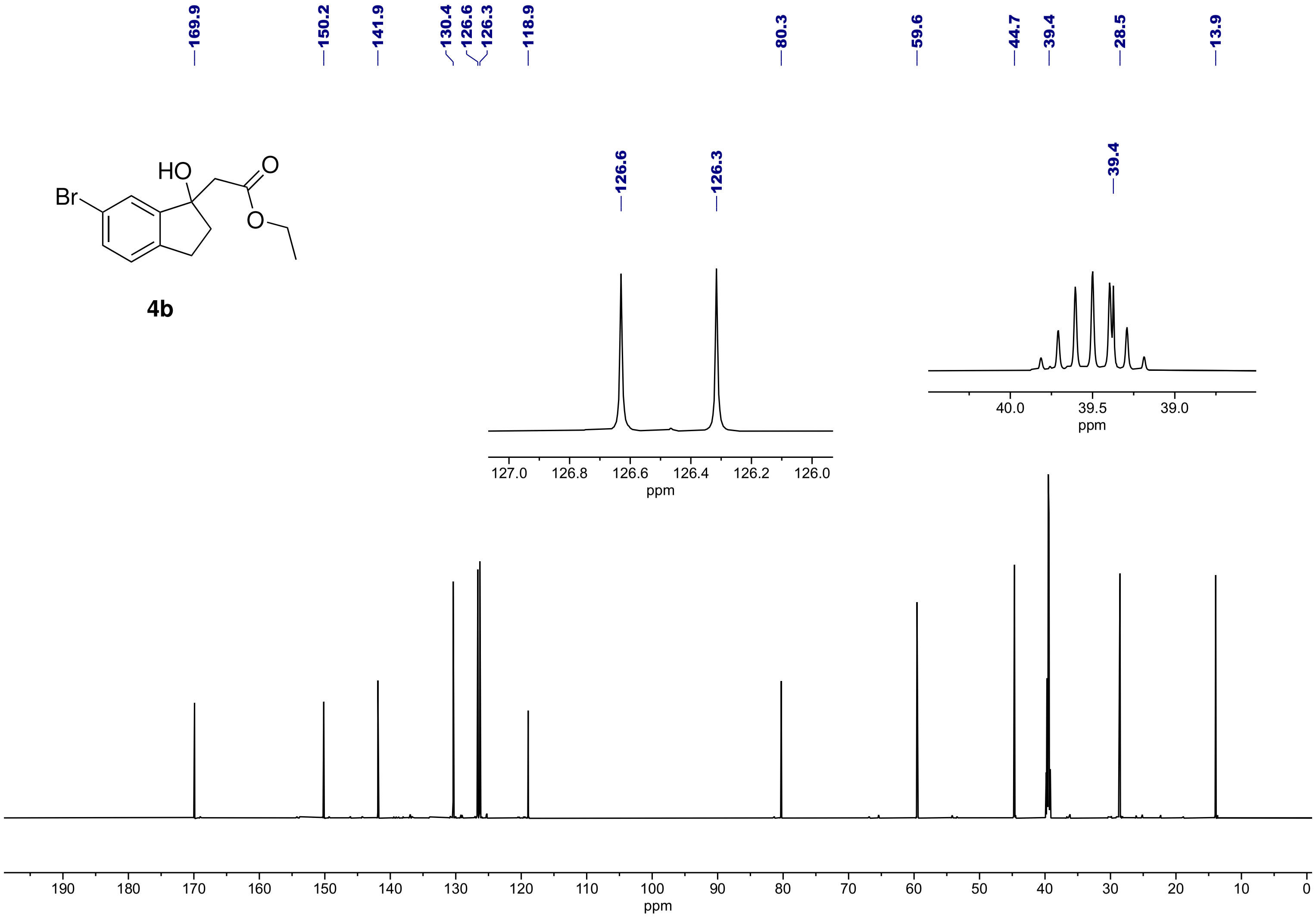

Figure 6.17: ^{13}C NMR (201 MHz, DMSO–d_6) spectrum of **4b**.

Ethyl 2–(5–bromoinden–3–yl)acetate (4c)

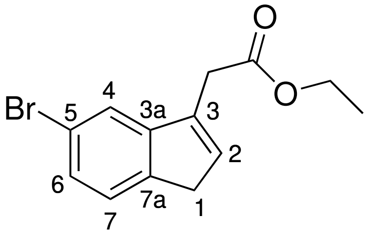

The compound was prepared based on a reported procedure by Alcalde *et al.* [90]
A solution of ethyl 2–(6–bromo–1–hydroxyindan–1–yl)acetate (**4b**) (1.11 g, 3.70 mmol, 1.00 eq.) in dichloromethane (23.5 mL) was added trifluoroacetic acid (6.76 mL, 88.2 mmol, 23.8 eq.) and left to stir in darkness at room temperature for 24 h. The solution was diluted with dichloromethane (20 mL) and washed several times with water until the aqueous phase maintained a neutral pH. The organic phase was then washed with brine and dried over $MgSO_4$ before being filtered by gravity and concentrated under reduced pressure. The resulting crude oil was purified by column chromatography (silica gel, 7:3 CH_2Cl_2/Hexane) yielding **4c** as a pale yellow oil which crystallised upon cooling.
Yield: 539 mg (52 %)

^{1}H NMR (600 MHz, DMSO–d_6): δ (ppm) **7.54** (d, 1 H, J = 1.8 Hz, H4), **7.42** (d, 1 H, J = 7.9 Hz, H7), **7.36** (dd, 1 H, J = 7.9, 1.8 Hz, H6), **6.52** (br m, 1 H, H2), **4.10** (q, 2 H, J = 7.1 Hz, OCH_2), **3.65** (br m, 2 H, CH_2CO), **3.37** (br m, 2 H, H1), **1.19** (t, 3 H, J = 7.1 Hz, CH_3)

^{13}C NMR (151 MHz, DMSO–d_6): δ (ppm) **170.2** (C=O), **146.8** (C3a), **142.9** (C7a), **136.0** (C3), **134.0** (C2), **127.1** (C6), **125.5** (C7), **122.3** (C4), **119.2** (C5), **60.3** (OCH_2), **37.3** (C1), **33.1** (**C**H_2CO), **14.0** (CH_3)

IR (ATR): $\widetilde{\nu}$ (cm^{-1}) **2980** (C–H), **2922** (C–H), **1720** (C=O), **1597** (C=C), **1456** (C–H), **1194** (C–O)

HRMS (ESI, CH_3CN): m/z $[C_{13}H_{13}BrO_2 + Na]^+$:
calcd.: **302.9991** / **304.9970**, found: **302.9991** / **304.9971**

R_f (7:3 CH_2Cl_2/Hexane): 0.35

mp: 42–44 °C

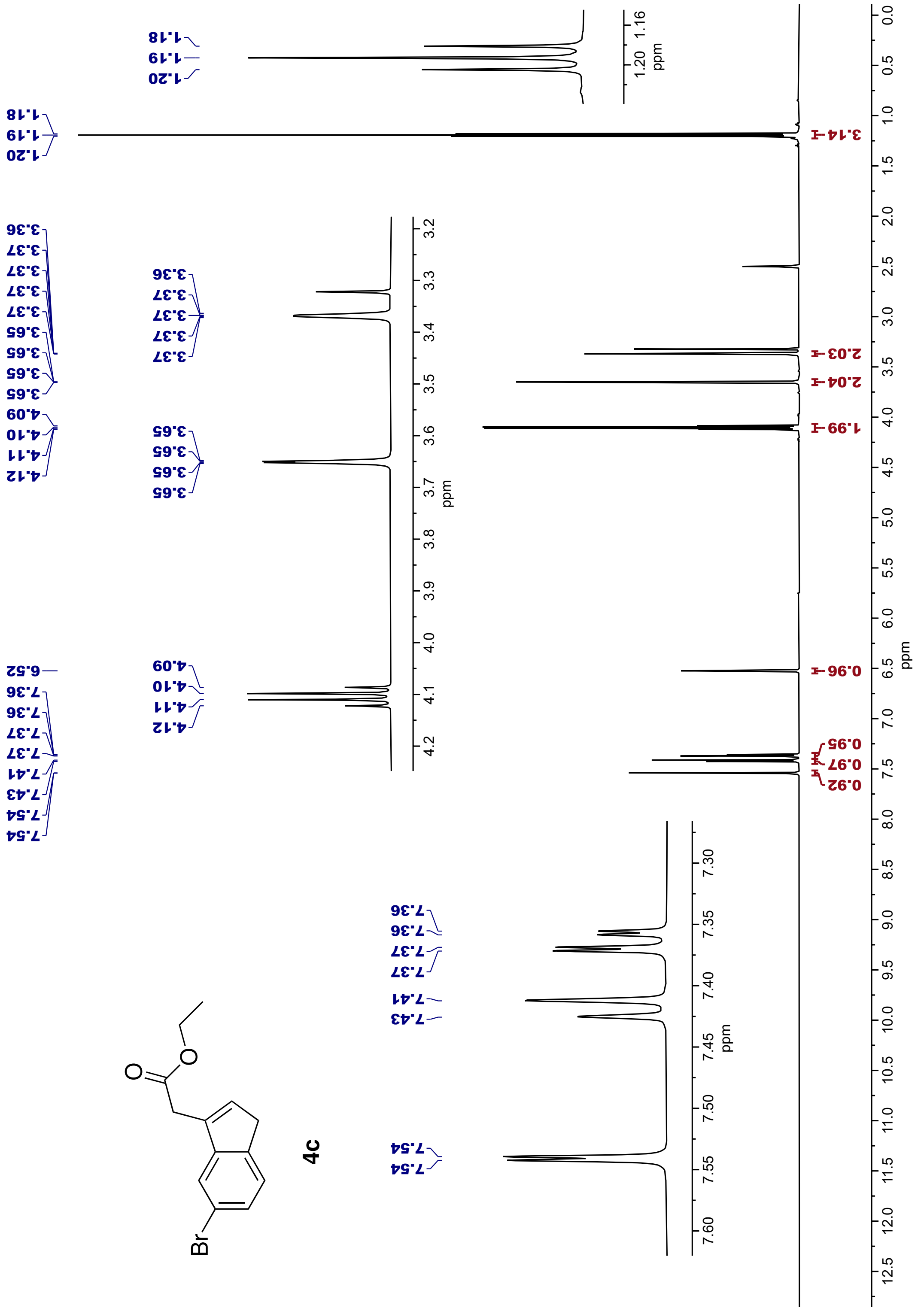

Figure 6.18: ^{1}H NMR (600 MHz, DMSO–d_6) spectrum of **4c**.

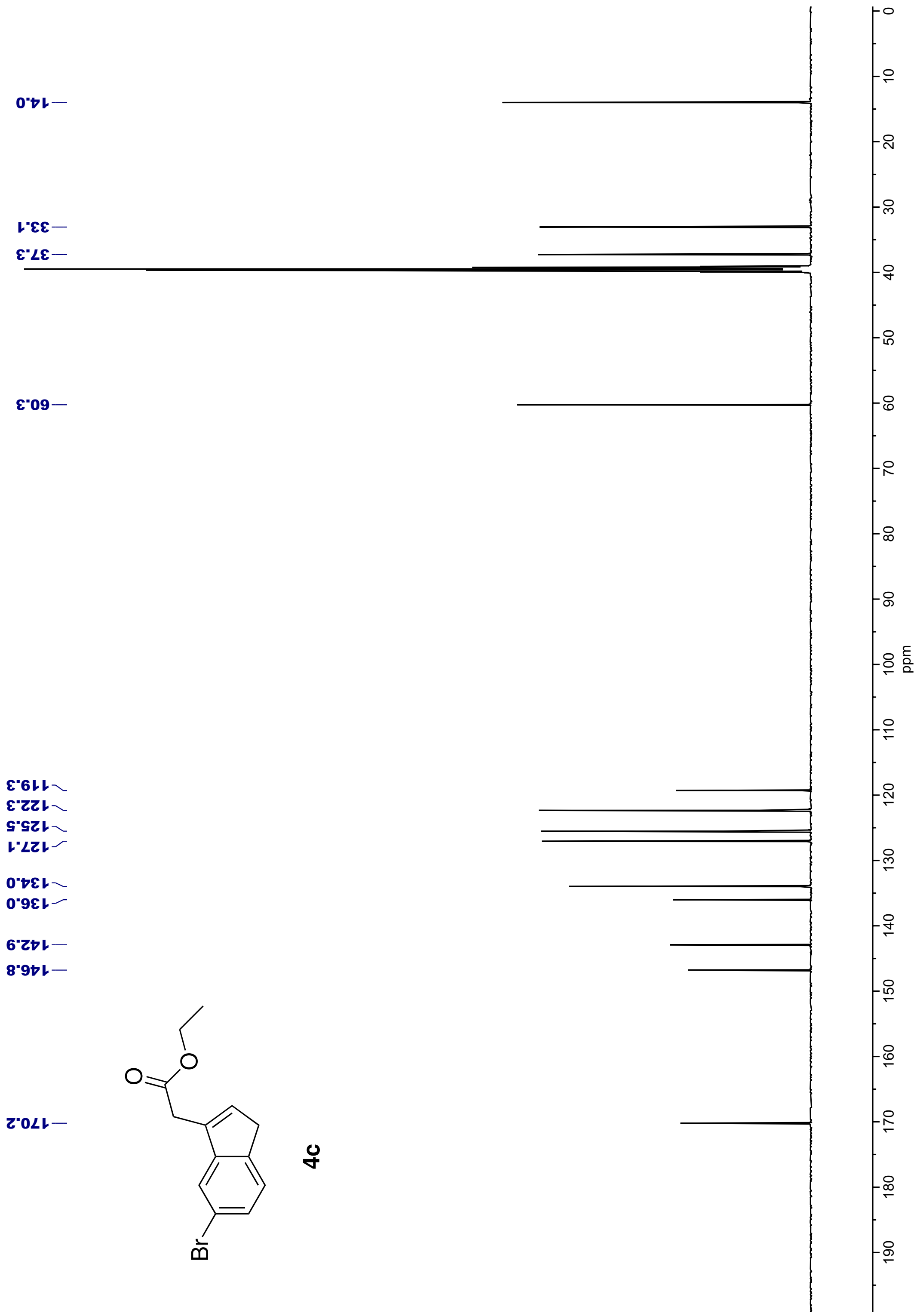

Figure 6.19: ^{13}C NMR (151 MHz, DMSO–d_6) spectrum of **4c**.

2–(5–Bromoinden–3–yl)acetohydroxamic acid (4e)

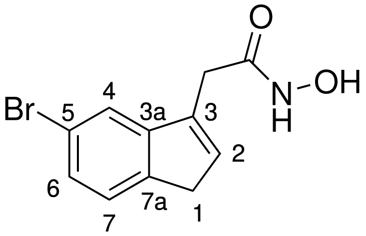

The compound was prepared based on a reported procedure by Boularot *et al.* [49]
A solution of ethyl 2–(5–bromoinden–3–yl)acetate (**4c**) (200 mg, 0.711 mmol, 1.00 eq.) in dry ethanol (7.2 mL) was added to a dry ethanol (9.4 mL) suspension of hydroxylammonium chloride (494 mg, 7.10 mmol, 9.98 eq.) and potassium *tert*–butoxide (798 mg, 7.12 mmol, 10.0 eq.) and stirred under nitrogen at 80 °C for 24 h. The resulting suspension was concentrated under reduced pressure before being diluted by ethyl acetate (50 mL). The resulting solution was washed with water (3 × 25 mL), saturated $NaHCO_3$ (25 mL), water again and brine (both 25 mL) before being dried over $MgSO_4$, filtered by gravity and evaporated under reduced pressure. The crude product was twice recrystallised from 1:1 acetone/cyclohexane *via* slow evaporation of acetone under reduced pressure. Washing with cyclohexane and evaporating to dryness yielded **4e** as a white solid.
Yield: 86.7 mg (45 %)

^{1}H NMR (600 MHz, DMSO–d$_6$): δ (ppm) **10.66** (br s, 1 H, N**H**OH), **8.86** (br s, 1 H, NHO**H**), **7.62** (d, 1 H, J = 1.7 Hz, H4), **7.41** (d, 1 H, J = 7.9 Hz, H7), **7.35** (dd, 1 H, J = 7.9, 1.8 Hz, H6), **6.46** (br m, 1 H, H2), **3.34** (br m, 2 H, H1), **3.27** (br m, 2 H, CH_2CO)

^{13}C NMR (151 MHz, DMSO–d$_6$): δ (ppm) **166.0** (C=O), **147.0** (C3a), **143.0** (C7a), **137.2** (C3), **133.6** (C2), **127.0** (C6), **125.5** (C7), **122.4** (C4), **119.3** (C5), **37.2** (C1), **32.1** (**C**H_2CO)

^{15}N{^{1}H} NMR (600 MHz, DMSO–d$_6$): δ (ppm) **166.9** (NHOH)

IR (ATR): $\widetilde{\nu}$ (cm^{-1}) **3240** (O−H), **3032** (N−H), **1632** (C=O), **1597** (C=C), **1454** (C−H)

HRMS (ESI, CH_3CN): m/z $[C_{11}H_{10}BrNO_2 + Na]^+$:
calcd.: **289.9787 / 291.9766**, found: **289.9786 / 291.9766**

mp: 157–159 °C

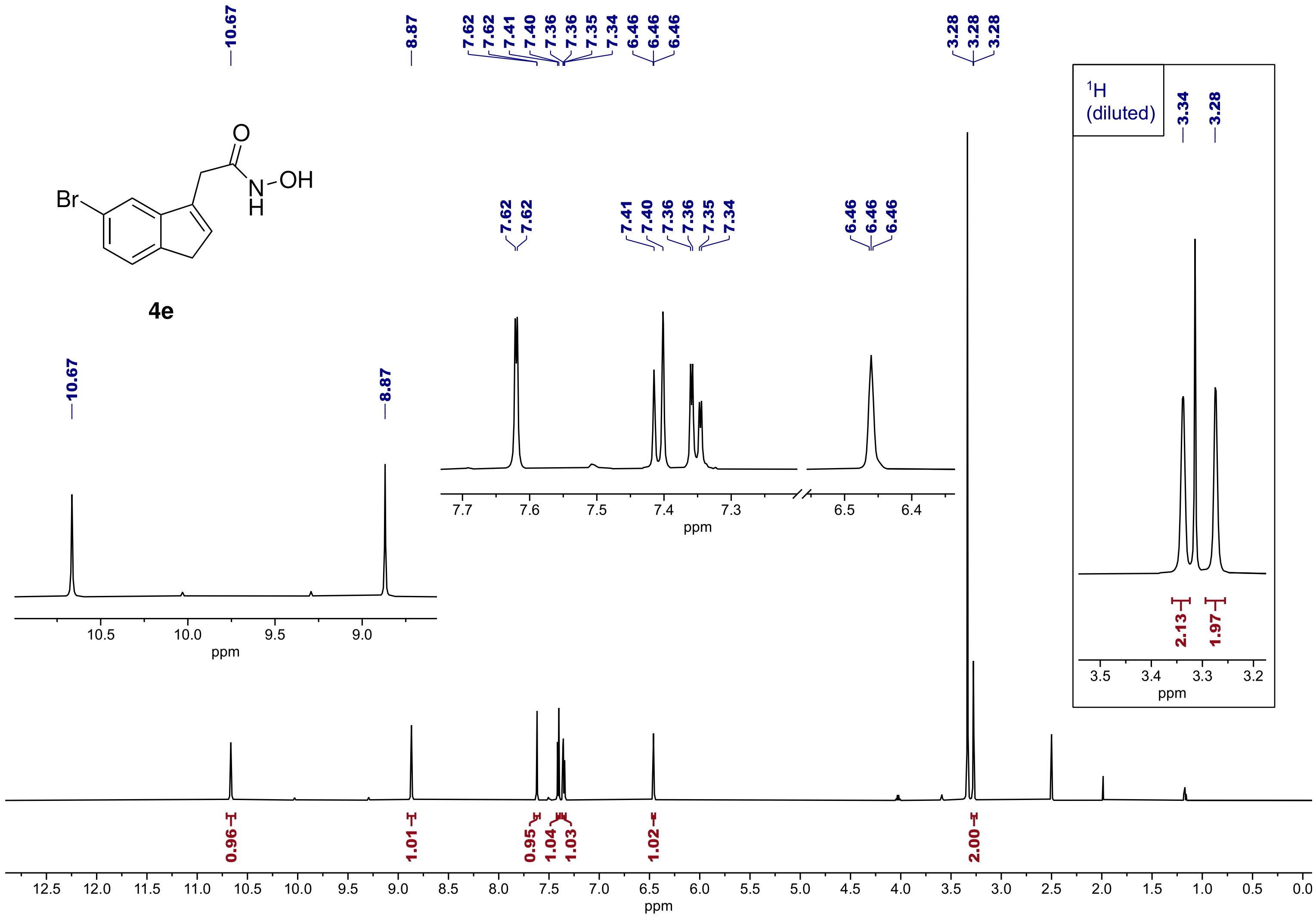

Figure 6.20: ^{1}H NMR (600 MHz, DMSO–d$_6$) spectrum of **4e**. Right inset is from a less concentrated NMR sample, revealing the H1 methylene signal at 3.34 ppm from underneath the water resonance.

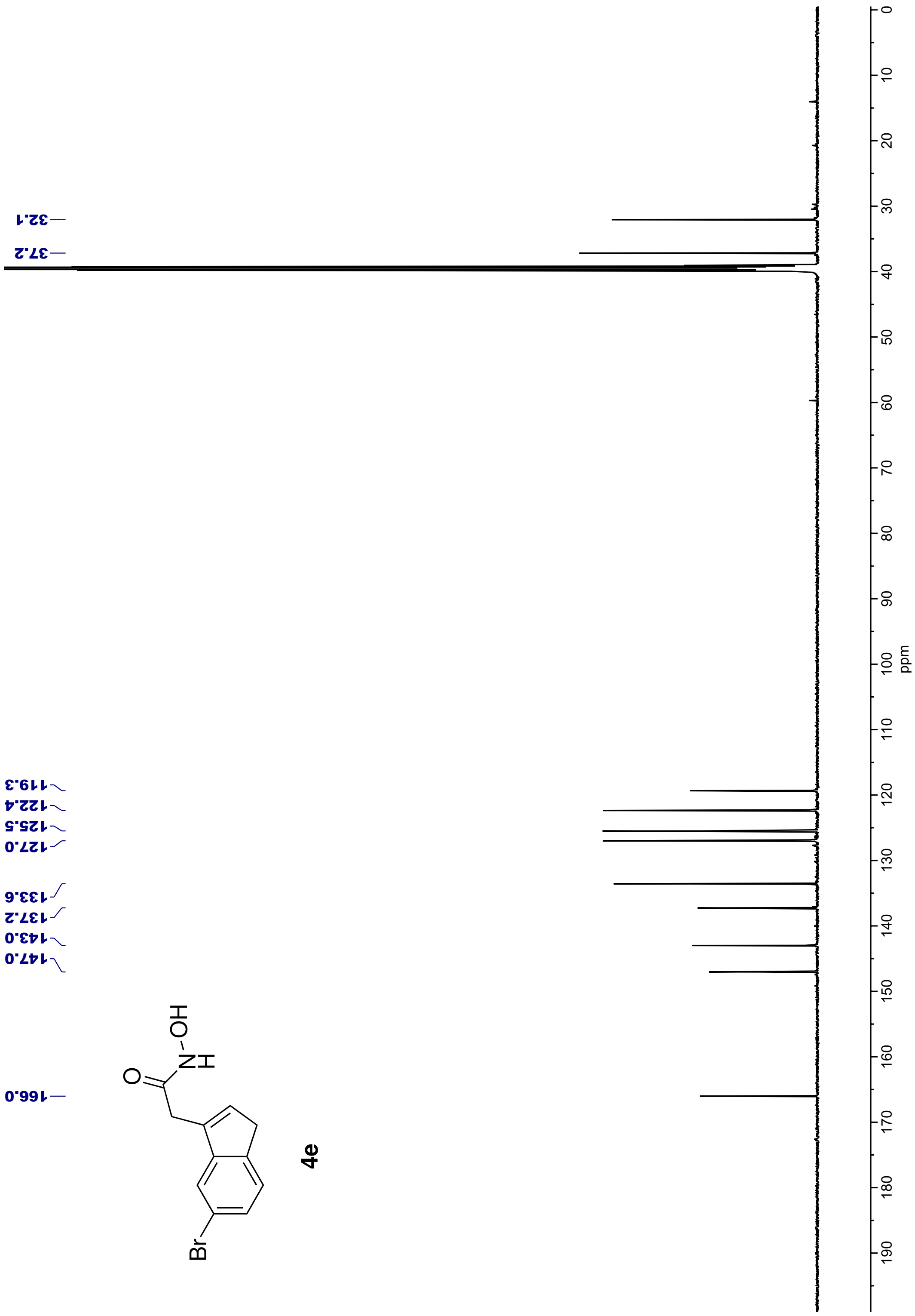

Figure 6.21: ^{13}C NMR (151 MHz, DMSO–d$_6$) spectrum of **4e**.

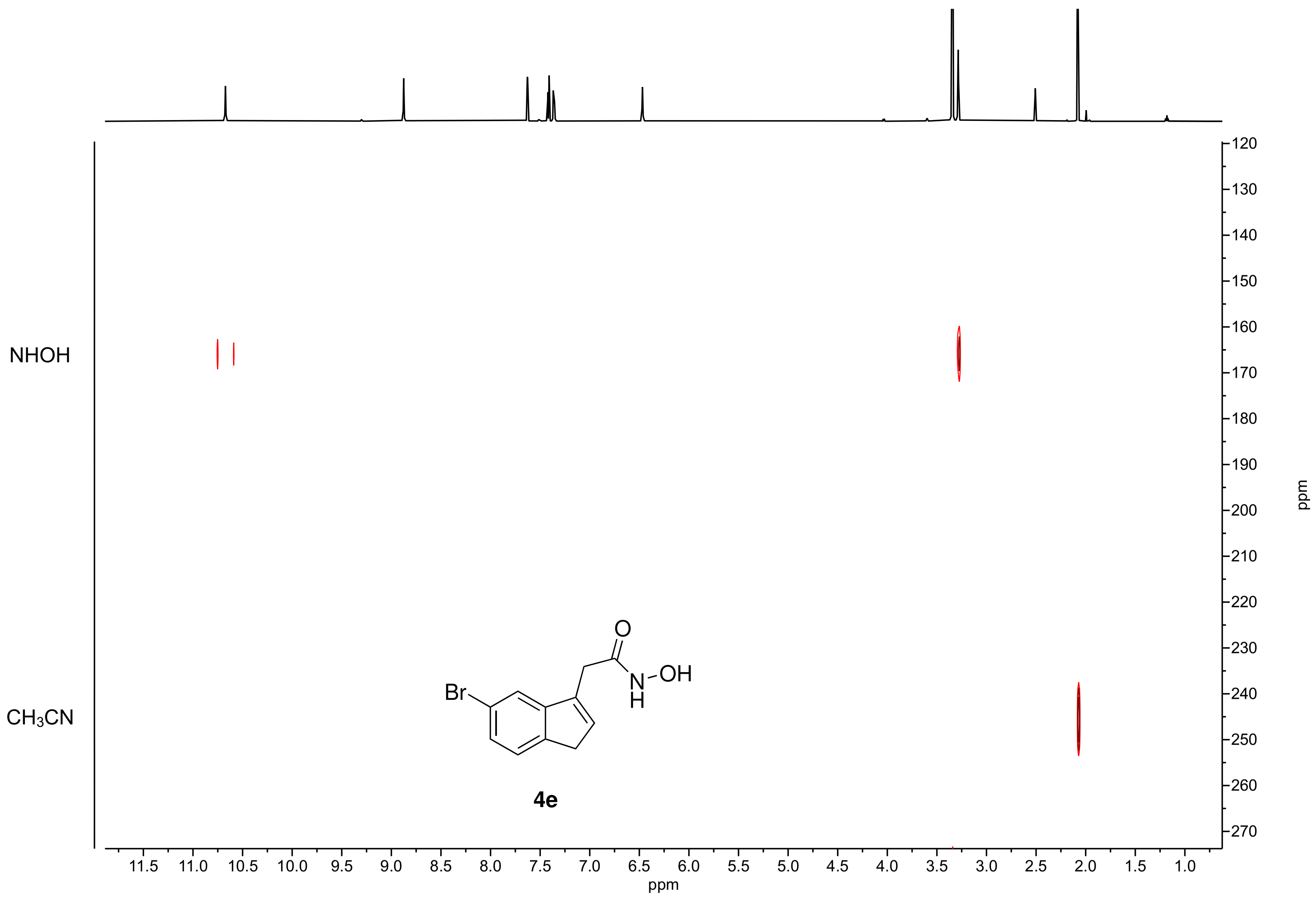

Figure 6.22: ^{1}H–^{15}N HMBC (600 MHz, DMSO–d_6) spectrum of **4e** with CH_3CN as an internal standard.

6.6 Synthesis of compounds in Route V

Ethyl (*E*)–2–(6–bromoindan–1–ylidene)acetate (5c)

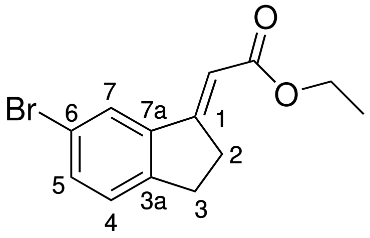

The compound was formed as a side product in the synthesis of compound **4c** and was purified by column chromatography (silica gel, 7:3 CH_2Cl_2/Hexane) yielding a pale yellow solid.
Yield: 298 mg (29 %)

^{1}H NMR (600 MHz, DMSO–d_6): δ (ppm) **8.05** (d, 1 H, J = 1.8 Hz, H7), **7.53** (dd, 1 H, $J = 8.1, 1.9$ Hz, H5), **7.34** (d, 1 H, J = 8.1 Hz, H4), **6.49** (t, 1 H, J = 2.7 Hz, CHCO), **4.13** (q, 2 H, J = 7.1 Hz, OCH_2), **3.18–3.15** (m, 2 H, H2), **3.36** (t, 2 H, J = 6.2 Hz, H3) **1.24** (t, 3 H, J = 7.1 Hz, CH_3)

^{13}C NMR (151 MHz, DMSO–d_6): δ (ppm) **166.3** (C=O), **161.0** (C1), **148.2** (C3a), **141.9** (C7a), **133.4** (C5), **127.5** (C4), **124.9** (C7), **120.2** (C6), **109.1** (**C**HCO), **59.3** (OCH_2), **30.9** (C2), **29.7** (C3), **14.2** (CH_3)

IR (ATR): $\widetilde{\nu}$ (cm^{-1}) **3055** (C–H), **2978** (C–H), **2926** (C–H), **1682** (C=O), **1620** (C=C), **1464** (C–H), **1290** (C–O)

HRMS (ESI, CH_3CN): m/z $[C_{13}H_{13}BrO_2 + Na]^+$:
calcd.: **302.9991** / **304.9970**, found: **302.9990** / **304.9970**

R_f (7:3 CH_2Cl_2/Hexane): 0.29

mp: 90–92 °C

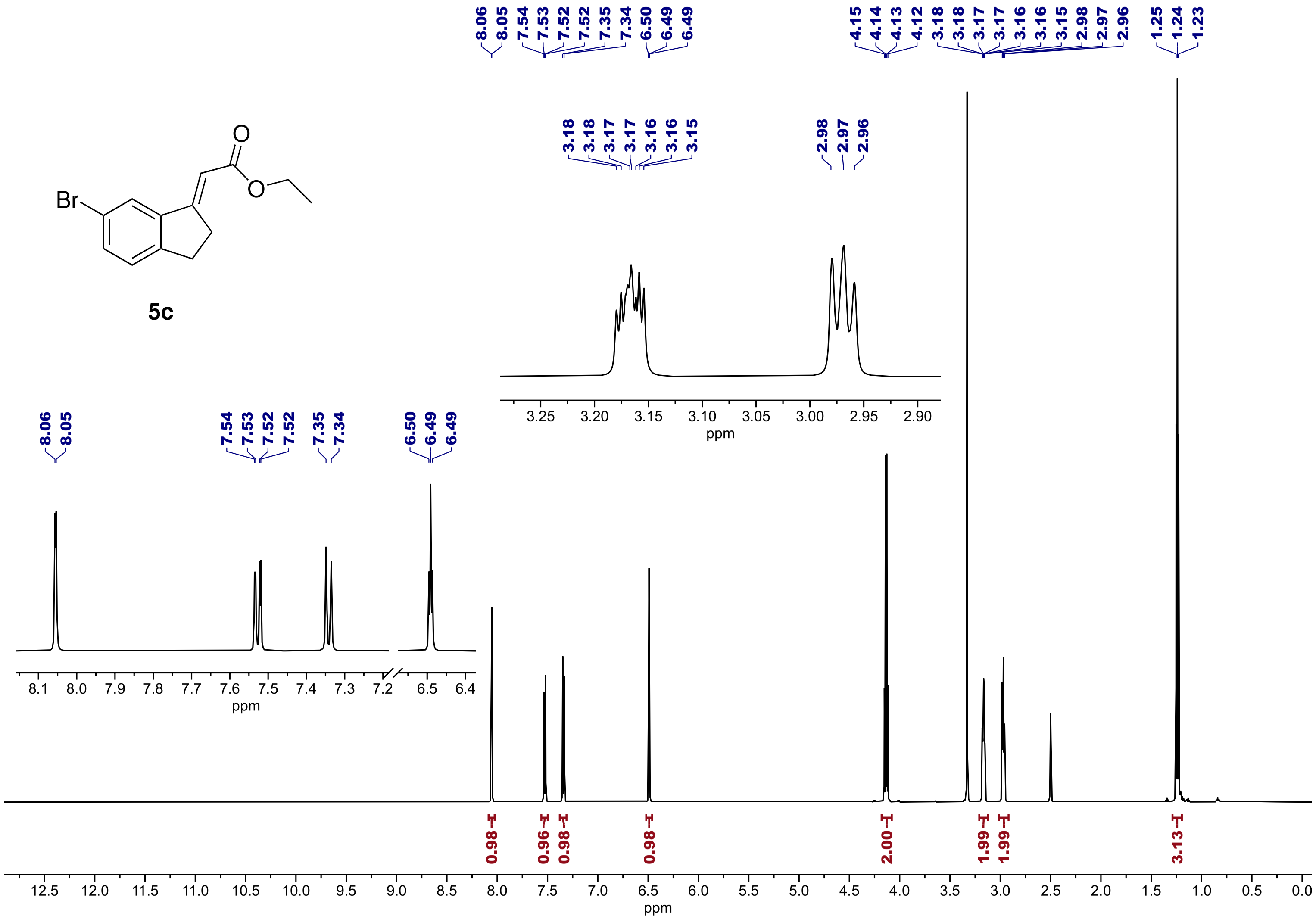

Figure 6.23: ^{1}H NMR (600 MHz, DMSO–d_6) spectrum of **5c**.

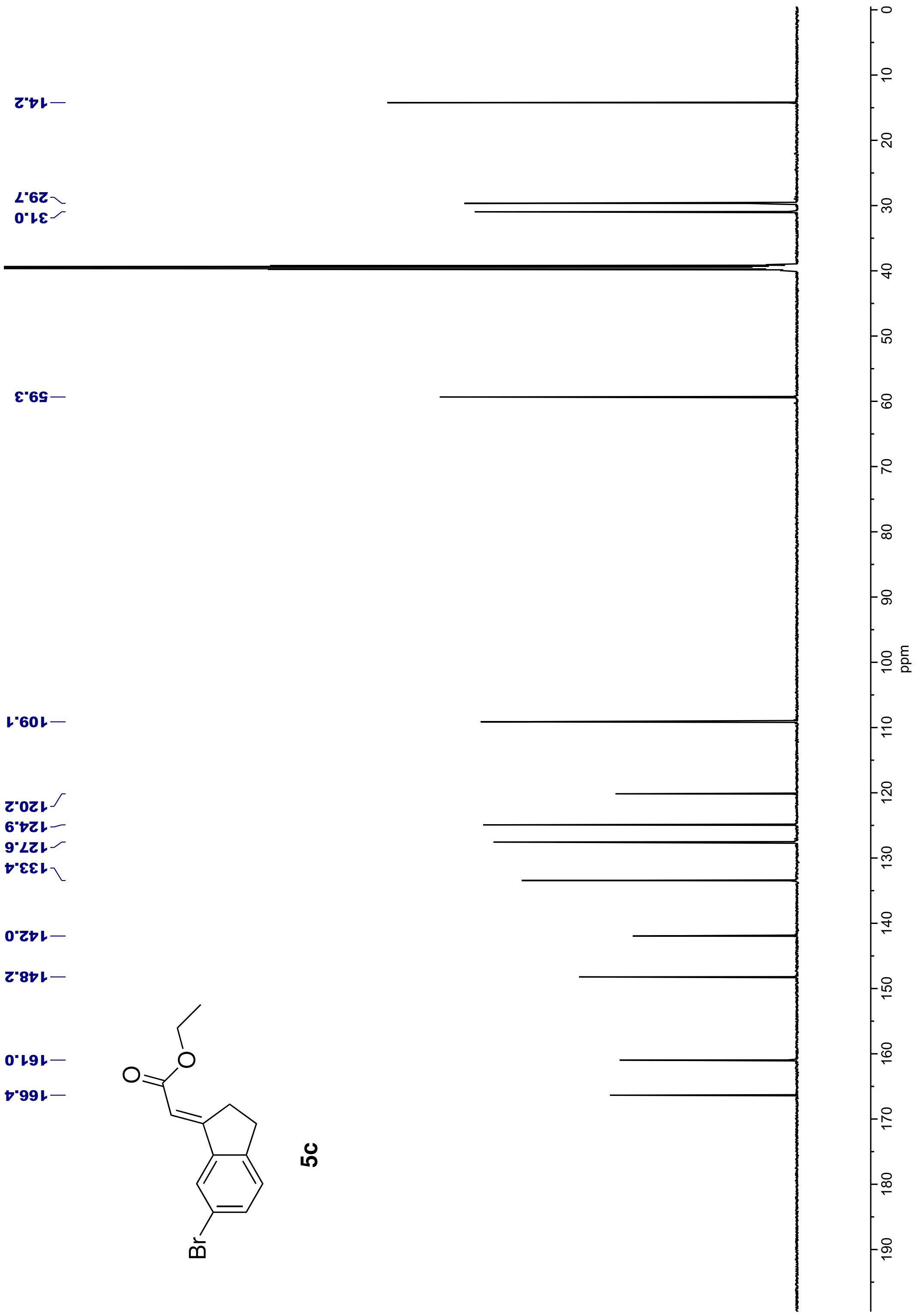

Figure 6.24: ^{13}C NMR (151 MHz, DMSO–d$_6$) spectrum of **5c**.

Bibliography

[1] Interagency Coordination Group on Antimicrobial Resistance, *No Time to Wait: Securing the future from drug–resistant infections;* World Health Organization: Geneva, 2019.

[2] J. O'Neill, Tackling drug–resistant infections globally: final report and recommendations. In *Review on Antimicrobial Resistance*; U.K. Government: London, 2016.

[3] World Health Organization, *Global Action Plan on Antimicrobial Resistance;* Geneva, 2015.

[4] World Bank, *Drug–resistant infections: A threat to our economic future;* Washington, D.C., 2017.

[5] A. H. Holmes, L. Moore, A. Sundsfjord, M. Steinbakk, S. Regmi, A. Karkey, P. J. Guerin, L. J. Piddock, *Lancet* **2016,** *387,* 176–187.

[6] M. E. Klepser, E. J. Ernst, M. A. Pfaller, *Trends Microbiol.* **1997,** *5,* 372–375.

[7] K. K. Irwin, N. Renzette, T. F. Kowalik, J. D. Jensen, *Virus Evol.* **2016,** *2,* vew014.

[8] R. I. Aminov, *Environ. Microbiol.* **2009,** *11,* 2970–2988.

[9] H. Nikaido, *Annu. Rev. Biochem.* **2009,** *78,* 119–146.

[10] World Health Organization, *2020 Antibacterial agents in clinical and preclinical development: an overview and analysis;* Geneva, 2021.

[11] Centers for Disease Control and Prevention, *Antibiotic Resistance Threats in the United States, 2013;* U.S. Department of Health and Human Services: Atlanta, GA, 2013.

[12] World Health Organization, *Global antimicrobial resistance surveillance system (GLASS) report: early implementation 2020;* Geneva, 2020.

[13] D. C. Hooper, *Clin. Infect. Dis.* **2001,** *32,* S9–S15.

[14] S. Leekha, C. L. Terrell, R. S. Edson, *Mayo Clin. Proc.* **2011,** *86,* 156–167.

[15] J. O'Neill, Securing new drugs for future generations: The pipeline of antibiotics. In *Review on Antimicrobial Resistance*; U.K. Government: London, 2015.

[16] M. I. Hutchings, A. W. Truman, B. Wilkinson, *Curr. Opin. Microbiol.* **2019,** *51,* 72–80.

[17] A. R. M. Coates, G. Halls, Y. Hu, *Br. J. Pharmacol.* **2011,** *163,* 184–194.

[18] *Drugs.com*, Diarylquinolines; `drugs.com` (Accessed: May 27th, 2021).

[19] *Drugs.com*, Oxazolidinone antibiotics; `drugs.com` (Accessed: May 27th, 2021).

[20] *Drugs.com*, Miscellaneous antibiotics; `drugs.com` (Accessed: May 27th, 2021).

[21] *DrugBank Online*, Other Macrolides; DrugBank No.: DBCAT003637; `go.drugbank.com` (Accessed: May 27th, 2021).

[22] A. Y. Chen, R. N. Adamek, B. L. Dick, C. V. Credille, C. N. Morrison, S. M. Cohen, *Chem. Rev.* **2019,** *119,* 1323–1455.

[23] *Adis Insight*, Search by Mechanism: Peptide Deformylase Inhibitors; `adisinsight.springer.com` (Accessed: June 3rd, 2021).

[24] D. Pei, *Emerging Ther. Targets* **2001,** *5,* 23–40.

[25] D. Z. Chen, D. V. Patel, C. J. Hackbarth, W. Wang, G. Dreyer, D. C. Young, P. S. Margolis, C. Wu, Z.–J. Ni, J. Trias, R. J. White, Z. Yuan, *Biochemistry* **2000,** *39,* 1256–1262.

[26] A. Becker, I. Schlichting, W. Kabsch, D. Groche, S. Schultz, A. F. V. Wagner, *Nat. Struct. Biol.* **1998,** *5,* 1053–1058.

[27] A. Becker, I. Schlichting, W. Kabsch, S. Schultz, A. F. V. Wagner, *J. Biol. Chem.* **1998,** *273,* 11413–11416.

[28] E. T. Baldwin, M. S. Harris, A. W. Yem, C. L. Wolfe, A. F. Vosters, K. A. Curry, R. W. Murray, J. H. Bock, V. P. Marshall, J. I. Cialdella, M. H. Merchant, G. Choi, M. R. Deibel, *J. Biol. Chem.* **2002,** *277,* 31163–31171.

[29] T. Meinnel, L. Patiny, S. Ragusa, S. Blanquet, *Biochemistry* **1999,** *38,* 4287–4295.

[30] Y.–J. Hu, P. T. Ravi Rajagopalan, D. Pei, *Bioorg. Med. Chem. Lett.* **1998,** *8,* 2479–2482.

[31] J. P. Hughes, S. Rees, S. B. Kalindjian, K. L. Philpott, *Br. J. Pharmacol.* **2011,** *162,* 1239–1249.

[32] J. J. Gordon, B. K. Kelly, G. A. Miller, *Nature* **1962,** *195,* 701–702.

[33] J. M. Clements, R. P. Beckett, A. Brown, G. Catlin, M. Lobell, S. Palan, W. Thomas, M. Whittaker, S. Wood, S. Salama, P. J. Baker, H. F. Rodgers, V. Barynin, D. W. Rice, M. G. Hunter, *Antimicrob. Agents Chemother.* **2001,** *45,* 563–570.

[34] J. A. Sutcliffe, *Ann. N. Y. Acad. Sci.* **2011,** *1241,* 122–152.

[35] Q. Wang, J. Wang, Z. Cai, W. Xu, *Biophys. Chem.* **2008,** *134,* 178–184.

[36] T. R. Fritsche, H. S. Sader, R. Cleeland, R. N. Jones, *Antimicrob. Agents Chemother* **2005,** *49,* 1468–1476.

[37] M. Lee, D. Kim, J. Shin, H.–Y. Lee, S. Park, H.–S. Lee, J.–H. Kang, S.–J. Chung, *J. Pharm. Biomed. Anal.* **2017,** *145,* 364–371.

[38] C. Giglione, A. Serero, M. Pierre, B. Boisson, T. Meinnel, *EMBO J.* **2000,** *19,* 5916–5929.

[39] M. D. Lee, C. Antczak, Y. Li, F. M. Sirotnak, W. G. Bornmann, D. A. Scheinberg, *Mol. Biol. Rep.* **1994,** *19,* 183–194.

[40] H. J. Pel, L. A. Grivell, *Biochem. Biophys. Res. Commun.* **2003,** *312,* 309–315.

[41] S. Wicke, G. M. Schneeweiss, C. W. dePamphilis, K. F. Müller, D. Quandt, *Plant Mol. Biol.* **2011,** *76,* 273–297.

[42] S. Escobar–Alvarez, J. Gardner, A. Sheth, G. Manfredi, G. Yang, O. Ouerfelli, M. L. Heaney, D. A. Scheinberg, *Mol. Cell. Biol.* **2010,** *30,* 5099–5109.

[43] Y. Xu, L. T. Lai, J. L. Gabrilove, D. A. Scheinberg, *Clin. Cancer Res.* **1998,** *4,* 171–176.

[44] A. Sheth, S. Escobar–Alvarez, J. Gardner, L. Ran, M. L. Heaney, D. A. Scheinberg, *Cell Death Dis.* **2014,** *5,* e1152.

[45] S. Fieulaine, C. Juillan–Binard, A. Serero, F. Dardel, C. Giglione, T. Meinnel, J.–L. Ferrer, *J. Biol. Chem.* **2005,** *280,* 42315–42324.

[46] S. Escobar–Alvarez, Y. Goldgur, G. Yang, O. Ouerfelli, Y. Li, D. A. Scheinberg, *J. Mol. Biol.* **2009,** *387,* 1211–1228.

[47] K. T. Nguyen, X. Hu, C. Colton, R. Chakrabarti, M. X. Zhu, D. Pei, *Biochemistry* **2003,** *42,* 9952–9958.

[48] A. Serero, C. Giglione, A. Sardini, J. Martinez–Sanz, T. Meinnel, *J. Biol. Chem.* **2003,** *278,* 52953–52963.

[49] A. Boularot, C. Giglione, S. Petit, Y. Duroc, R. Alves de Sousa, V. Larue, T. Cresteil, F. Dardel, I. Artaud, T. Meinnel, *J. Med. Chem.* **2007,** *50,* 10–20.

[50] S. Petit, Y. Duroc, V. Larue, C. Giglione, C. Léon, C. Soulama, A. Denis, F. Dardel, T. Meinnel, I. Artaud, *ChemMedChem* **2009,** *4,* 261–275.

[51] E. Goemaere, A. Melet, V. Larue, A. Lieutaud, R. Alves de Sousa, J. Chevalier, L. Yimga-Djapa, C. Giglione, F. Huguet, M. Alimi, T. Meinnel, F. Dardel, I. Artaud, J.–M. Pagès, *J. Antimicrob. Chemother.* **2012,** *67,* 1392–1400.

[52] S. Fieulaine, R. Alves de Sousa, L. Maigre, K. Hamiche, M. Alimi, J.–M. Bolia, A. Taleb, A. Denis, J.–M. Pagès, I. Artaud, T. Meinnel, C. Giglione, *Sci. Rep.* **2016,** *6,* 35429.

[53] M. S. Butler, M. A. T. Blaskovich, M. A. Cooper, *J. Antibiot.* **2016,** *70,* 3–24.

[54] L. L. Silver, *Clin. Microbiol. Rev.* **2011,** *24,* 71–109.

[55] World Health Organization, *Antibacterial agents in clinical development: an analysis of the antibacterial clinical development pipeline, including tuberculosis;* Geneva, 2017.

[56] A. Thorarensen, M. Deibel, D. Rohrer, A. Vosters, A. Yem, V. Marshall, J. Lynn, M. Bohanon, P. Tomich, G. Zurenko, M. Sweeney, R. Jensen, J. Nielsen, E. Seest, L. Dolak, *Bioorg. Med. Chem. Lett.* **2001,** *11,* 1355–1358.

[57] C. Apfel, D. W. Banner, D. Bur, M. Dietz, C. Hubschwerlen, H. Locher, F. Marlin, R. Masciadri, W. Pirson, H. Stalder, *J. Med. Chem.* **2001,** *44,* 1847–1852.

[58] Y.–T. He, Y.–J. Mao, H.–Y. Hao, Z.–Y. Xu, S.–J. Lou, D.–Q. Xu, *Org. Lett.* **2020,** *22,* 8250–8255.

[59] I. N'Diaye, J. Mayrargue, C. C. Farnoux, M. Miocque, P. Gayral, *Eur. J. Med. Chem.* **1987,** *22,* 403–409.

[60] C. A. Brooks, L. S. Barton, D. J. Behm, H. S. Eidam, R. M. Fox, M. Hammond, T. H. Hoang, D. A. Holt, M. A. Hilfiker, B. G. Lawhorn, J. R. Patterson, P. Stoy, T. J. Roethke, G. Ye, S. Zhao, K. S. Thorneloe, K. B. Goodman, M. Cheung, *ACS Med. Chem. Lett.* **2019,** *10,* 1228–1233.

[61] L. Fabian, M. Taverna Porro, N. Gómez, M. Salvatori, G. Turk, D. Estrin, A. Moglioni, *Eur. J. Med. Chem.* **2020,** *188,* 111987.

[62] J. Pothier, M. A. Riederer, O. Peter, X. Leroy, A. Valdenaire, C. Gnerre, H. Fretz, *Bioorg. Med. Chem. Lett.* **2012,** *22,* 4660–4664.

[63] *Kirk–Othmer Food and Feed Technology, 2 Volume Set*; John Wiley & Sons: Hoboken, NJ, 2007.

[64] J. E. McMurry, *Organic Chemistry;* Brooks/Cole Cengage Learning: International ed., 8th ed.; 2012.

[65] K. T. Hylland, S. Øien–Ødegaard, M. Tilset, *Eur. J. Org. Chem.* **2020,** 4208–4226.

[66] J. Clayden, N. Greeves, S. Warren, P. Wothers, *Organic Chemistry;* Oxford University Press: Oxford, 1st ed.; 2001.

[67] M. Witanowski, L. Stefaniak, G. Webb, Nitrogen NMR Spectroscopy. In *Annual Reports on NMR Spectroscopy*, Vol. 11; Academic Press: Cambridge, MA, 1982.

[68] D. Li, T. Ollevier, *Eur. J. Org. Chem.* **2019,** 1273–1280.

[69] E. Folkertsma, E. F. de Waard, G. Korpershoek, A. J. van Schaik, N. Solozabal Mirón, M. Borrmann, S. Nijsse, M. A. H. Moelands, M. Lutz, M. Otte, M.-E. Moret, R. J. M. Klein Gebbink, *Eur. J. Inorg. Chem.* **2016,** 1319–1332.

[70] V. Pandarus, R. Ciriminna, F. Béland, M. Pagliaro, *Adv. Synth. Catal.* **2011,** *353,* 1306–1316.

[71] L. Hizartzidis, P. J. Cossar, M. J. Robertson, M. I. Simone, K. A. Young, A. McCluskey, C. P. Gordon, *RSC Adv.* **2014,** *4,* 56743–56748.

[72] A. Kallinen, R. Boyd, S. Lane, R. Bhalla, K. Mardon, D. H. R. Stimson, E. L. Werry, R. Fulton, M. Connor, M. Kassiou, *Org. Biomol. Chem.* **2019,** *17,* 5086–5098.

[73] P. Furet, M. Gerspacher, C. Pissot–Soldermann, *Bioorg. Med. Chem. Lett.* **2010,** *20,* 1858–1860.

[74] C. Wang, D. Xing, D. Wang, X. Wu, W. Hu, *J. Org. Chem.* **2014,** *79,* 3908–3916.

[75] A. D. Martin, J. P. Wojciechowski, M. M. Bhadbhade, P. Thordarson, *Langmuir* **2016,** *32,* 2245–2250.

[76] N. Abe, N. Ishikawa, T. Hayashi, Y. Miura, *Bull. Chem. Soc. Jpn.* **1990,** *63,* 1617–1622.

[77] A. Chan, K. A. Scheidt, *J. Am. Chem. Soc.* **2007,** *129,* 5334–5335.

[78] W. P. Jencks, J. Carriuolo, *J. Am. Chem. Soc.* **1960,** *82,* 1778–1786.

[79] C. D. Floyd, C. N. Lewis, S. R. Patel, M. Whittaker, *Tet. Lett.* **1996,** *37,* 8045–8048.

[80] J. S. Albert, A. D. Hamilton, A. C. Hart, X. Feng, L. Lin, Z. Wang, 1,3–Dicyclohexylcarbodiimide. In *Encyclopedia of Reagents for Organic Synthesis*; John Wiley & Sons: Hoboken, NJ, 2017.

[81] Y. Wang, Y. Wu, Y. Li, Y. Tang, *Chem. Sci.* **2017,** *8,* 3852–3857.

[82] C. Karvellas, C. Williams, M. Whitehead, B. Jean–Claude, *J. Mol. Struct. THEOCHEM* **2001,** *535,* 199–215.

[83] S. Yoshida, T. Nonaka, T. Morita, T. Hosoya, *Org. Biomol. Chem.* **2014,** *12,* 7489–7493.

[84] S. Azeez, P. Chaudhary, P. Sureshbabu, S. Sabiah, J. Kandasamy, *Org. Biomol. Chem.* **2018,** *16,* 8280–8285.

[85] Y. Yang, A. Qin, K. Zhao, D. Wang, X. Shi, *Adv. Synth. Catal.* **2016,** *358,* 1433–1439.

[86] J. Messeguer, I. Masip, M. Montolio, J. A. del Rio, E. Soriano, A. Messeguer, *Tetrahedron* **2010,** *66,* 2444–2454.

[87] A. S. Felts, C. Ji, J. B. Stafford, B. C. Crews, P. J. Kingsley, C. A. Rouzer, M. K. Washington, K. Subbaramaiah, B. S. Siegel, S. M. Young, A. J. Dannenberg, L. J. Marnett, *ACS Chem. Biol.* **2007,** *2,* 479–483.

[88] K. Nishikawa, H. Fukuda, M. Abe, K. Nakanishi, Y. Tazawa, C. Yamaguchi, S. Hiradate, Y. Fujii, K. Okuda, M. Shindo, *Phytochemistry* **2013,** *96,* 223–234.

[89] E. Alcalde, N. Mesquida, J. Frigola, S. López–Pérez, R. Mercè, *Org. Biomol. Chem.* **2008,** *6,* 3795–3810.

[90] E. Alcalde, N. Mesquida, S. López–Pérez, J. Frigola, R. Mercè, *J. Med. Chem.* **2009,** *52,* 675–687.

[91] T. Guney, T. A. Wenderski, M. W. Boudreau, D. S. Tan, *Chem. Eur. J.* **2018,** *24,* 13150–13157.

[92] D. L. Musso, G. F. Orr, F. R. Cochran, J. L. Kelley, J. L. Selph, G. C. Rigdon, B. R. Cooper, M. L. Jones, *J. Med. Chem.* **2003,** *46,* 409–416.

[93] H. J. Reich, Pople Nomenclature for Coupled Spin Systems. In *Hans Reich's Collection. NMR Spectroscopy*; University of Wisconsin–Madison: Madison, WI, 2017 `https://organicchemistrydata.org/hansreich/` (Accessed: May 6th, 2021).

[94] I. B. Tangevold, *Synthesis of predecessors of novel PDF inhibitors with indane and tetralin scaffolds*, B.Sc. Project, University of Oslo, 2021.

[95] S. Basurto, S. García, A. G. Neo, T. Torroba, C. F. Marcos, D. Miguel, J. Barberá, M. B. Ros, M. R. de la Fuente, *Chem. Eur. J.* **2005,** *11,* 5362–5376.

[96] Z.–G. Wang, L. Chen, J. Chen, J.–F. Zheng, W. Gao, Z. Zeng, H. Zhou, X. Zhang, P.–Q. Huang, Y. Su, *Eur. J. Med. Chem.* **2013,** *62,* 632–648.

[97] M. Zhang, L. Zhu, X. Ma, M. Dai, D. Lowe, *Org. Lett.* **2003,** *5,* 1587–1589.

[98] I. K. Faye–Schjøll, *Structural and functional studies of the inhibition of peptide deformylase – A potential antibiotic target*, M.Sc. Thesis, University of Oslo, 2021.

[99] I. Singh, O. Seitz, *Org. Lett.* **2006,** *8,* 4319–4322.

[100] M. A. Khan, K. Miller, K. D. Rainsford, Y. Zhou, *Molecules* **2013,** *18,* 3227–3240.

[101] M. S. C. Pedras, D. P. O. Okinyo, *Org. Biomol. Chem.* **2008,** *6,* 51–54.

[102] D. Ranganathan, C. Bhushan Rao, S. Ranganathan, A. K. Mehrotra, R. Iyengar, *J. Org. Chem.* **1980,** *45,* 1185–1189.

[103] G. R. Fulmer, A. J. M. Miller, N. H. Sherden, H. E. Gottlieb, A. Nudelman, B. M. Stoltz, J. E. Bercaw, K. I. Goldberg, *Organometallics* **2010,** *29,* 2176–2179.

[104] *Sigma–Aldrich*, IR Spectrum Table & Chart; `https://sigmaaldrich.com` (Accessed: May 3rd, 2021).

[105] K. J. Morgan, *J. Chem. Soc.* **1961,** 2343–2347.

[106] A. Suwaiyan, R. Zwarich, N. Baig, *J. Raman Spectrosc.* **1990,** *21,* 243–249.

[107] *Spectral Database for Organic Compounds (SDBS)*; infrared spectrum; SDBS No.: 53563; CAS RN 4887–88–1; `sdbs.db.aist.go.jp` (Accessed: May 3rd, 2021).

[108] A. Bigotto, A. N. Pandey, C. Zerbo, *Spectrosc. Lett.* **1996,** *29,* 511–522.

[109] *Spectral Database for Organic Compounds (SDBS)*; infrared spectrum; SDBS No.: 10018; CAS RN 94–97–3; `sdbs.db.aist.go.jp` (Accessed: May 3rd, 2021).

Appendix

The following appendix contains supplementary spectroscopic data aquired for this thesis. It is divided into six sections, where those spectra discussed in Chapter 3 are located in Section A. Subsequent sections contain two–dimensional NMR data used for assignment of ^{1}H and ^{13}C resonances, going by Routes I–V in order.

A. NMR spectra discussed in Chapter 3

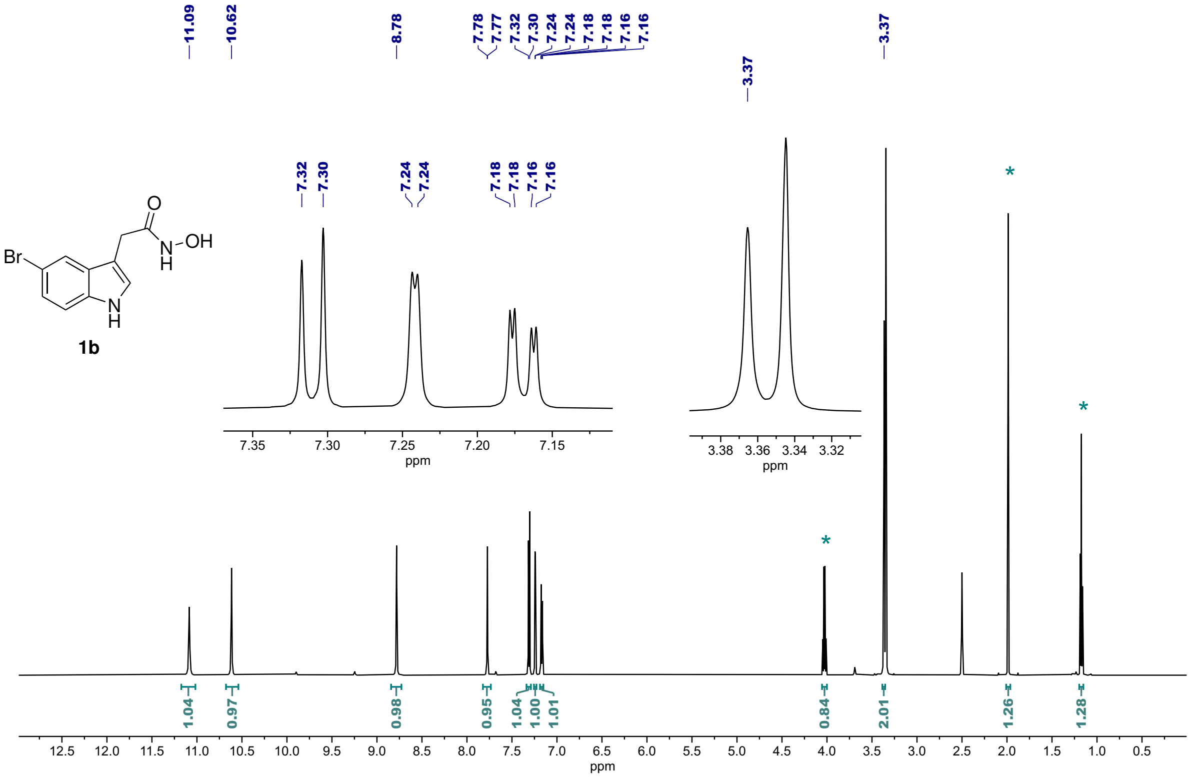

1b

Figure A1: ^{1}H NMR (600 MHz, DMSO–d$_6$) spectrum of **1b** with ethyl acetate signals integrated for comparison. Signals from ethyl acetate are marked with teal asterisks.

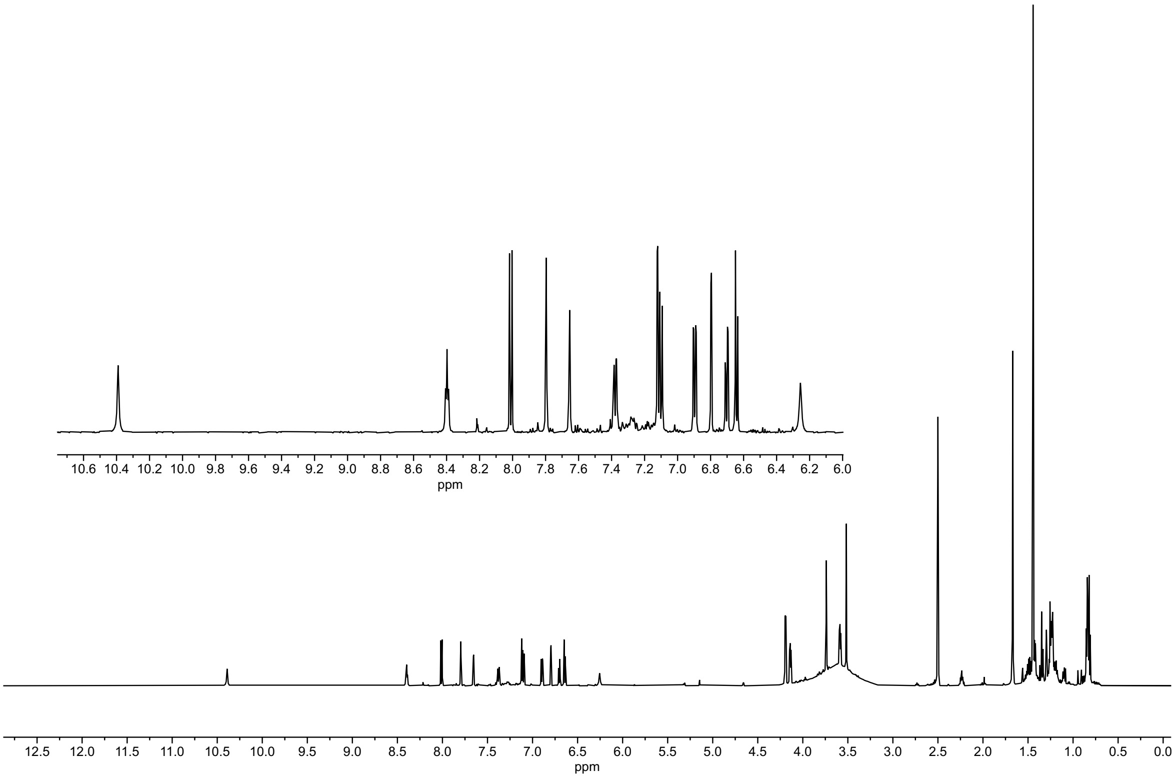

Figure A2: ^{1}H NMR (600 MHz, DMSO–d$_6$) spectrum of the crude material from the reaction in Scheme 3.4, including leftovers of **2b**. The signal at 10.39 ppm stood out as an unexpected signal from an exchangable hydrogen.

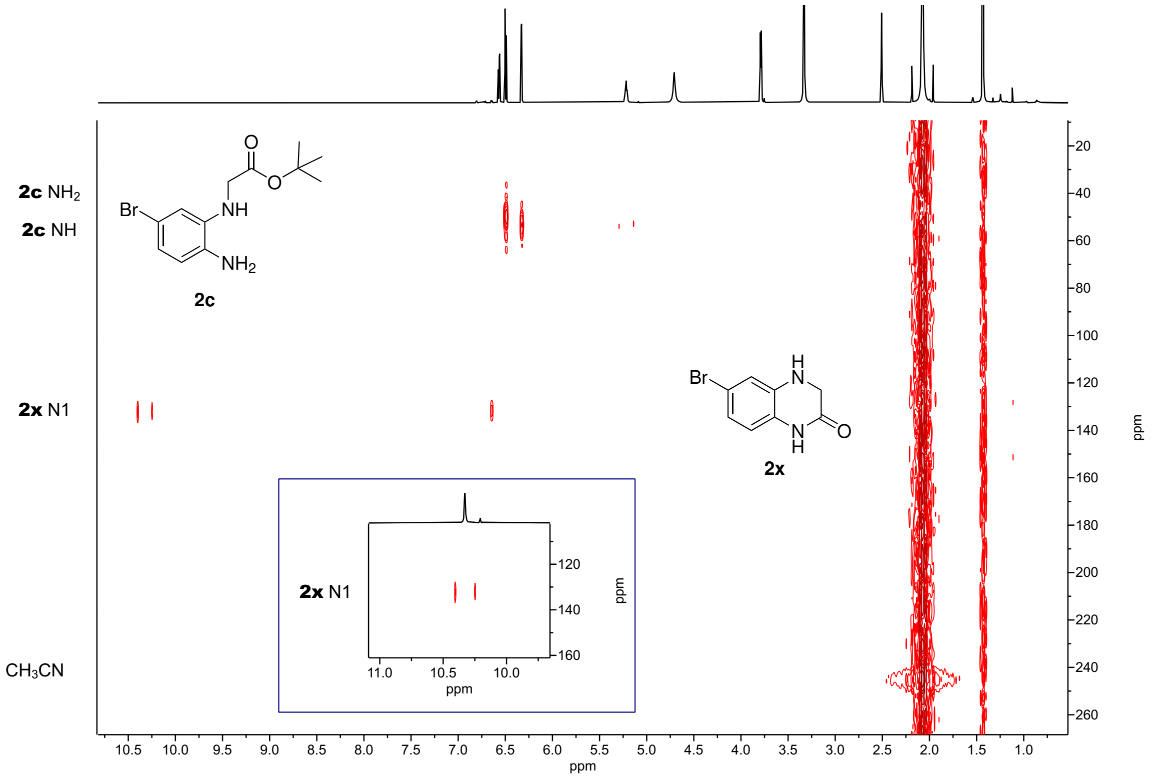

Figure A3: ^{1}H–^{15}N HMBC (600 MHz, DMSO–d$_6$) spectrum of **2c** with traces of **2x** present. CH_3CN is used as an internal standard. The ^{15}N correlations at 129.9 ppm show that the ^{1}H signal at 10.39 ppm comes from the hydrogen of an amide.

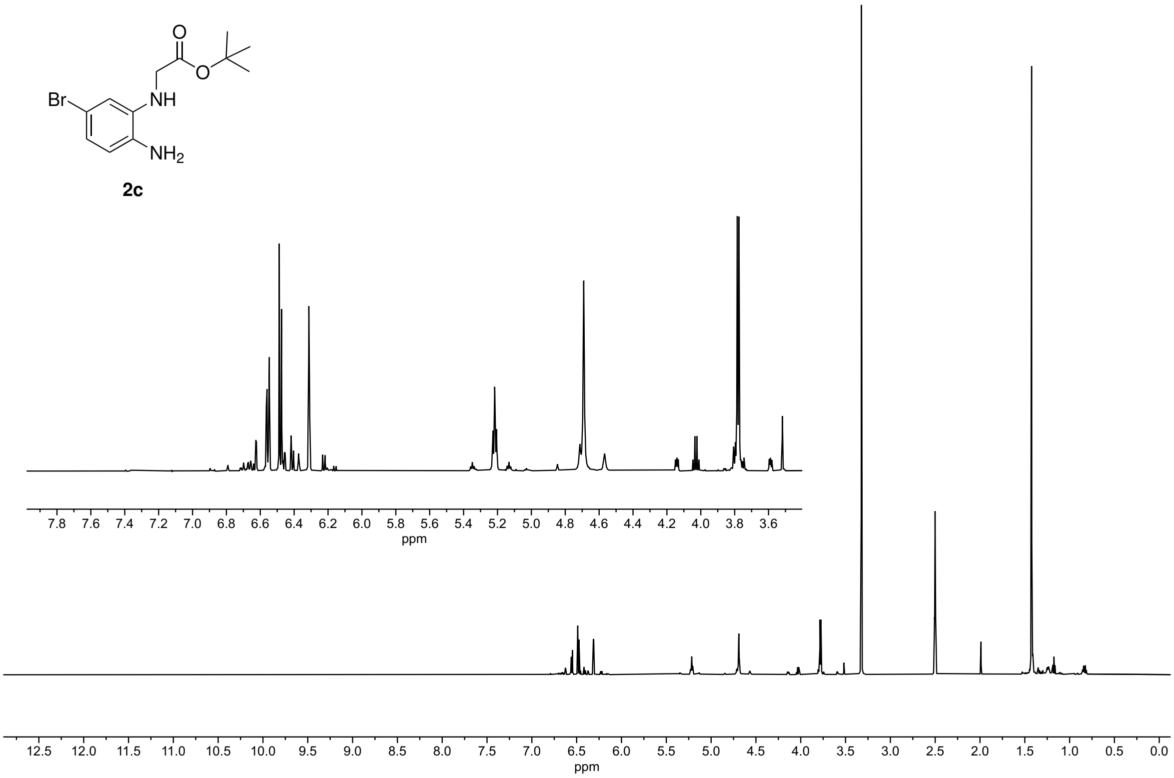

Figure A4: ^{1}H NMR (600 MHz, DMSO–d$_6$) spectrum of the crude material from the reaction in Scheme 3.8, showing **2c** as the major species.

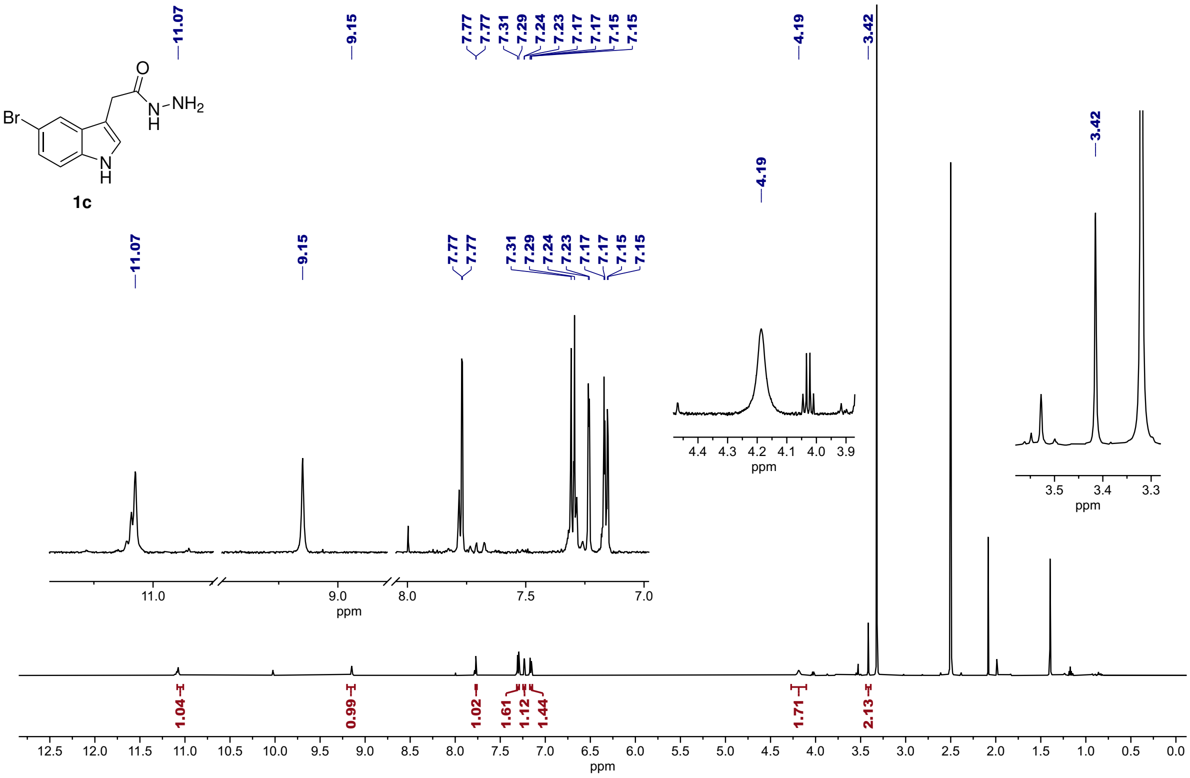

Figure A5: ^{1}H NMR (600 MHz, DMSO–d$_6$) spectrum of crude **1c**. Signals marked with integrals and chemical shifts arise from the target molecule.

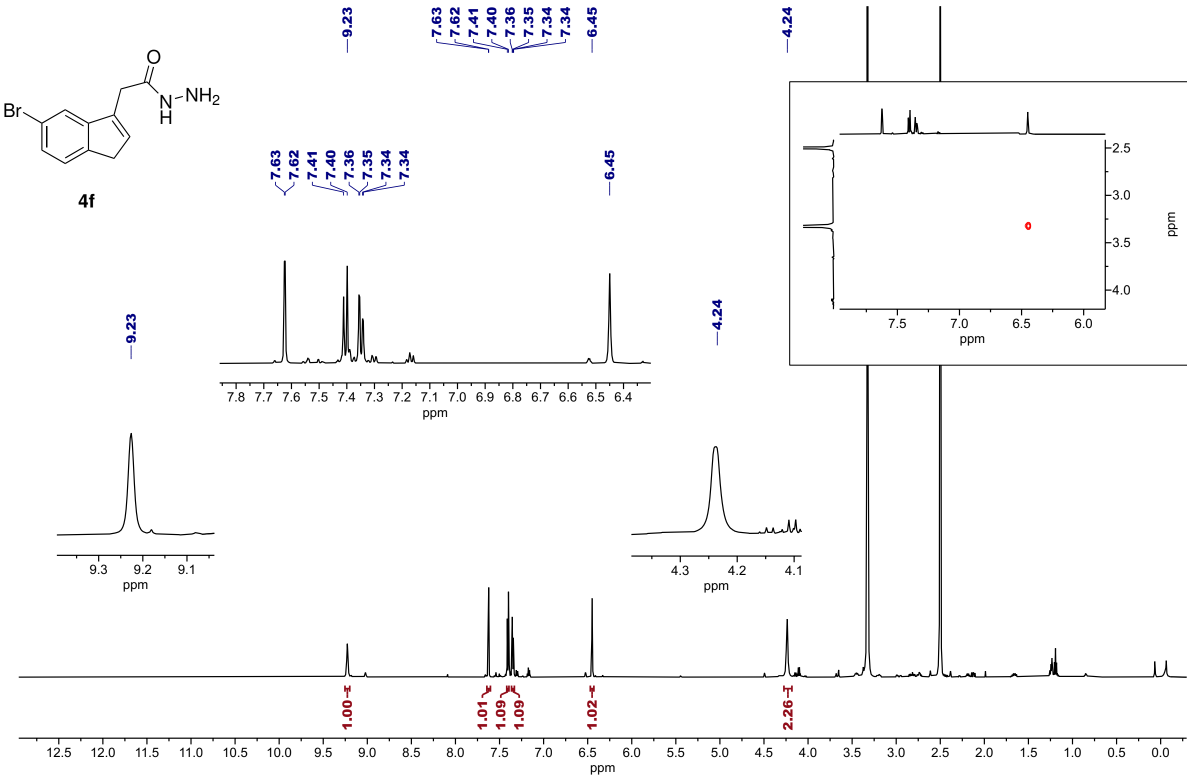

Figure A6: ^{1}H NMR (600 MHz, DMSO–d$_6$) spectrum of crude **4f**. Signals marked with integrals and chemical shifts arise from the target molecule. Inset of COSY spectrum, showing two signals hidden beneath the water signal at 3.33 ppm

B. NMR spectra of compounds from Route I

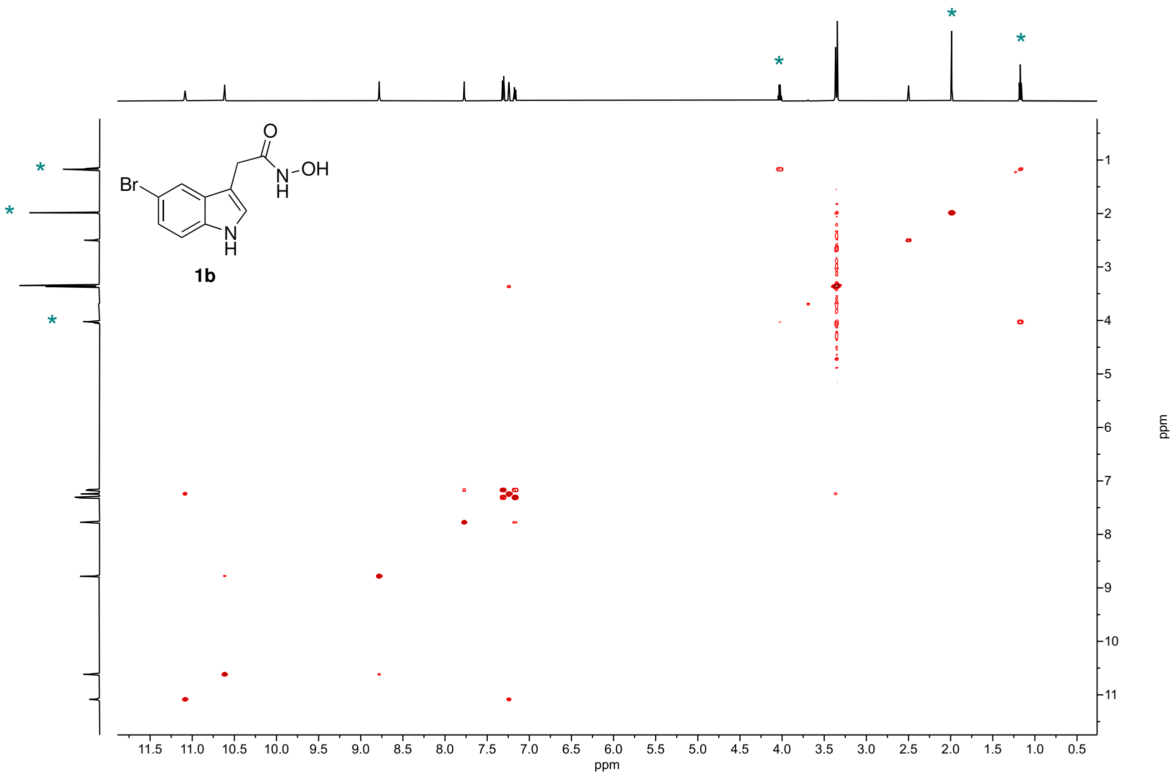

Figure B1: COSY (600 MHz, DMSO–d$_6$) spectrum of **1b**.
Signals from ethyl acetate are marked with teal asterisks.

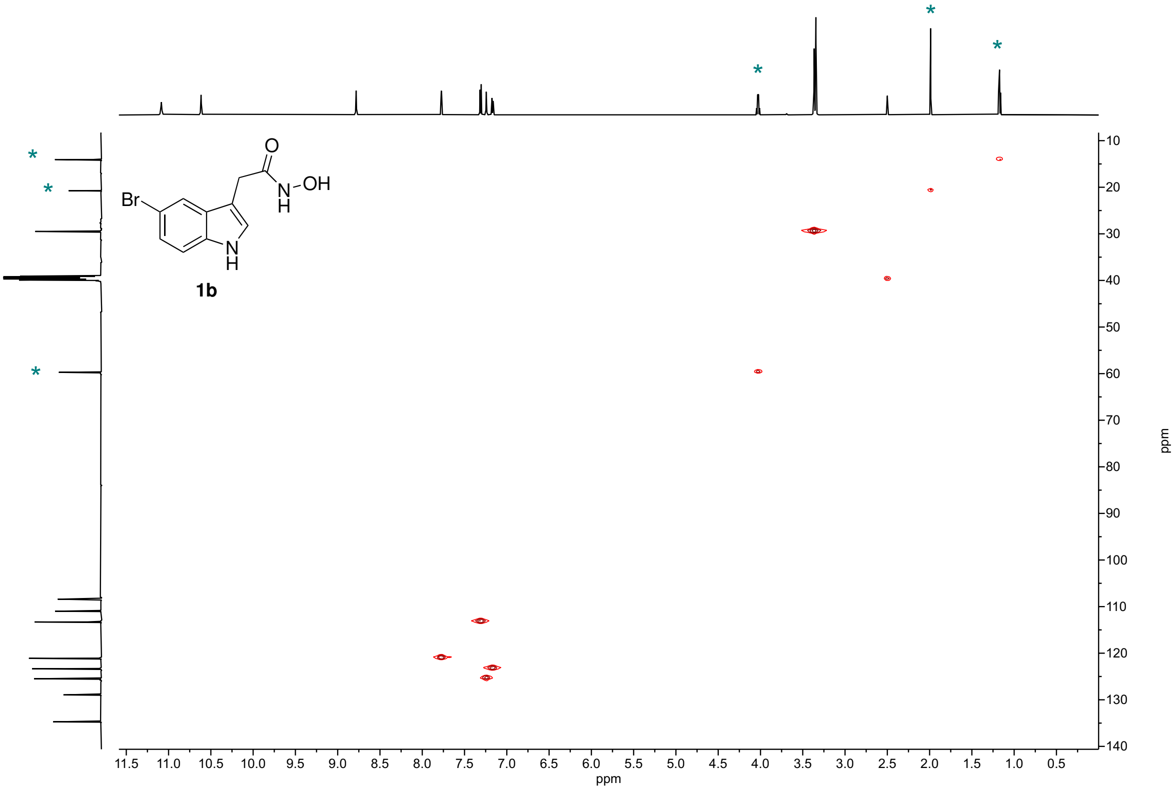

Figure B2: HSQC (600 MHz, DMSO–d_6) spectrum of **1b**.
Signals from ethyl acetate are marked with teal asterisks.

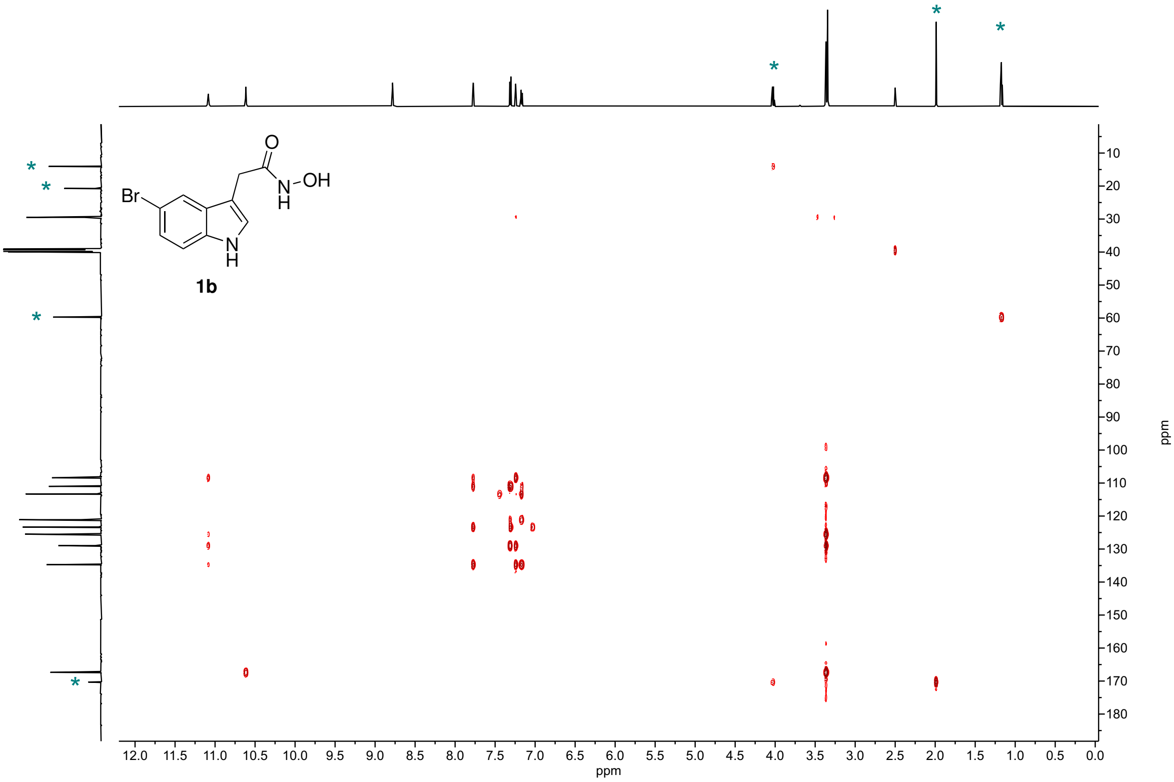

Figure B3: HMBC (600 MHz, DMSO–d_6) spectrum of **1b**.
Signals from ethyl acetate are marked with teal asterisks.

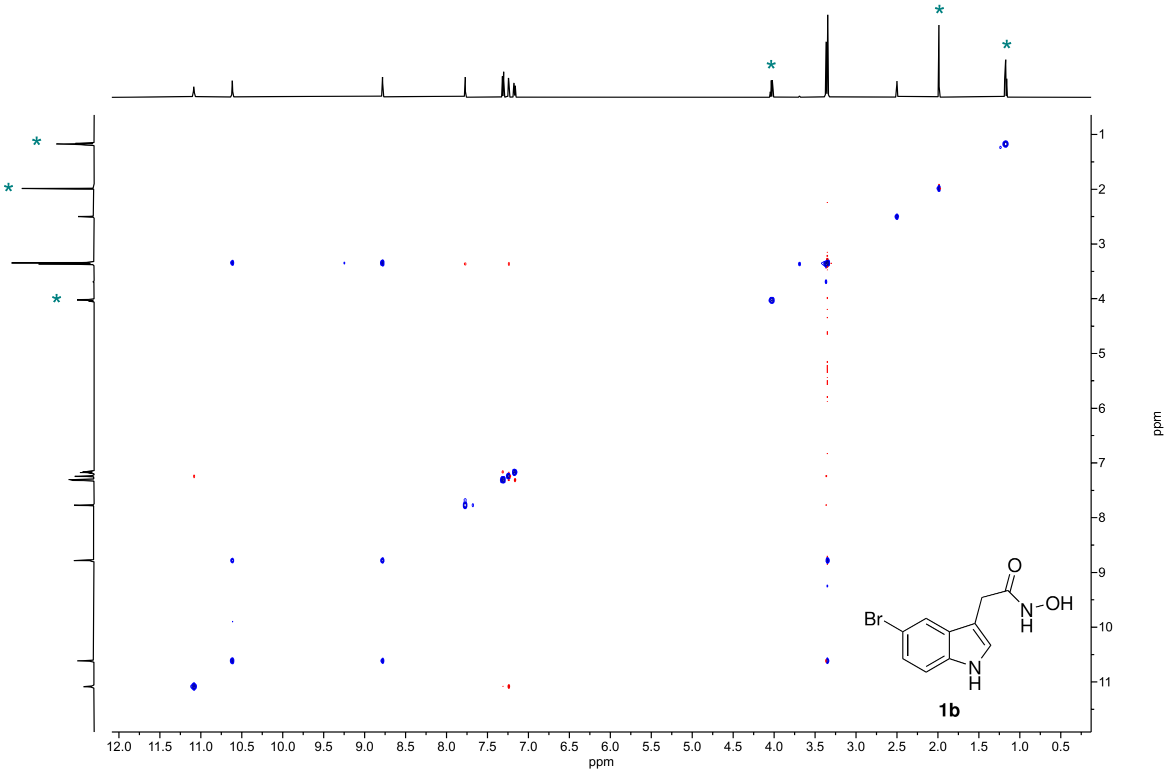

Figure B4: NOESY (600 MHz, DMSO–d_6) spectrum of **1b**. Signals from ethyl acetate are marked with teal asterisks.

C. NMR spectra of compounds from Route II

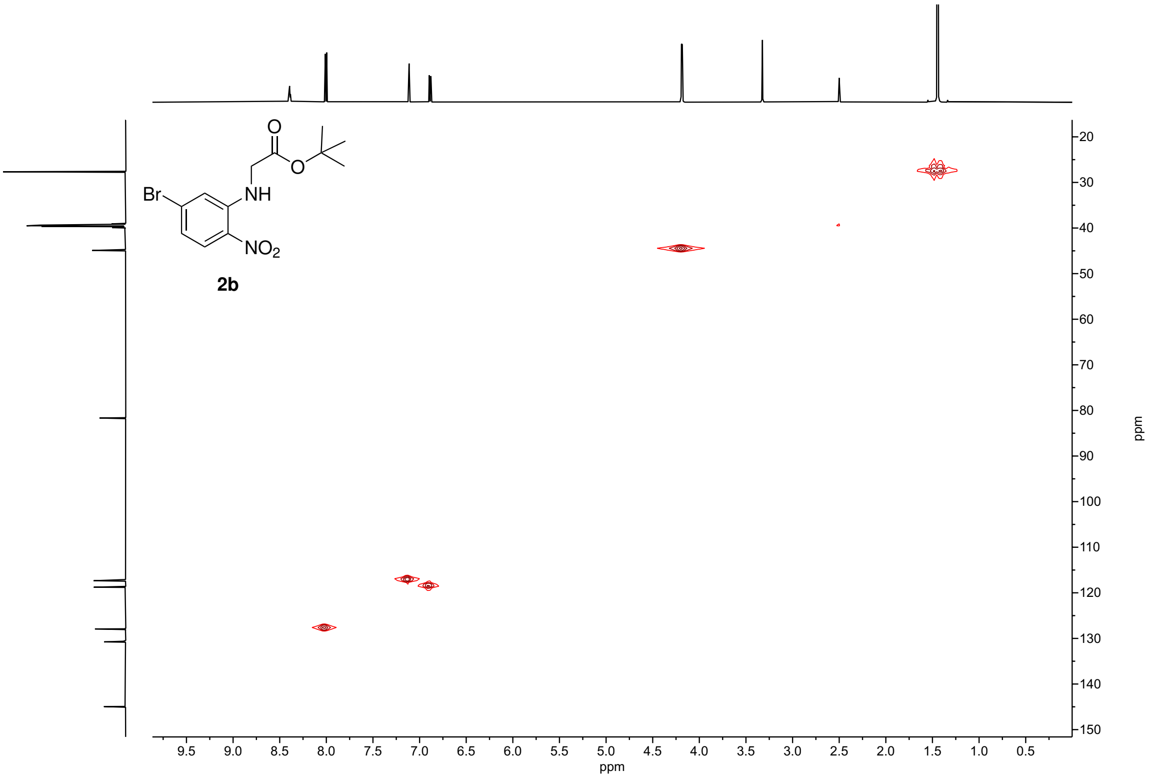

Figure C1: HSQC (600 MHz, DMSO–d_6) spectrum of **2b**.

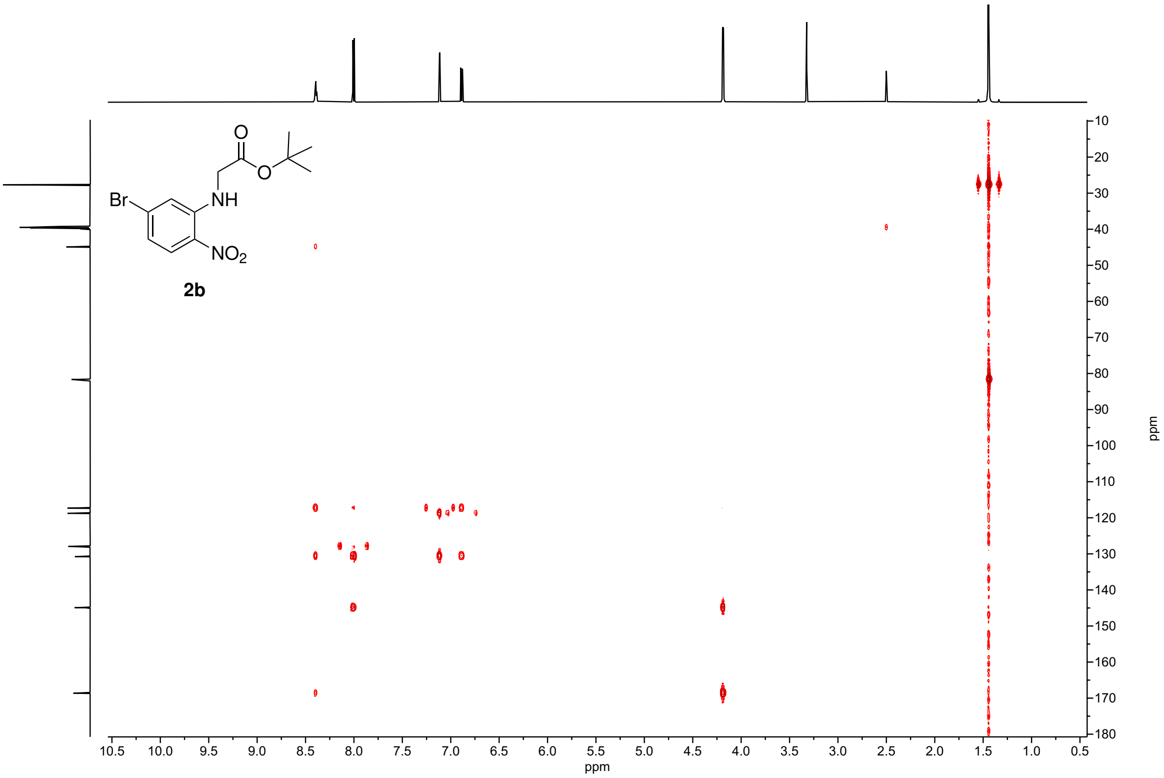

Figure C2: HMBC (600 MHz, DMSO–d_6) spectrum of **2b**.

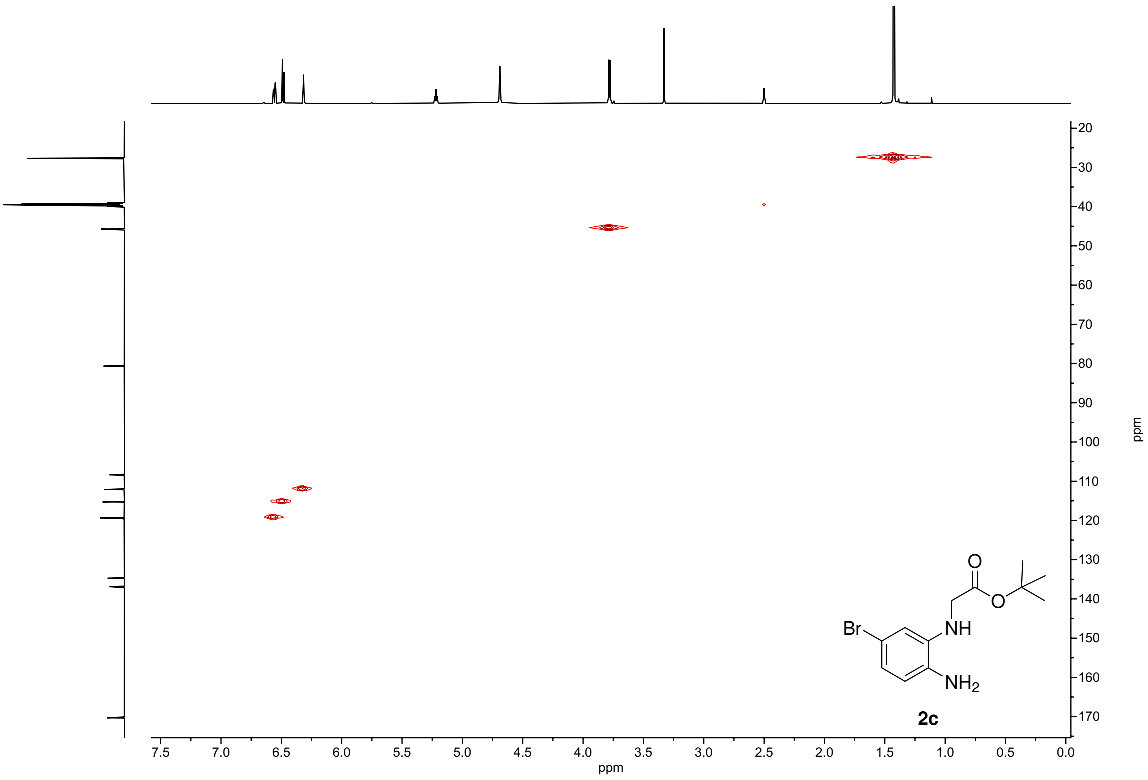

Figure C3: HSQC (600 MHz, DMSO–d_6) spectrum of **2c**.

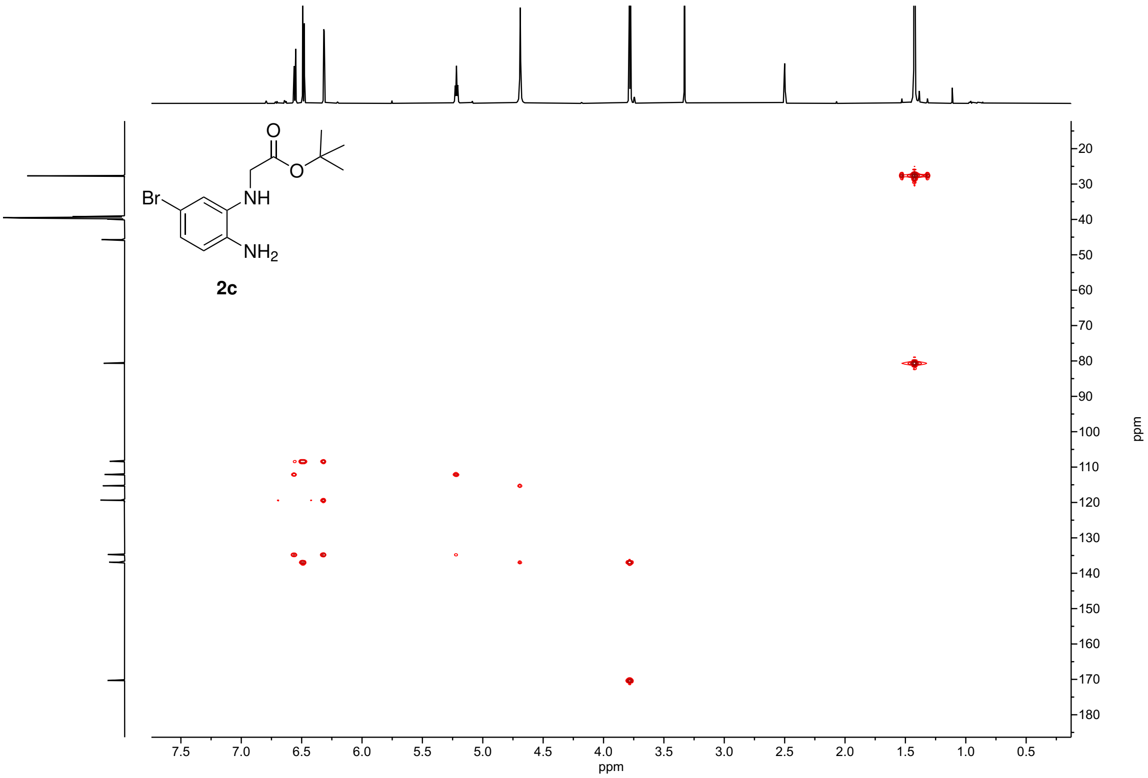

Figure C4: HMBC (600 MHz, DMSO–d_6) spectrum of **2c**.

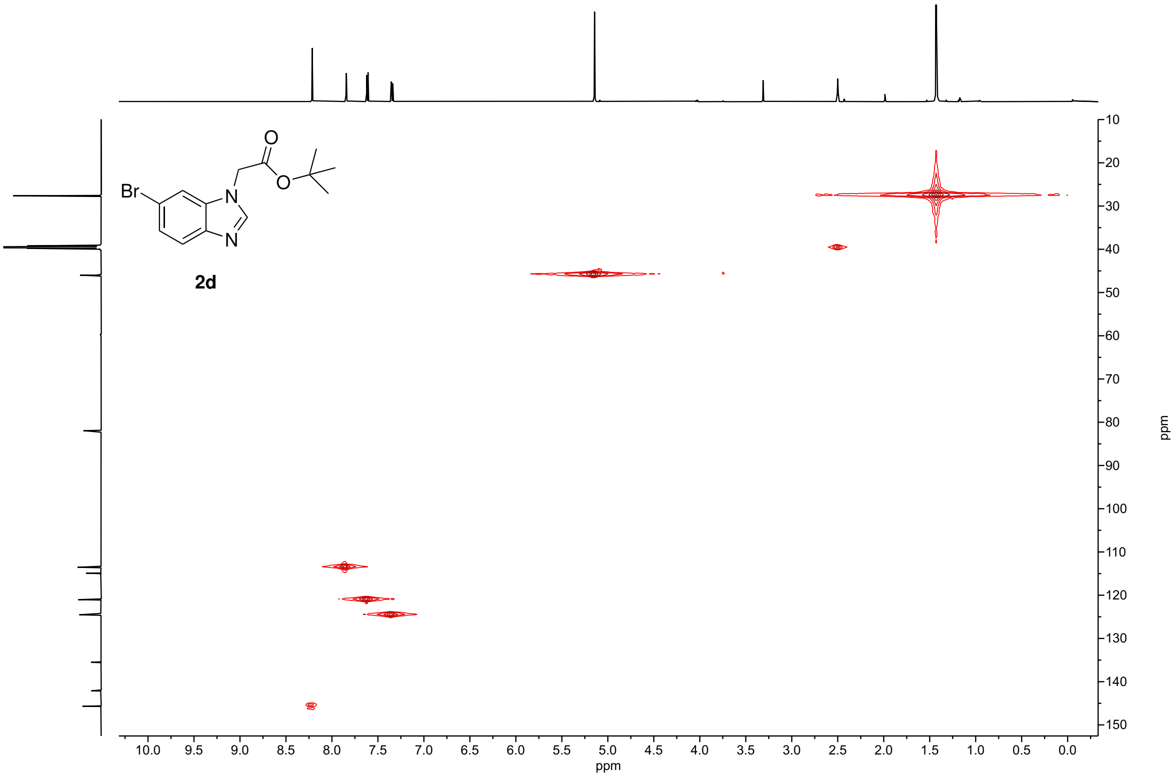

Figure C5: HSQC (600 MHz, DMSO–d_6) spectrum of **2d**.

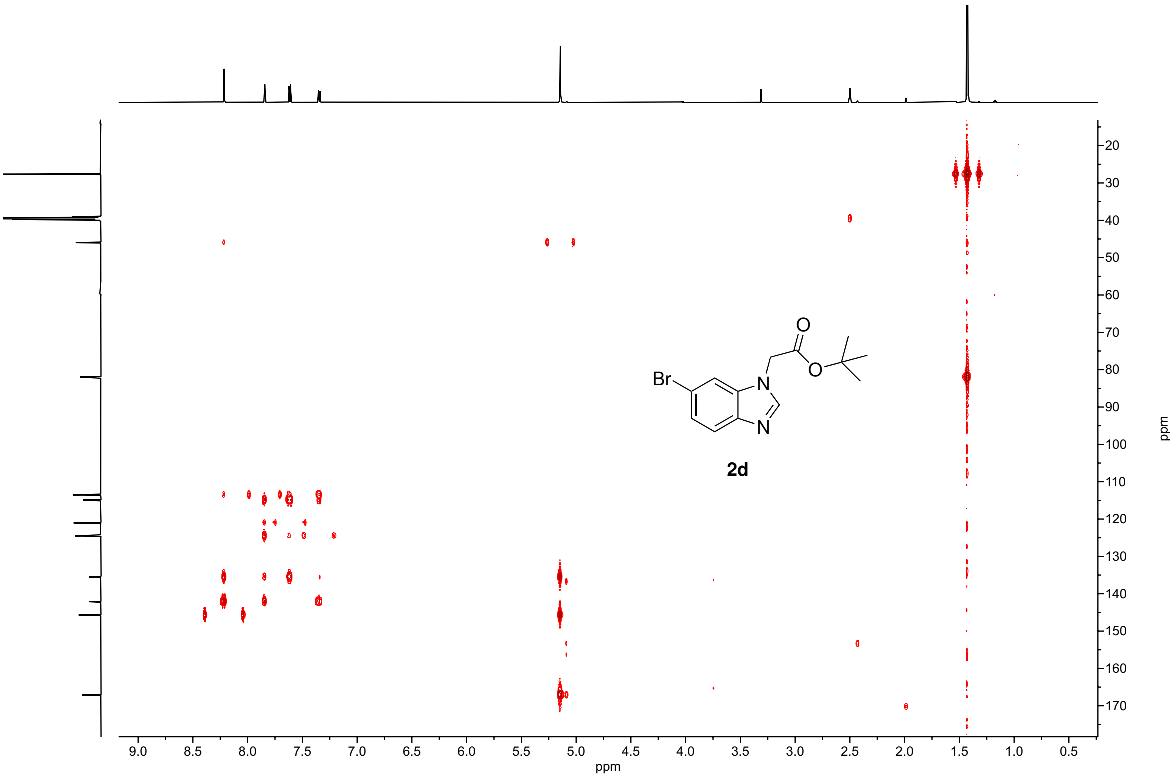

Figure C6: HMBC (600 MHz, DMSO–d_6) spectrum of **2d**.

D. NMR spectra of compounds from Route III

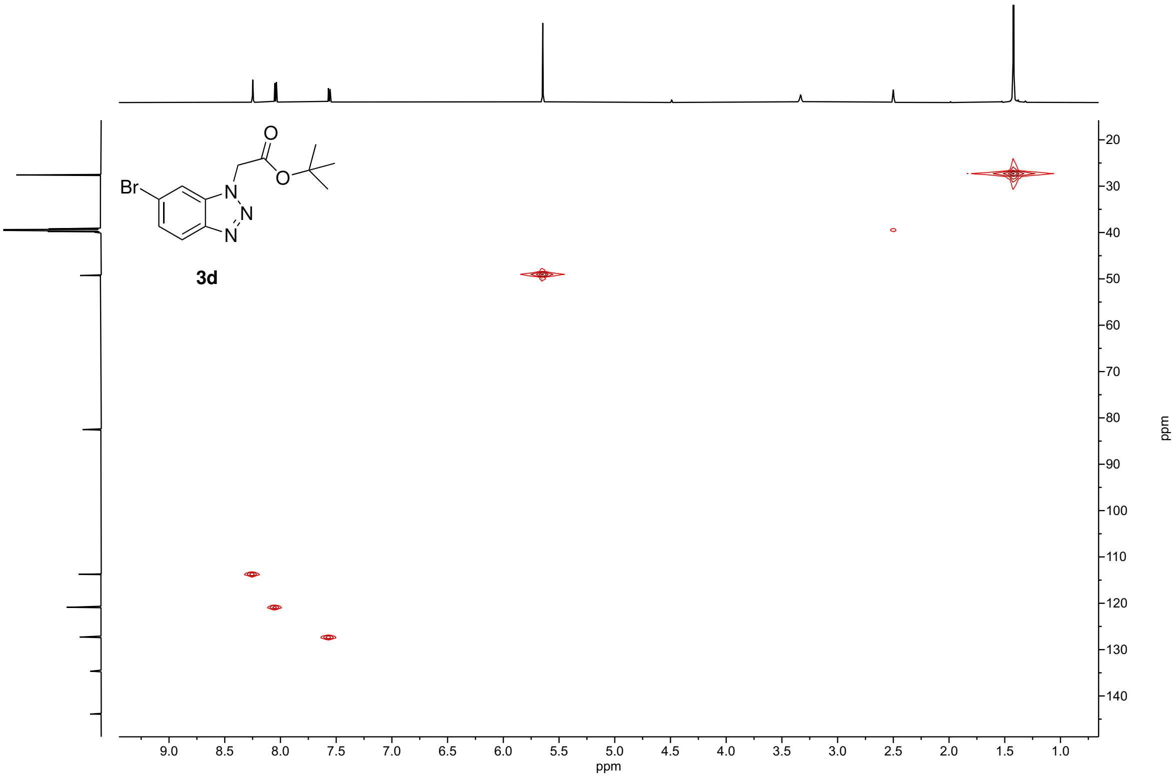

Figure D1: HSQC (600 MHz, DMSO–d_6) spectrum of **3d**.

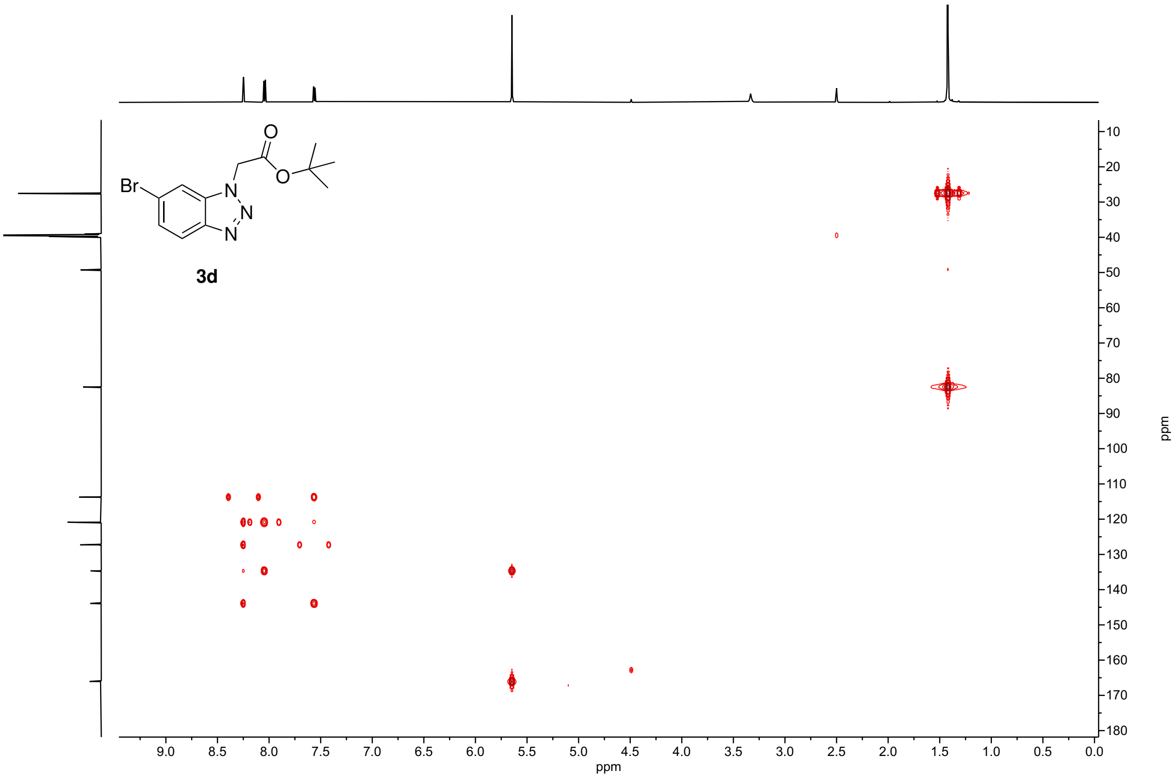

Figure D2: HMBC (600 MHz, DMSO–d_6) spectrum of **3d**.

E. NMR spectra of compounds from Route IV

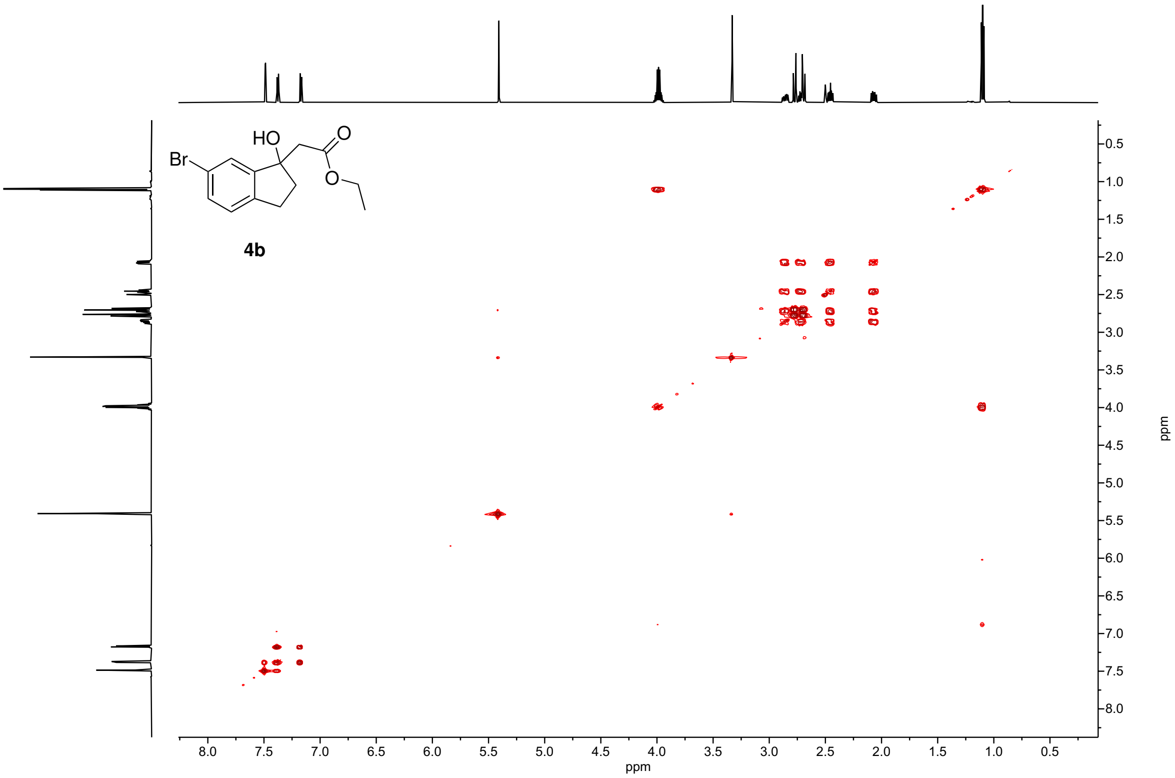

Figure E1: COSY (600 MHz, DMSO–d$_6$) spectrum of **4b**.

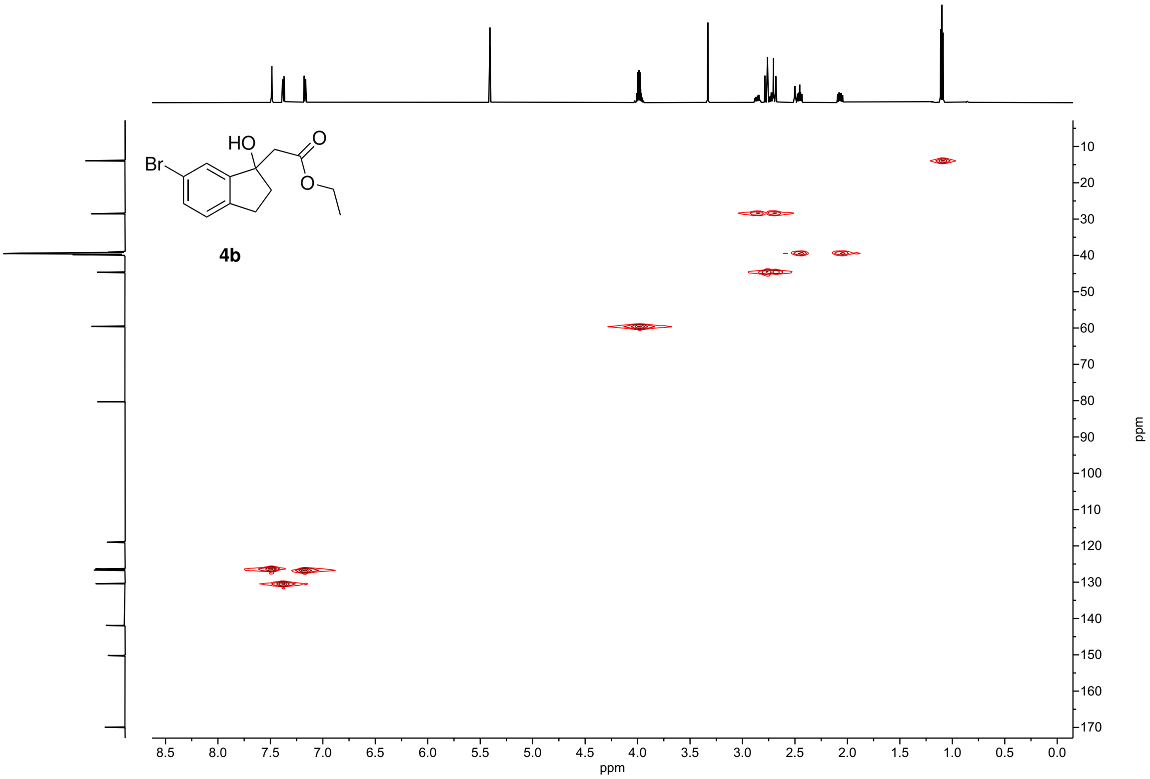

Figure E2: HSQC (600 MHz, DMSO–d$_6$) spectrum of **4b**.

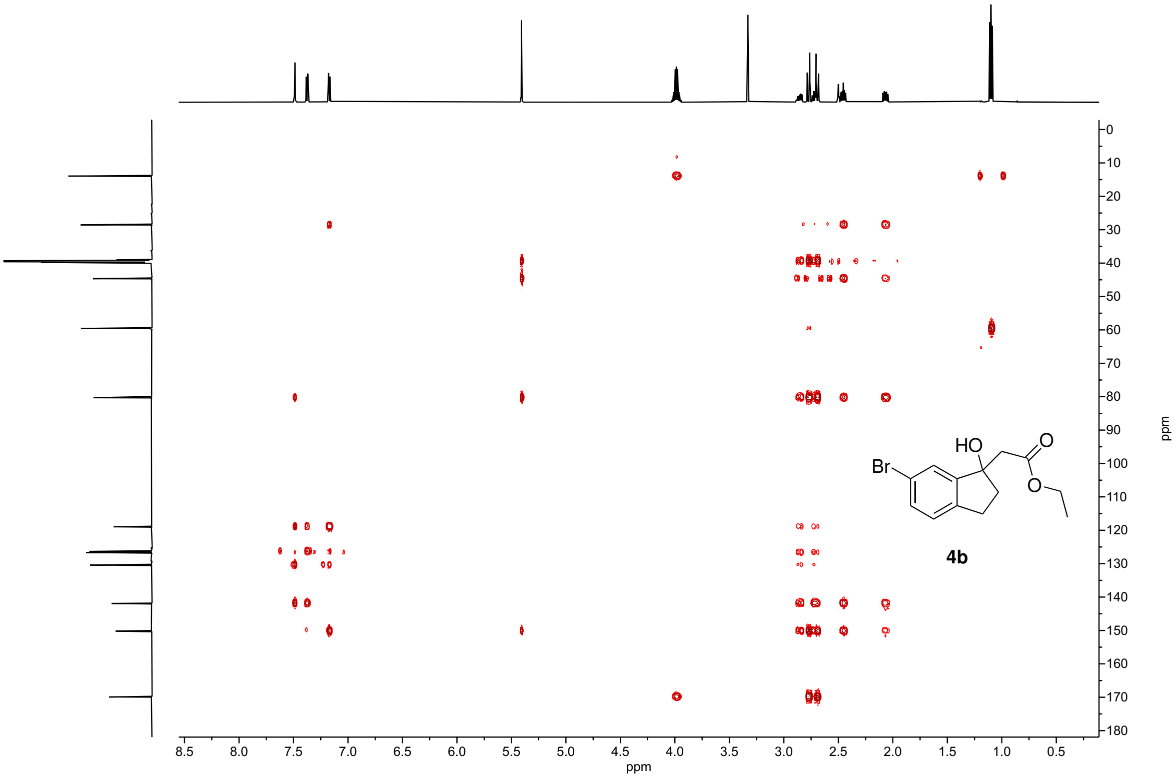

Figure E3: HMBC (600 MHz, DMSO–d_6) spectrum of **4b**.

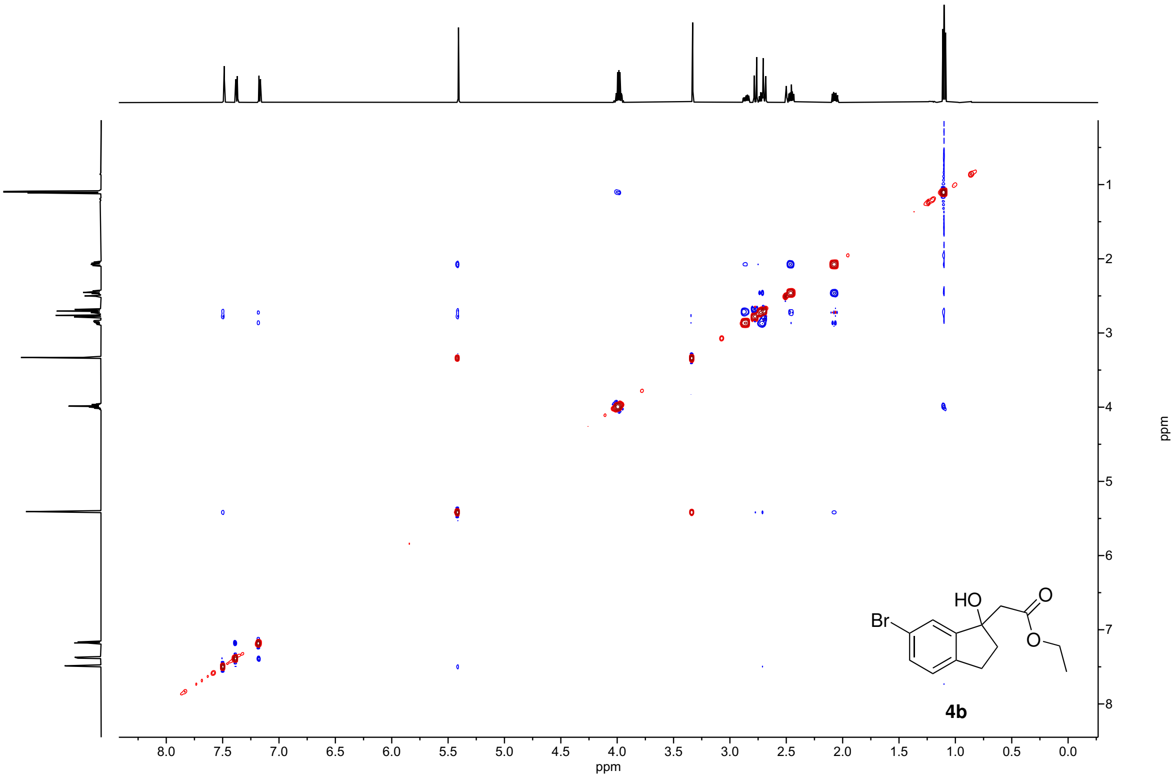

Figure E4: NOESY (600 MHz, DMSO–d_6) spectrum of **4b**.

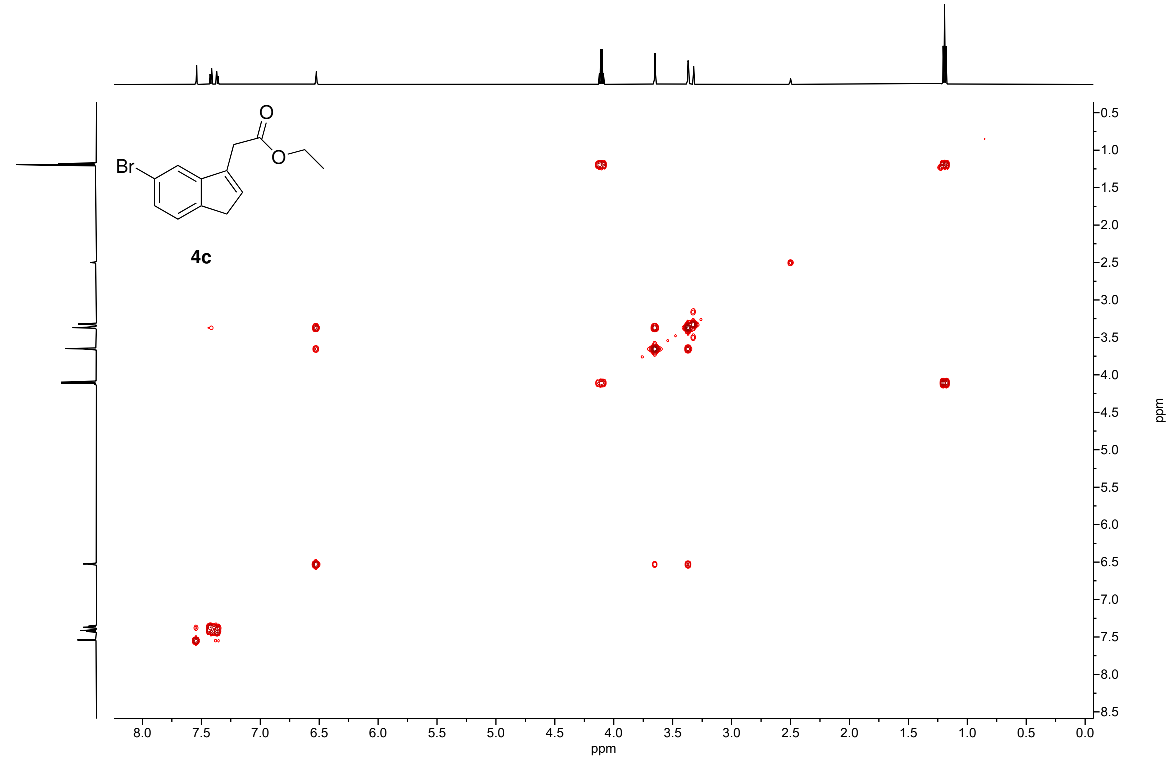

Figure E5: COSY (600 MHz, DMSO–d_6) spectrum of **4c**.

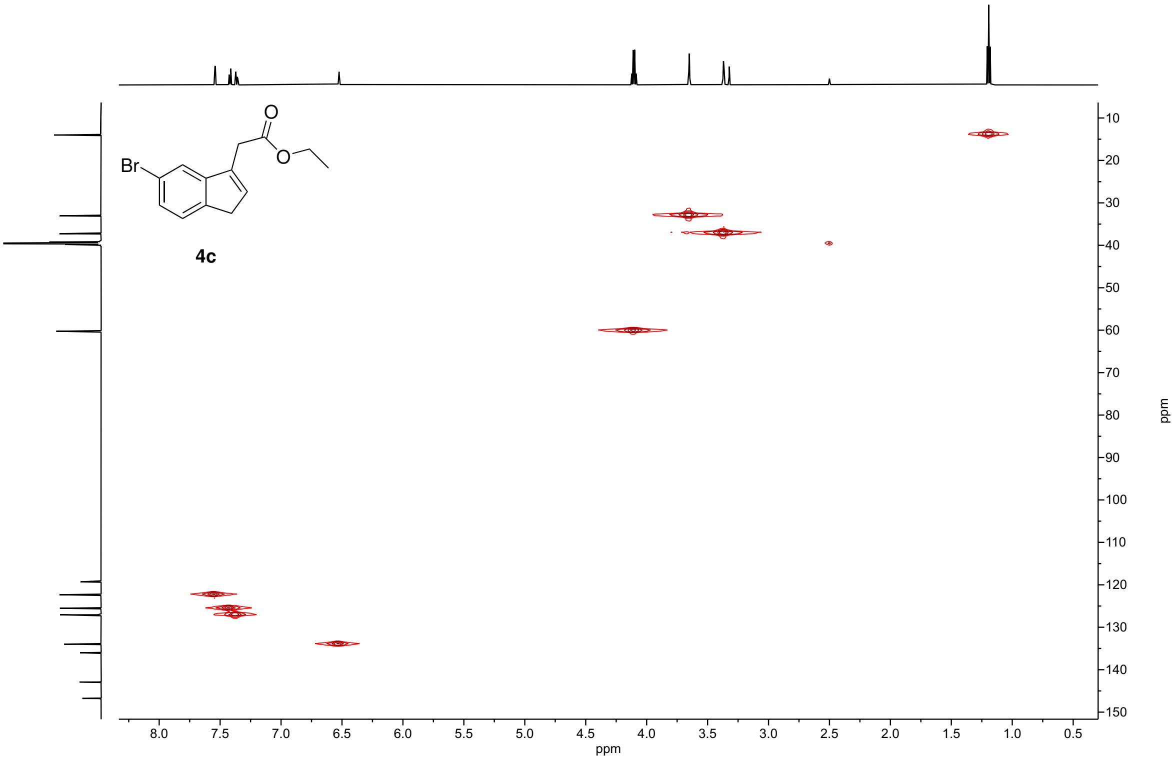

Figure E6: HSQC (600 MHz, DMSO–d_6) spectrum of **4c**.

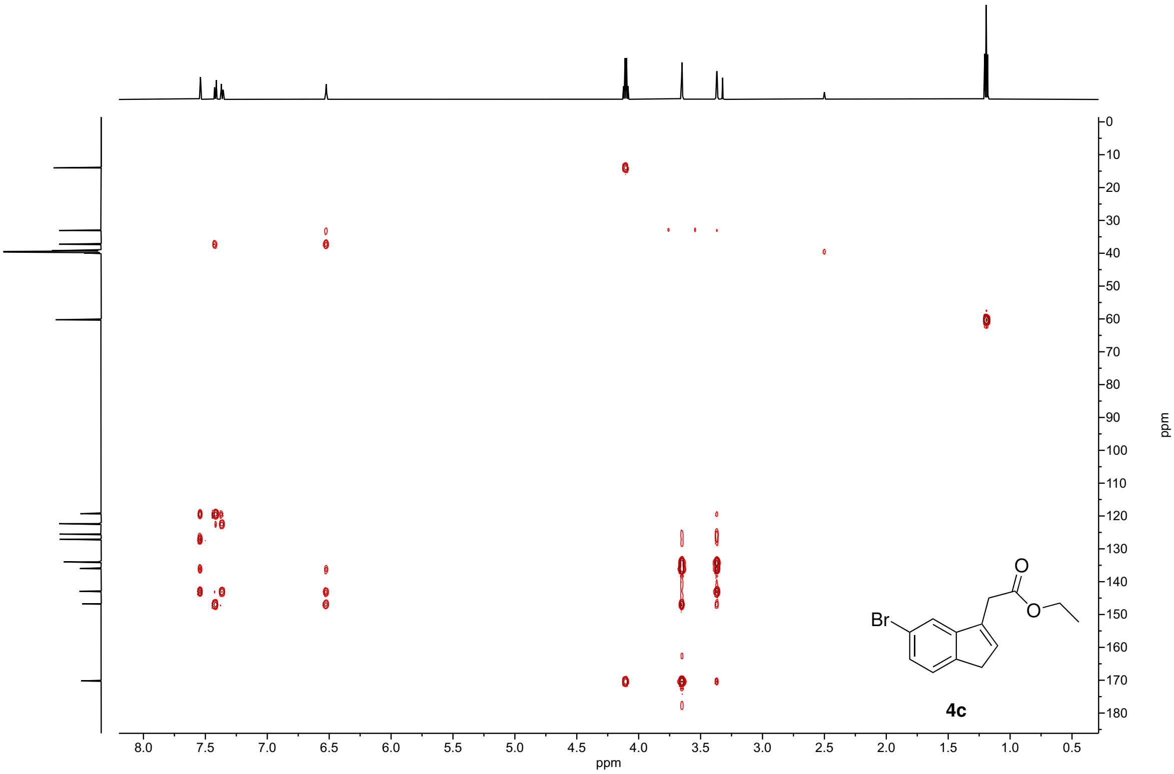

Figure E7: HMBC (600 MHz, DMSO–d$_6$) spectrum of **4c**.

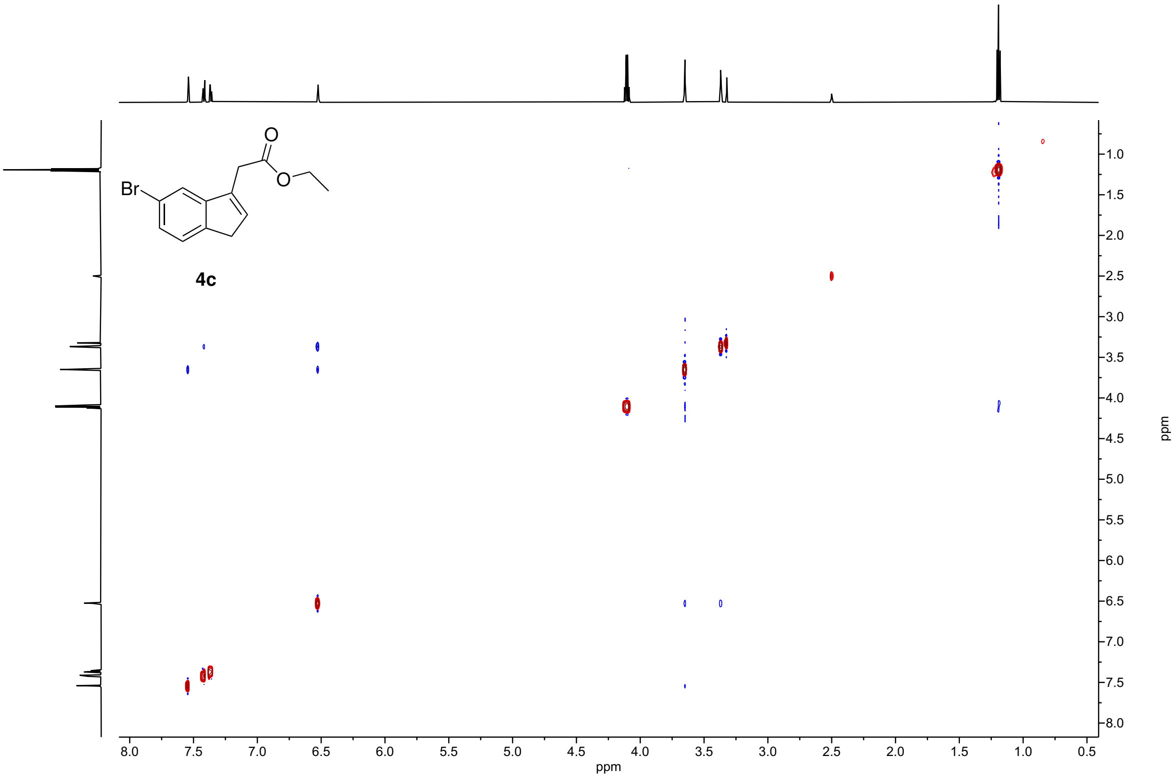

Figure E8: NOESY (600 MHz, DMSO–d$_6$) spectrum of **4c**.

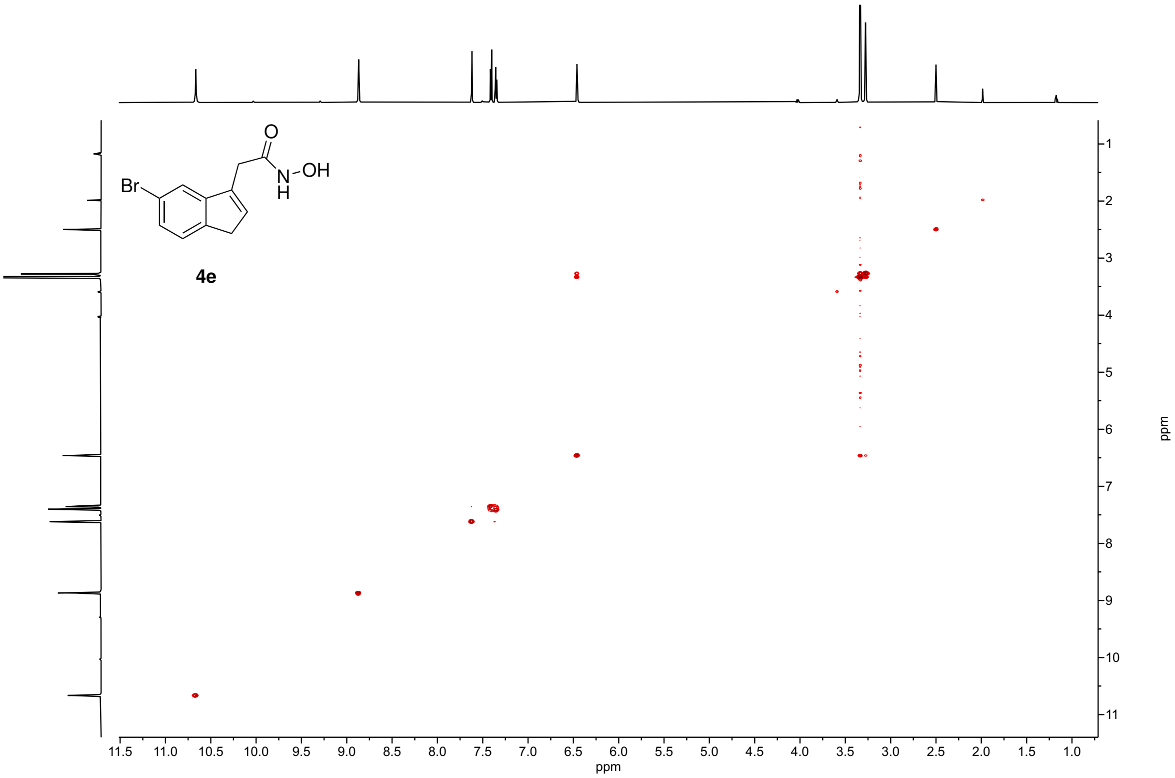

Figure E9: COSY (600 MHz, DMSO–d_6) spectrum of **4e**.

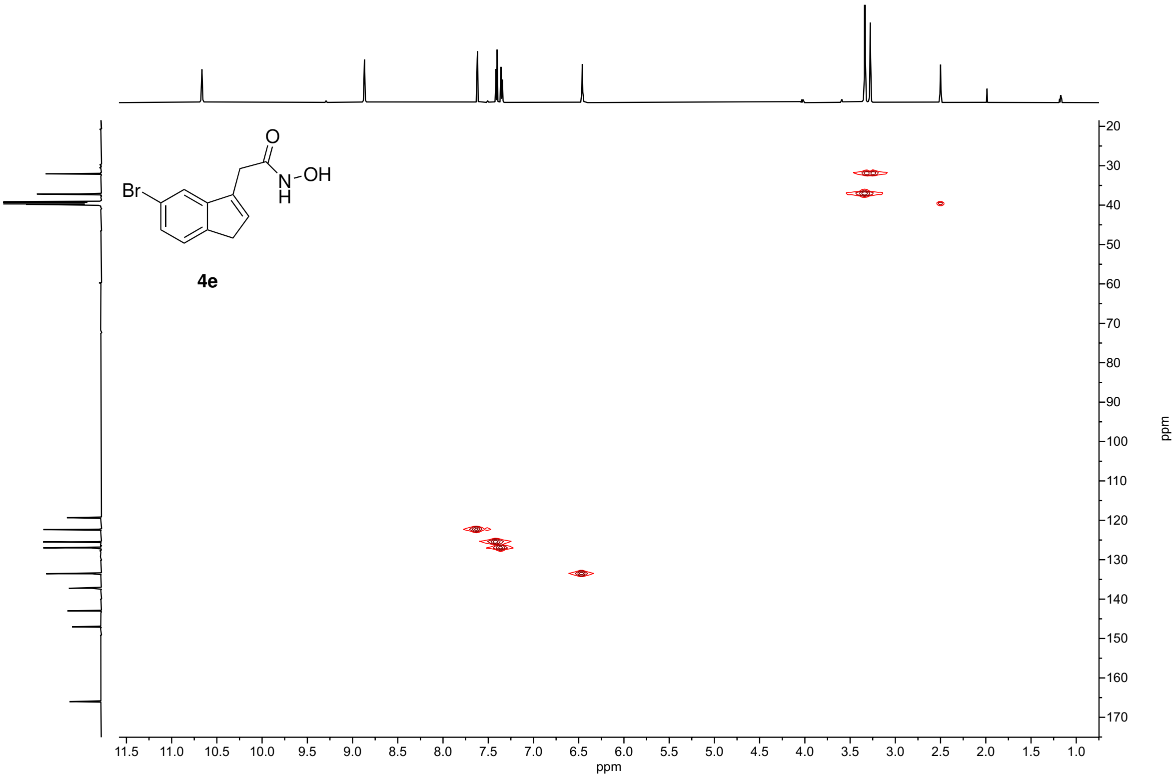

Figure E10: HSQC (600 MHz, DMSO–d_6) spectrum of **4e**.

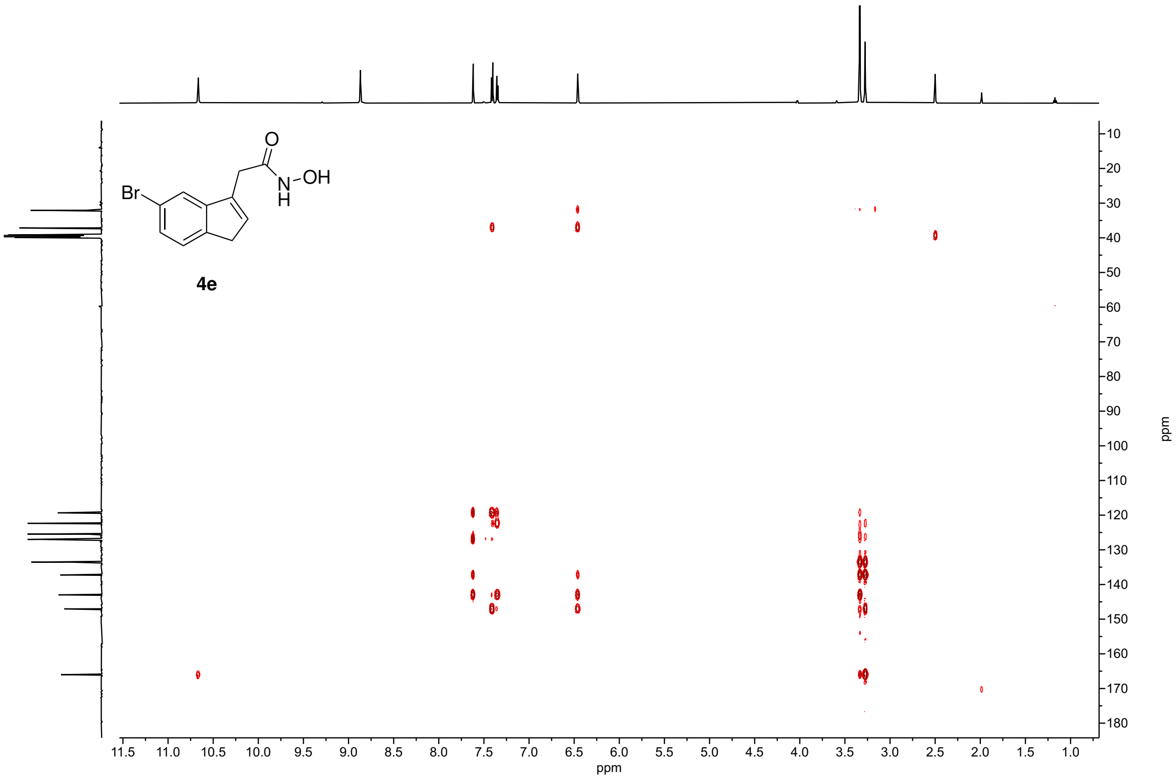

Figure E11: HMBC (600 MHz, DMSO–d_6) spectrum of **4e**.

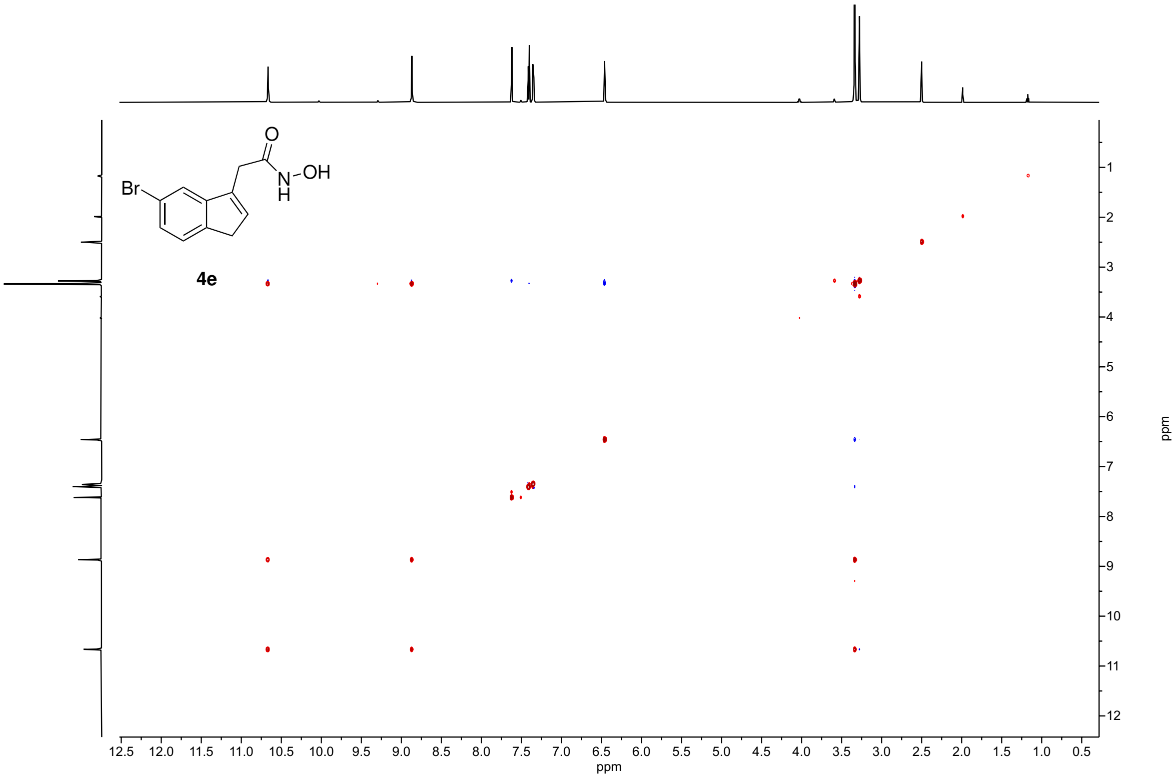

Figure E12: NOESY (600 MHz, DMSO–d_6) spectrum of **4e**.

F. NMR spectra of compounds from Route V

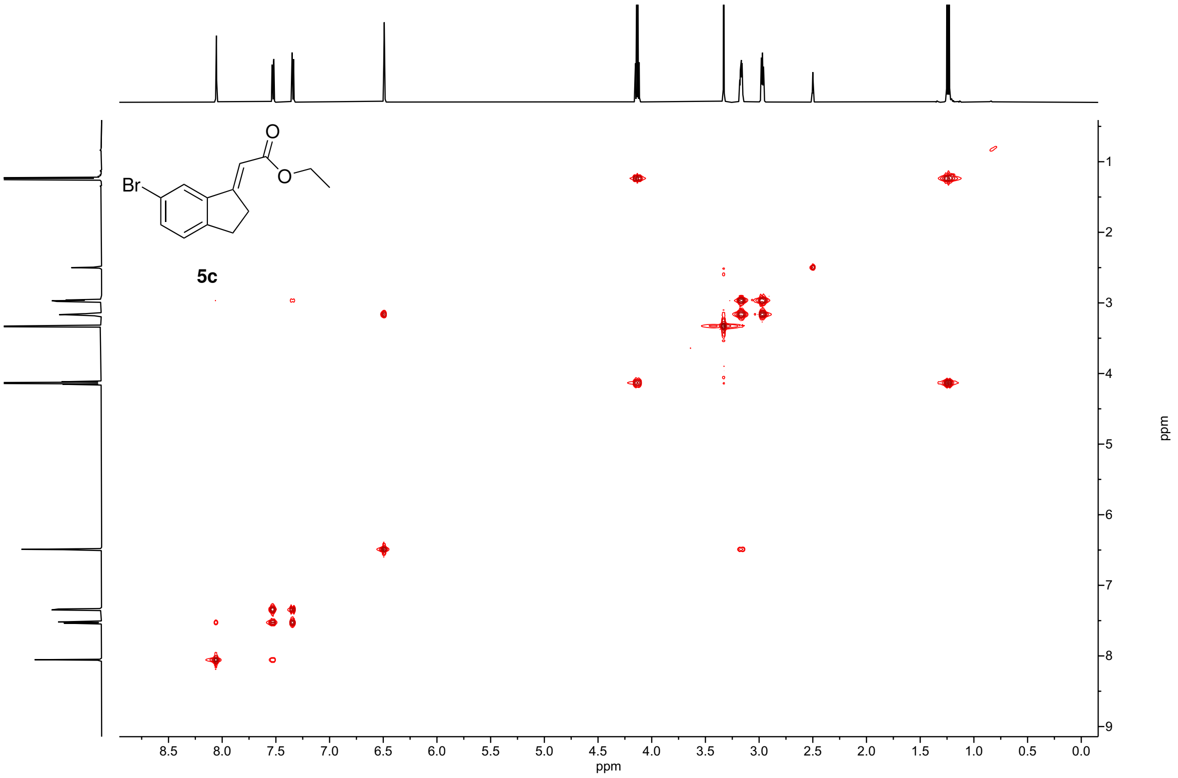

Figure F1: COSY (600 MHz, DMSO–d_6) spectrum of **5c**.

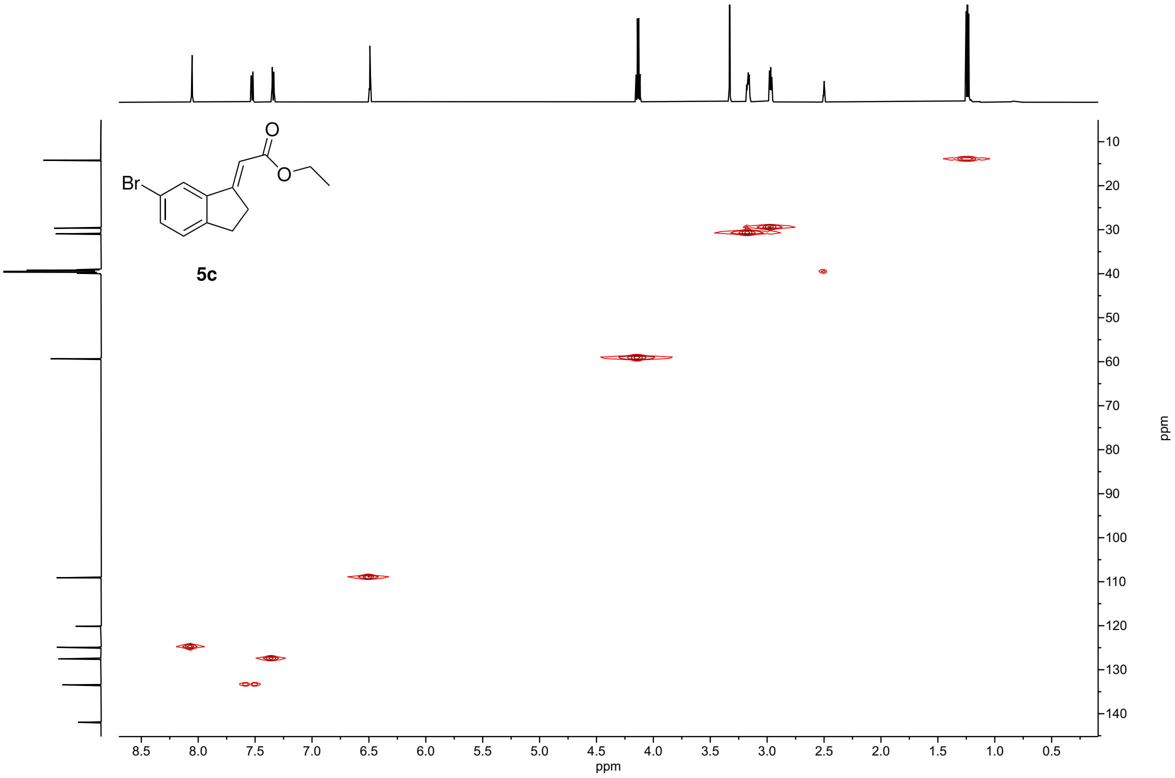

Figure F2: HSQC (600 MHz, DMSO–d_6) spectrum of **5c**.

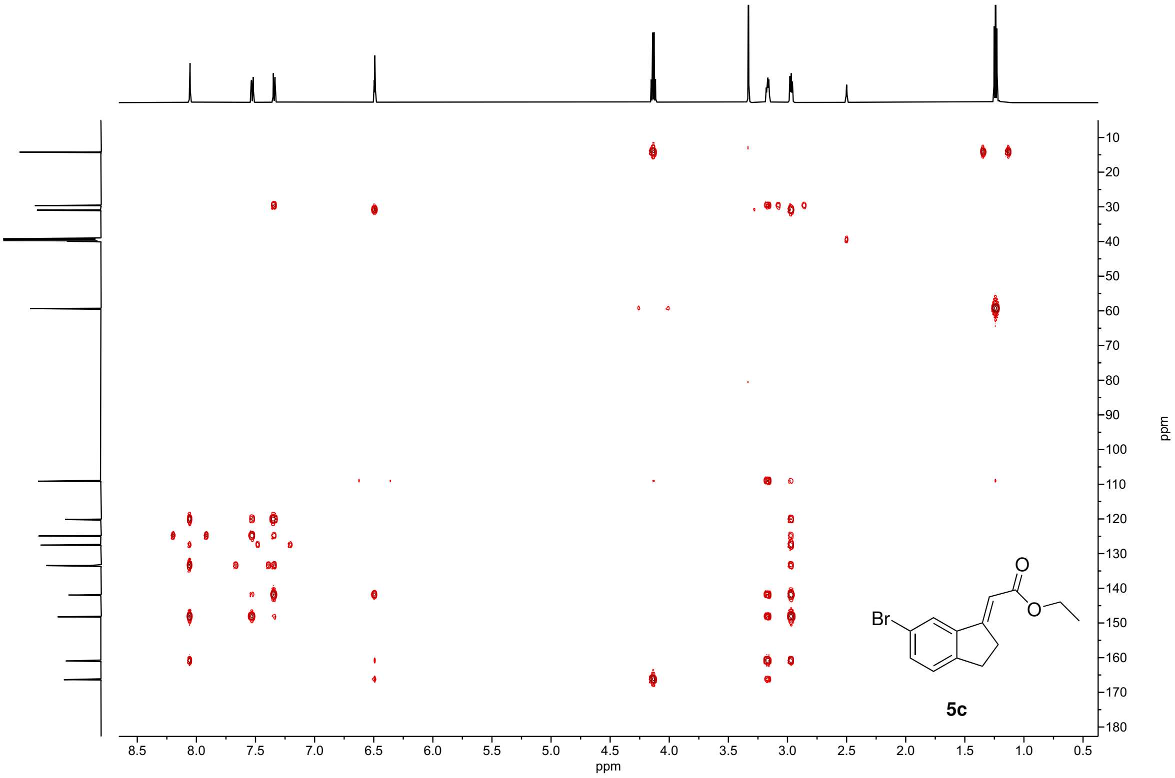

Figure F3: HMBC (600 MHz, DMSO–d_6) spectrum of **5c**.

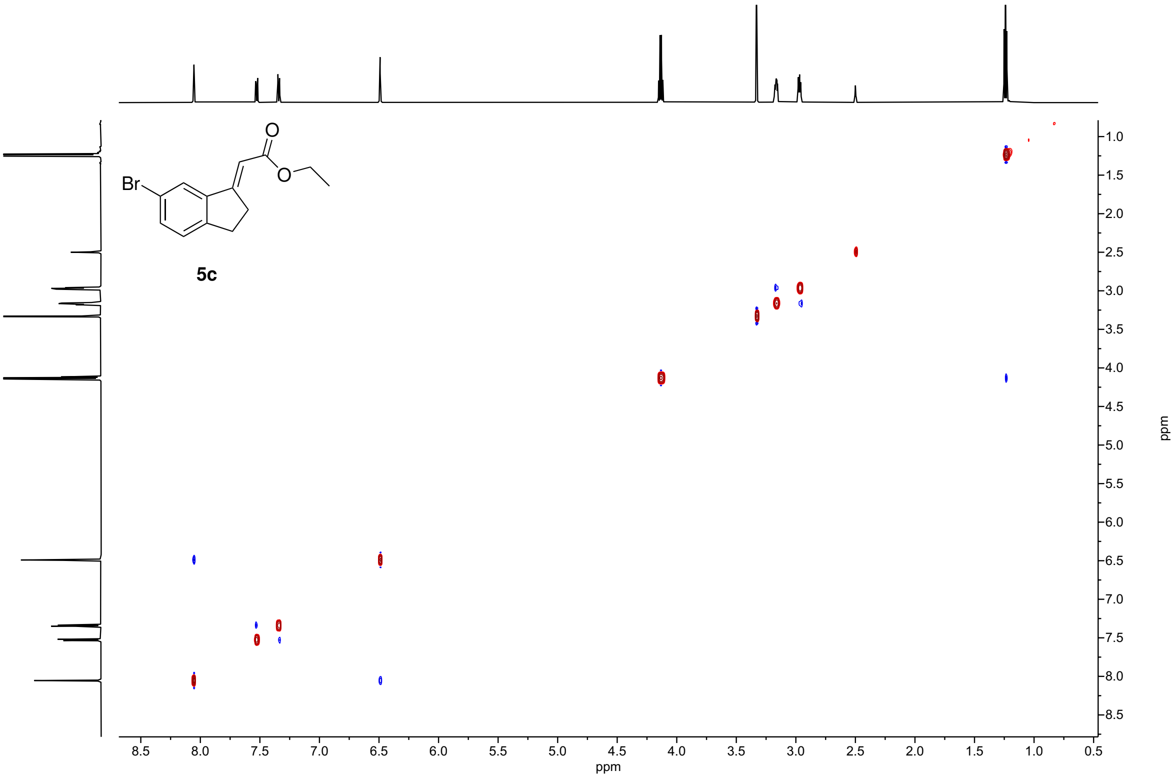

Figure F4: NOESY (600 MHz, DMSO–d$_6$) spectrum of **5c**.